Université Pierre et Marie Curie

École doctorale 397 Physique et Chimie des Matériaux

Institute de Nanoscience de Paris

Structure and Reactivity of Lutetium bis - Phthalocyanine Thin Films

Par Mattia FARRONATO

Thèse de doctorat de Physique

Dirigée par Nadine Witkowski

Présentée et soutenue publiquement le 16 octobre 2017

Devant un jury composé de :

Rudolf Petra, professeur, Rapportrice

Lozzi Luca, professeur, Rapporteur

Cabaret Delphine, professeur, membre du jury

Resel Roland, professeur, membre du jury

Humblot Vincent, chargé de recherche, membre du jury

Witkowski Nadine, professeur, Directrice de Thèse

"That's one giant leap for man, one small step for mankind"

M. Farronato

Acknowledgements

A thesis work is always a team work, even if the name of the PhD candidate is only one. At least for me this was the case. First and most important I have to thank my supervisor Nadine Witkowski, without whom this thesis would not even have started, who provided help and guidance and proofread the drafts of this thesis manuscript. Secondly I would like to thank Roland Resel for the help in interpreting the diffraction data, and guiding me while I was in Graz.
Most of the experiments required technical help. Apart from the two people I already mentioned I acknowledge the help from Hervé Cruguel who was late at night at the synchrotron and early in the morning at the STM. Sebastien Royer helped me in building, mounting, unmounting all the setups and tried to cheer me up even in the darkest day. Brigitte Kunert helped carrying out the XRD experiments in Graz.
I really want to thank all the PhD students at the INSP (Pierre Yves, Camille, Suzanne, Cyril, Romain, Alberto, Leo and everyone else I am forgetting now) for providing a live and stimulating environment. Among them a couple of names definitely stand out, a big thank you goes to Nathalie and Louis for making the office a pleasant place to live, and Danilo, who got here as an intern, and became both a colleague and a friend. I want to remember here the PhDs from the THINFACE project, it was nice and stimulating to meet you all a couple of times a year.
A special thanks goes of course to my mother Cristina and my father Franco, who never stopped believing in me. Also my girlfriend for his continued support and patience.
A few people I lived with are worth mentioning, Pierre, Joffrey and Giorgia, who always made my house feel like home.
A few friends back in Italy also indirectly contributed to this work, Marco (all 3 of you), Claudia, Claudio, Carlo, Niccolò.

Contents

List of Figures

List of Tables

List of Abbreviations

BE	**B**inding **E**nergy
DFT	**D**ensity **F**unctional **T**heory
FET	**F**ield **E**ffect **T**ransistor
GIXD	**G**razing **I**ncidence **X**-ray **D**iffraction
HOMO	**H**ighest **O**ccupied **M**olecular **O**rbital
HR-XPS	**H**igh **R**esolution XPS
IPS	**I**nverse **P**hotoemission **S**pectroscopy
LCD	**L**iquid **C**rystal **D**ynamics
LED	**L**ight **E**mission **D**iode
LEED	**L**ow **E**nergy **E**lectron **D**iffraction
LN	**L**iquid **N**itrogen
LUMO	**L**owest **U**noccupied **M**olecular **O**rbital
MPc	**M**etal-**p**hthalo**c**yanine
NEXAFS	**N**ear **E**dge **X**-ray **A**bsorption **F**ine **S**tructure
OFET	**O**rganic **F**ield **E**ffect **T**ransistor
OLED	**O**rganic **L**ight **E**mission **D**iode
OPV	**O**rganic **P**hoto**V**oltaic
OSC	**O**rganic **S**emi**C**onductor
Pc	**P**hthalo**c**yanine
PE	**P**hoton **E**nergy
PEY	**P**artial **E**lectron **Y**ield
RE	**R**are **E**arth
RT	**R**oom **T**emperature
SAM	**S**elf-**A**ssembled **M**onolayer
SDRS	**S**urface **D**ifferential **R**eflectance **S**pectroscopy
STM	**S**canning **T**unnelling **M**icroscopy
UV	**U**ltra-**V**iolet
UPS	**U**ltra-violet **P**hotoelectron **S**pectroscopy
Vis	**V**isible
XES	**X**-ray **E**mission **S**pectroscopy
XANES	**X**-ray **A**bsorption **N**ear **E**dge **S**tructure
XPS	**X**-ray **P**hotoelectron **S**pectroscopy
XRD	**X**-**R**ay **D**iffraction
XRR	**X**-**R**ay **R**eflectivity

Abstract

In this thesis work I studied the structure and reactivity of Lutetium bis-phthalocyanine ($LuPc_2$) thin films deposited on metallic surfaces. The knowledge of the structure of epitaxial organic thin films is extremely important to design the next generation of devices based on organic electronics, because crucial parameters as carrier mobility, and to an extent charge recombination, critically depend on the molecular configuration and thin film ordering. The second part of the work deals with the reactivity of molecular thin films towards atmospheric gases. This is particularly important when considering the lifetime of the device, as at the moment this is one of the greatest hindrance to the extensive use of organic electronic devices in everyday life. Phthalocyanine were chosen due to their already wide use in devices and their ease of process. In particular we chose LuPc2 because, due to the double decker molecular geometry they should present a different reactivity respect to single decker phthalocyanine, as the second macrocycle should hinder the reactivity on the metallic cation.

The work was carried out with a surface science approach, the thin films were prepared by thermal evaporation under ultra-high vacuum conditions and analysed by means of Scanning Tunnelling Microscopy (STM) and X-ray Diffraction (XRD) to achieve a complete characterization of the structure and the morphology. Than the chemical changes after reaction towards gases were studied by means of X-ray Photoemission Spectroscopy (XPS) and Near Edge X-ray Absorption Fine Structure Spectroscopy (NEXAFS) to study.

We resolved the structure of a $LuPc_2$ thin film deposited on Au(111), showing that the molecules adopt a β structure, the interaction with the substrate via the relaxation of the surface reconstruction, and demonstrated the templating effect of the substrate via the epitaxial relations with the overlayer. We then present the surface morphology at the molecular scale, showing the formation of large (tens of nm) islands composed by a double layer of molecules. From a careful analysis of the STM images we are able to show the stacking geometry, as well as the relative orientation of the different domains and compare this results with the one obtained by XRD.

We tested the reactivity of these thin films towards atmospheric gases, in particular oxygen and water, showing a low reactivity and managing to demonstrate the adsorption sites, which indeed are not the central cation, but rather on the macrocycle. We also showed how molecular oxygen is a greater threat to the molecular stability than water.

Resumé

Cette thèse présente dès les résultats de mes travaux sur la structure et la réactivité des bisphthalocyianine de lutétium en couche mince.
Dans le premier chapitre je présente un résumé de l'état de l'art sur les dispositifs basés sur des matériaux organiques et sur cette classe des molécules. Le chapitre commence avec une introduction sur l'électronique organique en général, l'intérêt qu'elle suscite actuellement, et les principales démarches historiques qui ont amené à cette situation. Après une rapide introduction aux principaux dispositifs basées sur des matériaux organiques, notamment les diodes organiques a émission de lumière (OLED), les cellules photovoltaïques organique (OPV) les transistors organiques à effet de champs (OFET) avec leurs structures et leurs modes de fonctionnement. Apres le concept de semi-conducteur organique (OSC) est introduit. Les OSC sont définies par Maitrot en 1987 comment des matériaux organiques (constitue par des unités moléculaires bien définies et agrégés a l'état solide), avec une conductivité intrinsèque entre 10^{-6}-10^{-1} $\Omega^{-1}\,\mathrm{cm}^{-1}$, et possible à doper avec et des donneurs et des accepteurs d'électrons. Le problème de la conduction dans des solides qui ne sont pas parfaitement ordonnés comment les semi-conducteurs inorganiques, mais présentent toujours un dégrée de délocalisation est discuté.
Evidemment plusieurs facteurs peuvent influencer l'efficacité des dispositifs. La structure des films est certainement un des plus importants : il a été démontré que le π stacking décale est plus efficace que le structures a chevrons. Un autre facteur très important est le degré d'ordre, soit ordre structurale et ordre en énergie, relatif aux variations locaux des interactions entre molécules. Un autre facteur très important est représenté de la possibilité de dégradation de la couche moléculaire. Cet évènement peut se produire à cause de la réactivité des molécules avec des gazes, ou aussi à cause de l'oxydation du substrat (les métaux utilise pour les contacts électriques par exemple). Une autre source de dégradation est la température : les composés organiques sont sensibles même à température modérément élevée ($\sim 100°$C), qui sont atteintes dans les cellules solaires organiques en fonctionnement. Le dernière facteur qui a été prise en compte est l'illumination : les composés organiques blanchissent sous rayonnement UV, surtout si couple avec la présence des gazes oxydants. Apres la physique des interfaces a été décrite, et trois types d'interfaces ont été présentes : interface entre couche organique et métal, entre couche organique e oxyde, et interface entre différentes couches organiques. L'interface Organique/métal est importante pour les contacts électriques du dispositif, et par conséquent l'allégement des niveaux énergétiques est particulièrement important. L'interface organique/oxyde

est étudiée à cause de la présence de ces isolants dans les OFET et les OPV. Aussi les oxydes conducteurs sont utilisés autant que contact dans certains dispositifs. L'interface organique/organique est concerné surtout dans les OPV, ou la couche active est souvent composée de deux différents matériaux interconnectes (hétérojonctions de volume, BHJ).
Ensuite la description des phthalocyanines (Pcs) est présentée. Ces macrocycle organiques ont été synthétisée la première fois en 1907, et depuis une large quantité de molécule appartenant a cette classe a été découverte, avec des différents groups au centre du macrocycle, ou avec des différents groupes fonctionnels, ou notamment des doubles. Les phthalocyanine sont des molécules organiques composes des quatre unités isoindoliques disposes en carre et rejointes par des azotés pontants. La cavité peut être remplie par deux atomes d'hydrogène (H_2Pc) ou par des cations métalliques (MPc). Ces molécules sont très résistent aux hautes températures et aux attaques chimiques à cause de leur système de 18 électron π conjugués, qui fournit une forte stabilisation. Des H_2Pcs ont été exposées vers NO, en montrant l'oxydation des deux N-H centraux. Si c'est une MPc à être exposée a des gazes oxydants (O_2, NO, NO_2...) c'est invariablement le cation métallique qui réagit, qui renvoyé a un problème de chimie des complexes métalliques.
Une classe similaire de molécules est composée de phthalocyanine doubles. Cela comprends des molécules ou le cation central (normalement une terre rare en configuration 3+) est trop gros pour être accommodé dans la cavité du macrocycle, et du coup est complexé par deux macrocycle, qui se trouvent en position étalée, mais pas symétrique : l'angle entre les axes moléculaires des deux plateaux est de 25°. Il est important de remarquer est que les deux macrocycle sont électriquement équivalents, cela signifie que tout le deux portent une charge 1.5-. La raison pour laquelle ces molécules sont intéressantes est qu'elles possèdent un orbital occupe a plus haute énergie (HOMO) et après un orbital mi rempli (SOMO) avant l'orbital vide a plus basse énergie (LUMO), ce qui le rend en principe facile à oxyder ou à réduire. Les propriétés électroniques sont, comme en général pour les phthalocyanines, dirigées par les électron π, qui donnent vie a 4 bandes d'absorption entre le proche UV et le proche infrarouge. La bande B a 3.2 eV (transitions des états profonds au LUMO et LUMO+1), la bande BV a 2.8 eV (du HOMO-1 au SOMO), la bande Q a 1.9 eV (du HOMO et SOMO au LUMO et LUMO+1) et la bande RV a 1.5 eV (du HOMO au SOMO).
Dans le deuxième chapitre les systèmes expérimentaux ont été décrits. L'ultravide est introduit, avec la raisons principale pour s'en servir (éviter la contamination des surfaces, qui arrive très rapidement à pression ambient), et les principales méthodes pour le produire et le surveiller. Successivement les vraies techniques expérimentales sont décrites, après une introduction au rayonnement de synchrotron, dès que la plupart des expériences présentées dans cette thèse ont été réalisé dans des synchrotrons, et aux différentes lignes de lumière utilisée pendants ces travaux. La première technique montre est la photoémission des rayons X (XPS), avec ses

principes de base, pour l'use qualitatif et quantitatif, et l'explication des certaines techniques de traitement des données utilisées pendant cette thèse. Puis la spectroscopie d'absorption de rayons X (NEXAFS) est introduite, toujours avec les principes de base, avec un regard particulier sur la possibilité d'étudier l'orientation des molécules. Apres les détails expérimentaux sont présentes, notamment les méthodes de récolte des donnes et leur calibration en énergie. Ces deux techniques de spectroscopie nous ont permis d'étudier les propriétés électroniques des molécules, une fois déposées sur le substrat et après avoir été exposées aux gazes pour en étudier la réactivité. Troisième est présentée la spectroscopie de réflectivité différentielle de surface (SDRS), qui nous a permis de vérifier en temps réel la préparation des nôtres couches. A la suite la microscopie par effet tunnel (STM) est présentée, qui nous a permis d'étudier la morphologie de surface de nôtres couches. La physique sur laquelle cette technique est basée est présentée en premier, suivie par certains détails expérimentaux, la préparation des pointes et la correction de la dérive. Dernière est présentée la diffraction des rayons x, (XRD), en particulier les techniques qui ont été utilisée pendant ce travail, le scan $\theta/2\theta$, les pole figures, utilisée pour étudier la mosaïque des échantillons et la diffraction en incidence rasante (GIXD), très utilisée dans les études des couches minces.

Dans le troisième chapitre les résultats sur la structure et la morphologie des couches minces (20 nm) de $LuPc_2$ déposée sur Au(111) sont présentés. Les études ont été menées par XRD et STM. En premier la structure des couches minces de $LuPc_2$ déposées sur du Si (100) reconstruit 2x1 terminé avec une couche passivant de Si-H est étudié. Le substrat est utilisé autant qu'exemple d'un substrat faiblement réactif. Les molécules s'organisent sur la surfaces avec une structure a chevron, appelée structure γ avec les plans moléculaires presque perpendiculaires a la surface du substrat. Celui-ci est la structure plus stable dans la poudre, ce qui est raisonnable en considérant la faible réactivité du substrat. Successivement les résultats sur les couches minces (20 nm) déposé sur Au(111) sont présentés. Les molécules s'auto organisent avec les plans moléculaires parallèles a la surface du substrat, probablement avec la structure α, qui par contre n'a pas été résolue pour des phthalocyanines doubles. Cette structure se transforme en la β avec un recuit a 280°C. La structure est stabilisée par un faible transfert de charge du substrat vers la couche moléculaire, qui a été montré par la relaxation de la reconstruction de surface (herringbone) du substrat. La couche présente au moins 2 domaines rotationaux, comment a été montré par des mesures de pole figures. Un étude plus approfondi de l'orientation des domains de la couche moléculaire relativement au substrat par GIXD avec radiation de synchrotron a été effectué. Les résultats montrent d'abord que, après un recuit la structure α se transforme en la β, qui a le même forme dans le plan, carré avec un vecteur de maille de 19.4$\mathrm{angstrom}$ avec les molécules à plat sur la surface, mais probablement un empilement diffèrent. Dans un des deux domains les vecteurs de la cellule unitaire sont presque parallèles a la direction $[1\bar{1}0]$ du substrat, le désalignement de un degree génère deux domains désalignés dans les deux sens par symétrie. Dans

l'autre domaine c'est la diagonal de la cellule unitaire qui est parallèle a la direction [$1\bar{1}0$]. Dans les deux cas l'effet prépondérant est l'alignement des axes moléculaires sur les directions plus condensées du substrat, pour maximiser les interactions de type van der Waal. L'effet de modelé des corrugation de la reconstruction à chevron du substrat est probablement moins important.
La morphologie de surface a été caractérise via STM. La couche est plutôt désordonnée après un dépôt à température ambiante, avec une surface à boulles. Après un recuit à 280degreeC pendant 10 minutes la surface reconstruit avec des larges terrasses avec beaucoup des molécules isolées dessus. Un recuit successif a 300°C amené a des iléaux en forme de doughnut (avec un trou au milieu). Ces iléaux ont par rapport à la terrasse sur laquelle croissent une hauteur qui est deux fois celui des molécules isolées. Elles sont donc formées d'une double couche des molécules, probablement à cause de l'élevée énergie associé à l'interaction molecule-molecule. De façon similaire le trou au milieu est „profond" comme deux couches de molécules. Les iléaux et la terrasse sous-jacent ont la même structure dans le plan. La structure est carrée avec un paramètre de maille de 19.4Å. Le packing dans le plan suit le principe des maximiser la distance entre les cycles benzéniques pour réduire la répulsion électrostatique, avec l'axe moléculaire tourné de 25° par rapport au vecteur de la cellule unitaire, qui a été confirmé par les calculs DFT. En particulier cet ordre-ci amené à deux géométries, dont une majoritaire. L'empilage moléculaire suit un principe diffèrent : les molécules s'empilent l'une sur l'autre avec les axes moléculaires parallèles. Ces deux conditions amènent a une superposition des anneaux benzéniques, qui est explicables en regardant la simulation des orbitaux moléculaires, qui montrent que la densité de charge de l'HOMO est surtout localisée sur la moitié du cycle benzénique, ce qui permet l'empilage en minimisant la répulsion électrostatiques. L'empilement avec les benzènes en position échelonnée est aussi présent, et ni l'une ni l'autre géométrie ne sont majoritaire. L'investigation des différents orbitaux moléculaires (HOMO et LUMO) est poursuivie avec des topographies a différentes tensions (entre +2 V et -2 V), et comparée avec les résultats obtenu par DFT.
Dans le quatrième chapitre la réactivité des couches minces de $LuPc_2$ est présentée. D'abord les propriétés électroniques de la molécule isolée ont été étudiées. La de convolution des pics de photoémission du C 1s et du N 1s est présentée avec une discussion sur la position des pics de shake-up. En particulier dans le cas du pic du C la transition de shake-up plus probable est celui entre HOMO→LUMO, dans le cas du N 1s est plutôt une transition SOMO→LUMO. La spectroscopie NEXAFS montre que les molécules sont à plat sur la surface d'or, qui est en accord avec les résultats de diffraction et STM, et les différents pics sont assignés à l'aide des calculs DFT présents en littérature. La réactivité vers l'oxygène a été étudiée en condition de „haute" pression (autour de 1 mbar) avec la spectroscopie NAP-XPS (Near Ambient Pressure-XPS). Le pic d'oxygène est présent dans les spectres recueillis pendant

l'exposition au gaz, mais disparait après la ré-évacuation de la chambre. Ce fait signifie que l'oxygène ne colle pas sur la couche moléculaire. En plus les pics du C 1s, N 1s et Lu 4f ne présentent aucun changement. Baisser la température autour de 80 K permet d'augmenter le coefficient de collage des molécules d'oxygène sur la couche moléculaire. L'oxygène est effectivement physisorbé sur la surface à 88 K. A l'XPS on voit aussi apparaitre une bosse at haute énergie de liaison (Binding Energy, BE) dans le spectre du N 1s et C 1s (plus évidente sur le spectre du N 1s), qui augmente avec la dose d'oxygène. Le processus est complétement réversible des que le système est réchauffé a température ambient, i.e. l'oxygène est complétement désorbé et les spectres de la couche après la désorption sont superposable a ceux avant l'exposition. La faible température de désorption, couplée avec l'analyse des BE des composantes additionnelles dans les spectres de XPS nous permet de exclure la formation d'une liaison chimique entre l'oxygène et la molécule de $LuPc_2$. Avec le support des simulations DFT on peut formuler l'hypothèse que la molécule d'oxygène soit adsorbée sur un des carbones pyrroliques (atomes de carbone liés à l'azote pyrrolique). La spectroscopie NEXAFS permet de vérifier l'effet de l'adsorption sur les orbitaux vides de la molécule, et après l'exposition à l'oxygène montre une transition supplémentaire due à la transition $N_{Ox} \rightarrow$ LUMO due aux atomes d'azote avec un contexte chimique différente à cause de l'absorption d'oxygène. En plus il y a une inversion des intensités des deux transitions π*, due à l'épuisement de charge dans le LUMO. Le NEXAFS sur l'oxygène montre que une multicouche a été adsorbée et confirme aussi que l'interaction avec la couche moléculaire est faible. Aucun changement n'est vu pour le lutétium.

La réactivité vers l'eau a été testée aussi. A haute pression (et température ambient) les résultats sont similaires à ceux avec l'oxygène, ce qui signifie pas de pic d'oxygène résiduel après l'évacuation de la chambre. La seule différence est la présence d'un shift rigide des pics de photoémission de 0.2 eV pendant l'exposition à l'eau du probablement a un changement du potentiel de surface ; la position initiale est récupérée après l'évacuation de la chambre. A basse température l'eau condense (gèle) sur la couche moléculaire, et est désorbé a -107°C. L'absorption ne porte à aucune variation sur les spectres XPS et NEXAFS du C et N, mais l'analyse du spectre NEXAFS de l'eau permet de trouver un faible transfert de charge de la couche moléculaire aux molécules d'eau.

L'exposition à l'air a été également testée. Une couche de contamination est présente sur la surface de l'échantillon, probablement composée des molécules organiques à base de C et O (CO ; CO_2...), qui est enlevée après un recuit a 280°C pour 15 minutes. Le recuit permet d'obtenir une surface qui est possible imager avec un STM.

Pour tester l'effet de la structure de la couche sur la réactivité et en particulier sur la pénétration des gazes un échantillon de $LuPc_2$ déposée sur du Si(100) a été exposé a l'air. Sur le Si(100) propre les molécules ont une structure plutôt amorphe, avec des domains de structure γ. La couche moléculaire ne fournit aucune protection au substrat, qui s'oxyde à l'atmosphère. Un appendis est présenté pour comparer les

résultats obtenu sur les effets de la radiation X sur nos échantillons avec des résultats de littérature.

Chapter 1

State of the art

1.1 Organic electronics

1.1.1 Introduction to organic electronics

Organic electronics is attracting a lot of interest lately. Figure 1.1 shows the number of papers found on the Web of Knowledge with search word "organic electronics", "organic LED" "organic photovoltaic" and "organic field effect transistors" in the last 20 years. A steady increase is seen for all the three categories, showing the interest of the scientific community for this new promising technology. All this attention started with the synthesis in 1977 of electrically conducting organic polymers through controlled halogen doping by A. G. MacDiarmid, A. J. Heeger and H. Shirakawa [127]. This work was later acknowledged as a major breakthrough and the three were awarded the Nobel prize in chemistry in 2000. This opened the gates to a whole new world for electronics. Organic materials have a lot of unique properties with respect to their inorganic counterpart. The carbon chemistry is extremely rich, allowing for countless variations and fine tailoring of the final material: the first conducting materials were insoluble, and intractable, but functionalization led to soluble, easy to use materials with the desired properties. All the processes can happen in solution [96], allowing the final device to be actually printed roll to roll, firstly shown in 2005 by Makela and coworkers [94], then improved by Krebs [78], who was able to avoid the use of Indium Tin Oxide as an electrode and now widely used in industrial production (see for example the paper from Krebs [79] and the review by Søndergaard [130]). Also another important advantage of organic devices is the need for only a mild annealing (usually below 200°C), which is very low (and therefore very easy and very cheap) if confronted with the 1425°C needed for the Czochralski process for Silicon. Another important aspect in a world that is becoming more and more aware about resources usage is the possibility of producing fully recyclable devices, as was shown since 2010 by Matyba and coworkers [96] who produced an OLED (Organic Light Emission Diode) made entirely in plastics, exploiting graphene as a transparent conducting electrode.
Following the discussion of the three most important class of devices which will benefit from a switching to an organic-based technology.

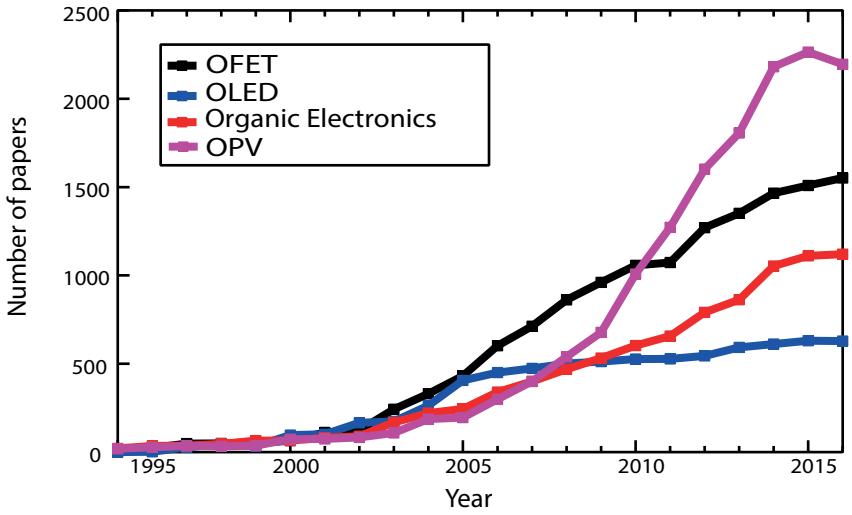

FIGURE 1.1: Number of papers published each year with the keywords "organic electronics", "OLED" 'OPV' and "OFET."

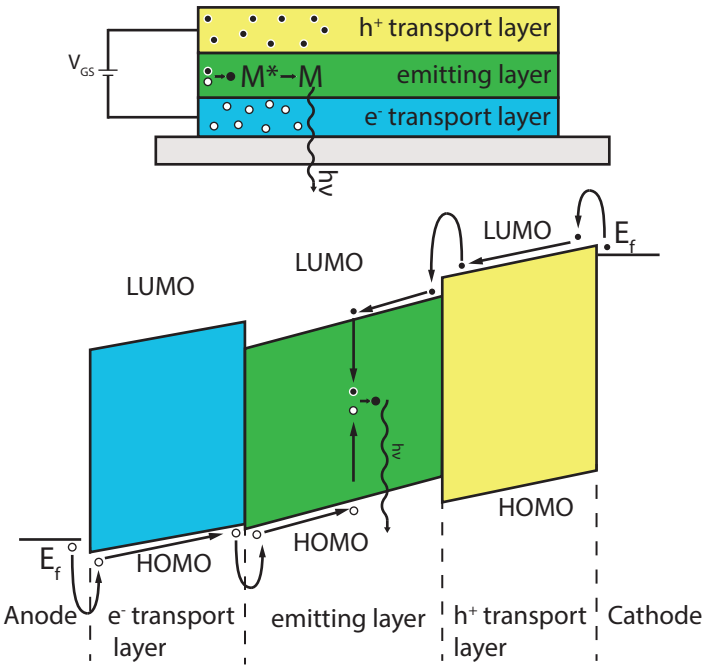

FIGURE 1.2: Pictorial depiction of an OLED device (top) and its energy level scheme (bottom).

Organic Light Emission Diode Right now OLED is the most industrially exploited organic-based technology. The organic display TV and smartphone market is worth almost 35 billion dollars in 2016 (source: IDTechEx). The working principle is quite simple, and divisible in 5 steps (see Figure 1.2):

1. Voltage is applied between two electrodes holes (electron) are injected in the organic layer from the anode (cathode)

2. the charge than migrate under the influence of the applied electric field

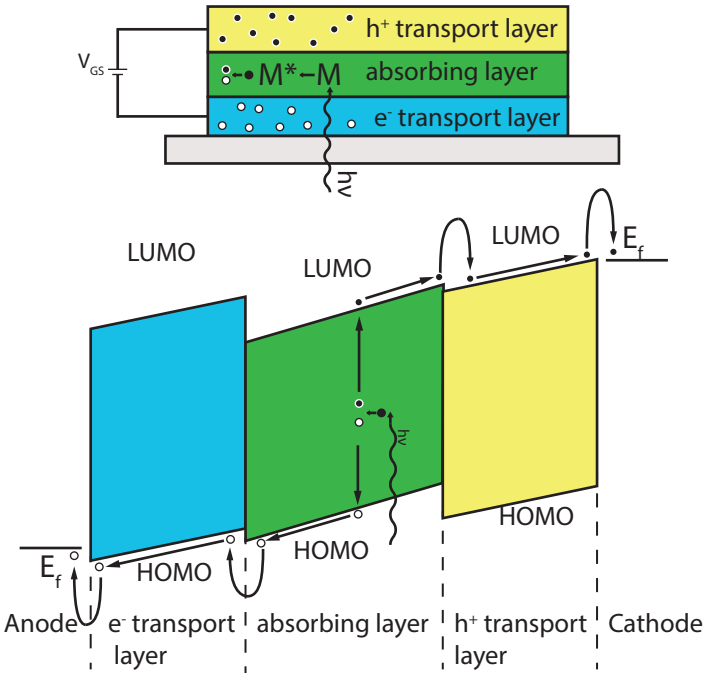

FIGURE 1.3: Pictorial depiction of an OPV device (top) and its energy level scheme (bottom).

3. a moving hole and an electron have to capture one another to form an exciton (excited state) on a molecule (or on a polymer segment);

4. the exciton has to decay radiatively with the emission of a photon;

5. the photon has to escape from the device.

For the Organic Photo Voltaics (OPV) the process runs in the opposite direction. In most cases architecture optimization are usually put in place, most notably the addition of a Hole Transport Layer and an Electron Transport Layer, to better match the energy levels of the contacts and the active layer. This implies a large number of interfaces, which all play a fundamental role in the functioning of the device, most notably in the energy level alignment. OLED with respect to LCD displays offer a lower power consumption, a darker black (amount of light emitted when the pixel is switched off) and high contrast.

Organic PhotoVoltaics Due to low efficiency (13.2% being the world record (source: Heliatek)) their use is not yet wide. But the low cost and the increasing lifetime is making them interesting for wide area, for example on windows (where only semi-transparent organic solar cells can be installed). The working principle is the exact opposite of the OLEDs (see Figure 1.3): a photon is absorbed by the active layer, and an exciton is formed. The exciton is then split and hole and electron migrate to the opposite electrodes where they are collected. Usually the charge transport happens in two different materials, an electron donor and an electron acceptor. The interface between the two is crucial in both the smoothness (a large contact area between the

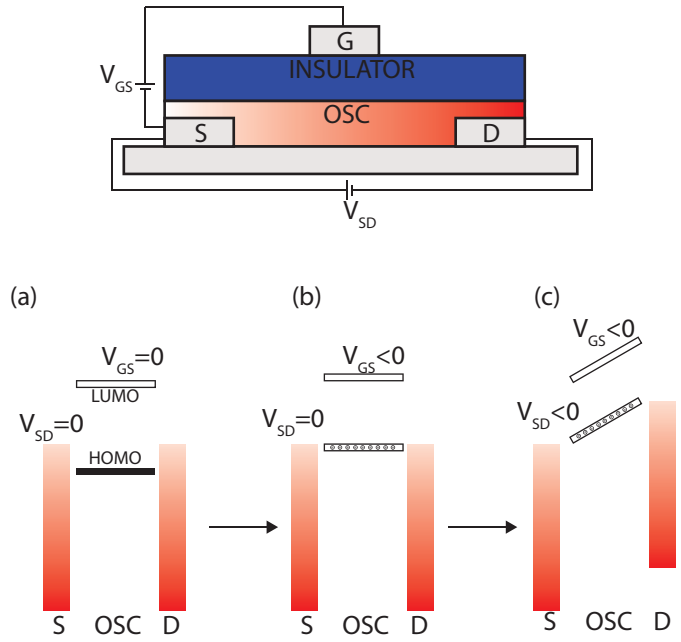

FIGURE 1.4: Pictorial depiction of an OFET device (top) and its energy level scheme (bottom).

two moieties will allow a more efficient charge transfer process) and in the alignment of the energy levels. The interfaces with the electric contacts play a very important role as well in the same way as in the OLED.

Organic Field Effect Transistor Organic Field Effect Transistors (OFET) are the most interesting organic-related technology. The possibility of producing microelectronic devices by roll to roll printing is extremely attractive for low-cost application as radio-operate labels where they can be used for example to replace barcodes so a customer would not have to pass all the items in front of the reader, but just transit with the full cart in front of the reader. Other applications are information storage, or as an actuator in active matrix OLED screen to allow the control of single pixels. Another interesting application is as gas sensors. In this field the interest is due to their inverted architecture, which brings the semiconductor in direct contact with the analyte. A field effect transistor (FET) consists of four different parts (see Figure 1.4 top) three metallic contacts for the Source, Drain, and Gate contacts, a semiconducting layer connecting the source to the drain, and an insulating layer to separate the gate from the semiconducting layer. In an O-FET at least the semiconducting layer has to be made with an organic material. The working principles of an OFET are schematized in Fig.1.4. In particular the schema refers to a p-type channel based on charge accumulation: when a voltage is applied between the Gate and the source the energy level of the organic align and the charges (in this case holes) can hop be injected in the organic semiconductor where they start accumulating. When a voltage is applied between the source and the drain then a current can pass in the OSC. This working principle is very inefficient due to great off-currents (leakage). It

TABLE 1.1: Brief summary of the biggest advantages and disadvantages of the organic-based electronic technologies.

PROs	CONs
Cheap materials	Low electrical conductivity due to low carrier mobility
Cheap processing	Processing incompatible with existing technology
Recyclable	Low lifetime
Fast production	High leakage current (bad transistors)
Taylorable	
Flexible (adapts to different surfaces, does not break)	
Compatible with existing technology (silicon)	

was not until 2013 that an OFET was demonstrated to work in the charge inversion mode [91]. They were able to show an efficient depletion and inversion transistor. Depletion was achieved simply by keeping the OSC layer as thin as possible while inversion devices were created by doping both the drain and the source contacts to increase the efficiency in the charge carriers injection.

Comparison with inorganic technologies Table 1.1 shows a brief summary on the comparison between organic and inorganic based technologies. It is apparent that for a new technology the advantages are large, in particular the cheaper processes and materials are appealing, while the flexibility (and the semi transparency) allows for the use in niches that are impossible to fill with silicon-based devices.

1.2 Organic Semiconductor

The possibility of designing all the above-mentioned devices resides on the availability of organic materials with semiconducting properties. An intrinsic (inorganic) semiconductor is defined as a semiconductor with a finite concentration of charge carriers in absence of doping. The creation of free carriers (i.e. the excitation of electrons in delocalized states) is achieved by thermal or electrical excitation, opposed to doped semiconductors where it is achieved by adding electrons or electronic states to the pure material by doping. Organic semiconductors (OSC) were defined in analogy with a paper by Maitrot in 1987 with the following criteria [93]:

- It should be a molecular material, i.e. built from well-defined molecular units which can be synthesized separately and then assembled in some organized condensed phase (single crystal, thin film...).
- The intrinsic conductivity of the material should be around 10^{-6}-$10^{-1}\ \Omega^{-1}\,\mathrm{cm}^{-1}$.
- The material can be doped with electron donors or acceptors.

TABLE 1.2: Charge carriers mobility for different organic semiconductors: $LuPc_2$, CuPc and polytiophene, compared to amorphous Si (a-Si:H), single crystal (SC) Si and perovskites. Values taken from ref.[92] [81] and references therein.

Material	$\mu\ (\mathrm{cm}^2\,\mathrm{V}^{-1}\,\mathrm{s}^{-1})$
a-Si:H	0.1 - 2
SC-Si	300 - 1200
InAs	80000
perovskite	<2000
polytiophene	2×10^{-5}
βCuPc	9.7×10^{-5}
$LuPc_2$	10^{-4}

The mobility of the three different organic semiconductors (two molecular and one polymeric) are compared to single crystal (SC) Silicon and to amorphous silicon (a-Si:H) in Table 1.2, showing way lower values for organic semiconductors. Note that mobility (μ) is related to conductivity (σ) by the equation $\sigma = ne\mu$ where n is the charge carriers density and e is the elemental charge. In inorganic semiconductor electronic transport happens along delocalized states (bands), in organic materials, however, the situation is more complex. Two models have been proposed: band conduction and hopping process, but except from these very strict conditions other processes are involved. In this case the principal difference between the two models is probably the community that introduced them. Organic electronics is a contact point between chemists, who adopt the molecular point of view, and therefore consider individual units, and physicists, who adopt the crystal point of view, and think in terms of band structure. Indeed a contact point has to be found between the two extreme pictures. Indeed a contact point has to be found. We can start examining the models. At one side of the spectrum the Variable Range Hopping (VHR) model is found, where electronic states are confined on a single molecule, and for the conduction to happen the charge has to "hop" from one molecule to the adjacent one (see Figure 1.5 a)) For this to happen a donor molecule and an acceptor one are needed in the allowed spatial and energy range. The model was first introduced by Mott [99] for impurity conduction in inorganic semiconductors and can be described by the equation

$$P(r, W) = exp\left(-ar - \frac{W}{k_B T}\right) \tag{1.1}$$

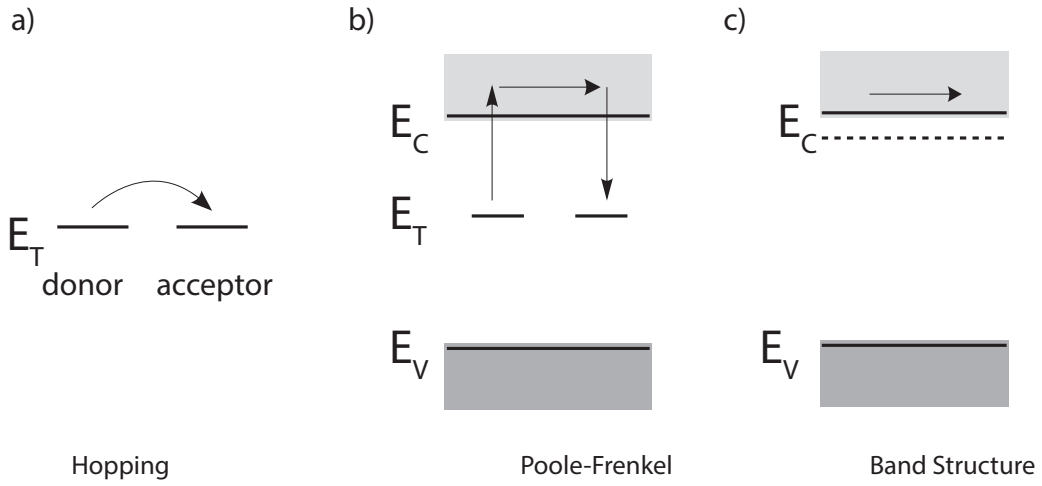

FIGURE 1.5: The different conduction models: a)hopping; b)Poole-Frenkel trap and release; c)bands. Image adapted from ref. [131], E_V is the valence band energy, E_T is the energy of the trap states, E_C is the conduction band energy.

where P is the hopping probability, a is a constant, r is the spatial distance between hopping sites, W is the energy separation between the two sites, and k_BT is Boltzmann's factor. The model is effective in explaining the temperature dependence of the mobility, which was experimentally found to be a power law. It is clear from Equation 1.1 that it exists a radius where two adjacent spheres begin to touch each other. When this condition applies we enter in the field of the Percolation Theory, where the current is allowed to percolate through a network of conductive material embedded in a non-conducting environment. At the opposite end of the spectra there is band theory (see Figure 1.5 c)), where charges do not belong to a single molecule anymore, but to the whole crystal. Band structure derives from the translational symmetry of the inorganic crystals, and in fact in ultrapure organic single crystals "bands", i.e. states delocalized over a few molecules, are indeed found [102]. This model allows to explain the field dependent mobility observed in organic semiconductors which is of the form of $\mu \propto \sqrt{\frac{\mathbf{E}q}{\pi\epsilon}}$ with ϵ the dielectric constant of the medium, q the elementary charge ad **E** the applied field. The dichotomy between the two cannot be as sharp as depicted: sure molecular overlap is important, but it cannot be accountable for the loss of 6 order of magnitude passing from single crystal to amorphous pentacene. The answer to this problem are trap states [131]. The trap states arise from the imperfect stacking in non-crystalline materials or under coordination which leads to unpaired electrons. These kinds of states are very abundant, up to some percent. Regarding the number of trap state we can range from

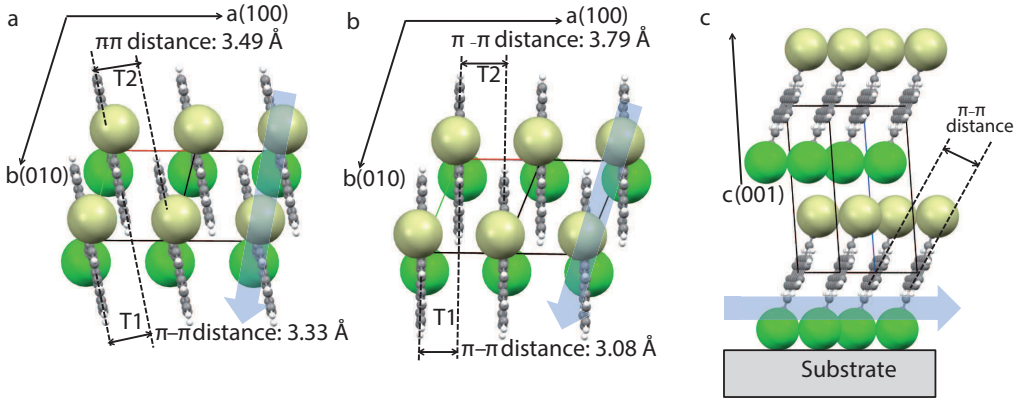

FIGURE 1.6: Molecular packing structure of TIPS-pentacene thin films prepared under different conditions: a) thermal evaporation; b)deposited by spin coating; c) same as b) but along the cofacial axis. Image taken from ref. [56].

the situation where only trap states exist (Multi-Trap Release or MTR model). This hybrid model has the advantage of explaining both the temperature and the field dependence of the mobility and also of unifying two different theories used for the same phenomenon.

1.3 Factors Influencing the Efficiency of the Devices

As we have seen before the charge mobility is a crucial factor in determining efficiency of devices based on organic semiconductors. There are, however, a few different factors that influences charge mobility, which are discussed below.

1.3.1 Film Structure

Charge carrier mobility is known to vary along different crystallographic directions in inorganic materials. In organic materials, where the anisotropy is even larger the same rule applies and two structural factors can influence the mobility: molecular stacking and order. The first is closely related to the structure of the material. Because the transport happens either by hopping or band-like it needs an overlap between adjacent molecule orbitals. The most common structure adopted in organic conjugated material is a herringbone-like structure, which is a highly anisotropic one, with a dense in-layer stacking and a poor overlap between the layers. It was shown that the interlayer mobility was lower respect to the in-layer mobility by a factor 3 or 4 [134]. This shows that the herringbone structure might not be the ideal structure for electric conduction. Other geometries, for example the π stacked ones might be more interesting, as the conduction might as well happen between the layers. In fact this is rarely true. The actual π stacking in fact is not with the molecules one on top of the other since a cofacial packing would be unfavourable due to the pi electron cloud repulsion, but is usually displaced along one or two of the molecule axis [16], which reduces the π-π repulsion, but might reduce the orbital overlap as

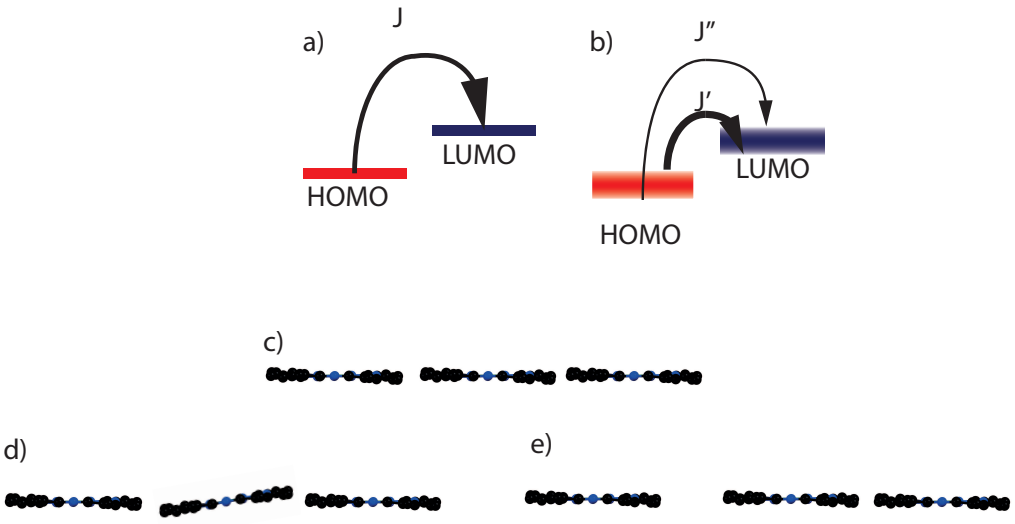

FIGURE 1.7: top:Energy level scheme for a perfectly ordered ideal system (a) showing a localized state and a real disordered system (b) showing a larger, less localized state; J is the overlap integral, the size of the arrow is proportional to the integral value. Bottom: perfectly ordered ideal system c), examples of possible off diagonal disorder: rotation d) or displacement e) of a molecule in the lattice.

well. In fact it was shown reducing the π-π distance by means of lattice strain as shown in Figure 1.6 a) and b) resulted in a 6-fold augmentation of the mobility in a TIPS-pentacene layer [56]. So to engineer the ideal structure a precise knowledge of the topography of the frontier orbitals is necessary.

1.3.2 Order

Not only structure but also order (or, talking about organic thin films, disorder) is a key factor when discussing the electronic properties of OSC. However different kind of disorder can influence charge transport in OSC. Coropceanu [30] divided it in Diagonal and Off-Diagonal disorder. Diagonal disorder refers to the fluctuations in site energy which is usually caused by polarization effect from surrounding molecules, and is exemplified in Figure 1.7a,b). It is possible to see the spreading of the energy level, and the hopping path (exemplified by the overlap integral J), which becomes either favourable (J') either unfavourable (J") by the disorder (remember that a single dead end is sufficient to stop a conduction pathway). Off-Diagonal Disorder instead refers to the different interaction between adjacent molecules, and is exemplified in Figure 1.7c,d,e). It is easy to see how these two effects that will reduce hopping probability are a function of the film order. A perfect example of which is shown in ref. [147] who showed a drastic drop in carriers mobility when transitioning from a single crystal phase to a mesophase in a liquid crystal thin film. Another interesting result [71] is the reduction in Diagonal disorder after suppression of thermal motion by careful tailoring of the molecule (substituting side chains along the long

axis of the molecule), which is believed to be the most important limiting factor for the efficiency of organic semiconductors [25].

1.3.3 Degradation

Probably the most troublesome aspect of the application of organic materials to electronic application is their low stability. There are different processes that can reduce the efficiency of an organic electronic device; they are presented below:

Reactivity Organic devices are usually encapsulated to avoid contact with air or other pollutant, but as no encapsulation can be perfect, so the effect of gas exposure on the devices has to be taken into account. The presence of gases can lead to different degradation processes [124]. The most intuitive mechanism is the reaction of the organic with the gas. It has been shown [143] that PCBM can react with oxygen leading to different products, and the same occurs for C_{60} [85]. Also C_{60} is found to polymerize in presence of oxygen at 80 °C, which is an operating temperature for an OPV cell. Even if the reactivity of organic semiconductors towards air might be low at operating temperature, the simple diffusion of gas molecules can lead to the formation of shallow traps blocking the electric conduction. It is the case of water in PCBM [143] which interestingly was less reactive than molecular oxygen.
Another crucial point is the interface layer, in particular when low work function metals (as Alluminum) are used as a contact due to ease to oxidize [59]. This can lead to delamination, with the appearance of dark spots on the device [140].

Temperature One of the biggest advantages of organic materials applied to electronic devices is, as shown earlier, the possibility to employ low temperature processes. The high sensitivity of organic materials even to temperature around 100°C becomes also a great problem, due to degradation processes activated by heating under working conditions. Most of the problems are due to the elevated thermal expansion coefficients and the low melting point of most of the OSC. This might lead to delamination, phase transition [54] and agglomeration in case of bulk heterojunction devices [38]. A nice review about heat generation and the damage it provokes in OLEDs was proposed by Tyagi and coworkers [140] who pointed out that electrical resistance at the interfaces is one of the main source of heat generation.

Illumination OSC are known to bleach when exposed to UV light. The most important process is photoactivation of oxidative processes [128] by the formation of oxygen radical species [158]. Another possibility is the cleavage of specific molecular bonds when the molecule is in the excited state (or even more in charged states), as was demonstrated by Lin and coworkers [87] for $CzPO_2$ (a molecule used in

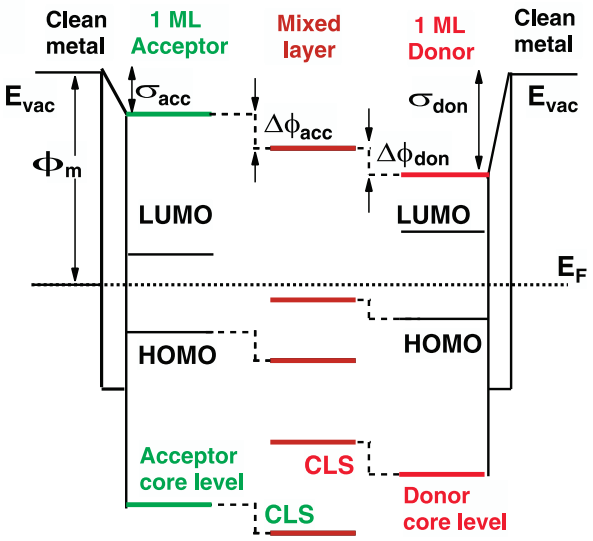

FIGURE 1.8: Schematic of the energy level alignment of the interface between a metal contact and an OSC donor/acceptor mixture. The dotted lines show the shift of the molecular levels upon vacuum level pinning. Taken from ref. [44].

OLEDs). Moreover photobleaching is well known on many different classes of organic molecules as phthalocyanine [47]. Also it can lead to crystallization of one of the two phases of a bulk heterojunction, as was shown for boron subphthalocyanine chloride [145]. Another mechanism is represented by the formation of radicals.

1.3.4 Interfaces

Another key aspect is the interface between the organic semiconductor and the other components of the devices [31, 3]. These are usually either metals (contacts), either insulators (the gate in OFET), either other organic materials (blends are mostly used in OPV for the light absorbing and the transport layer). Two kinds of phenomena have to be taken into account when studying interface: electronic interaction between substrate and overlayer and the morphology, i.e. the presence of surface stabilized polymorph.

Organic/Metal Interface The most commonly used metal in microelectronics is gold, due to its low reactivity, and in fact most of the organic semiconductors adsorb on it without any major modification of the structure or of the electronic properties. Instead on copper the interaction is stronger, leading to chemisorption [90] which implies a strong electronic coupling and can result in a deformation of the organic molecule [119]. It was shown [44] in the case of a weak interaction (molecules-gold for example) that the electronic coupling can lead to a rigid shift of frontier (HOMO, LUMO) orbitals and core level in both electron acceptor and donor. These phenomena are ascribed to a local keep of the vacuum level, and allow to study the interaction, which is crucial for charge injection at the electrodes, by mean of core

level spectroscopies, which are easier to analyse than the valence band. On copper instead it is the Fermi level that remains constant, reflecting a stronger molecule-substrate interaction. Another interesting study was published by Zhao et al. [156] who showed by a combined STM measurement and theoretical calculation that in the case of weakly coupled metal/organic interfaces the key factor in the electronic level alignment is the interplay between the metal image potential and the molecular electron affinity. However it has been shown that this kind of interaction can be prevented by deposition of a graphene layer between the metal and the organic layer[1]. Also instead of metals conductive metal oxides can be used [86] as a contact layer.

Organic/Oxide Interface The organic-insulator interface becomes particularly important in OFET or OPV applications, where the charge carriers behaviour at this interface will dictate the functioning of the device [15]. Up to now the most popular choice for the gate in OFET is SiO_2 [110], but its low dielectric constant leads to different problems. Higher ϵ transition metal oxides have been used [149] to try to minimize the oxide film thickness. It was, however, shown that varying the capacitance of the film had different effects depending on the architecture [160], or polymers [151]. It was shown that upon irradiation with light pulses longer than the characteristic transit time of a charge in the channel a transient photocurrent is formed at the organic-insulator interface. This current can be tuned by changing the insulator, or the semiconducting layer thickness. This could help tackling problems like low mobility, and high exciton binding energy in OPV [65]. Another way transition metal oxides can be used in organic devices is as contact materials. In this case particular care has to be taken on the energy level alignment with these of the OSC. In particular a crucial role is played by the oxide work function, and how it aligns with the HOMO-LUMO of the molecular layer [60]. In particular a crucial role is played by oxygen vacancies and their capacity to tune the position of the Fermi level as shown for MoO_3 often in OPV [22].

Organic/Organic Interface The semiconducting layer is often composed of a blend of two different organic materials. It can be a mix between donor and acceptor or an active layer in contact with a transport layer, both being OSC. In such "all organic" devices the organic/organic interface has to be inspected. From what was said before it is clear that the mutual orientation of the molecules is crucial. It can be controlled by balancing the molecule/substrate (mostly charge transfer) and the molecule-molecule interaction (π-π interaction, hydrogen bond or even covalent bonds) [159, 66]. Also more subtle effect can come into play: it was demonstrated that a difference in polarizability between the molecules forming a bulk heterojunction (BHJ) can lead to a difference in the electrostatic landscape seen by the excitons, and influence the splitting of the latter. Also it was shown that the diagonal disorder (i.e. the presence of different energy states at the interface between the two

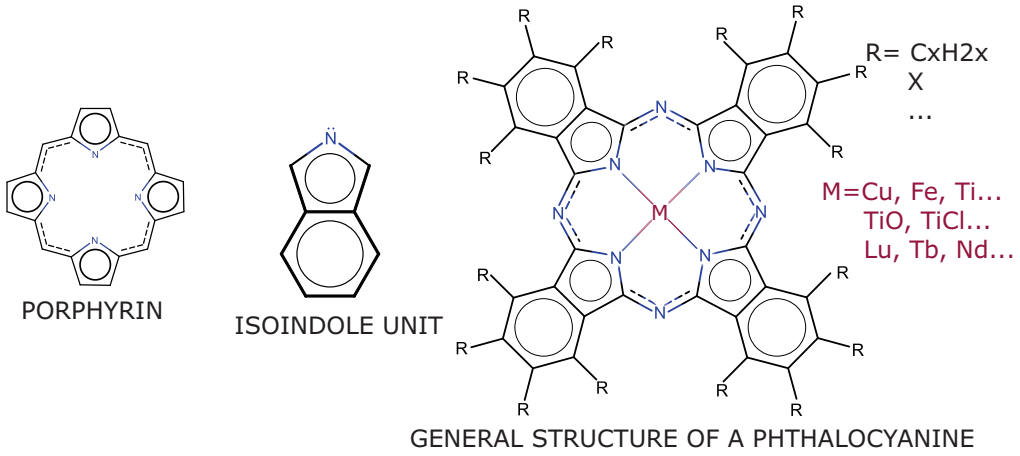

FIGURE 1.9: Structure of porphyrin (left), isoindole unit (centre) metal phthalocyanine (right).

organic moieties) can increase the number of exciton dissociation paths, leading to more efficient charge separation [21]. A comprehensive review on organic-organic, in particular on BHJ was published by Lu et al. [89] while for the molecule-molecule heterojunctions (OOHs) another review is advised by Goiri et al. [57].

1.4 Phthalocyanines

Among organic semiconductors one of the most studied is represented by the group of phthalocyanines (PCs). This is due to the ease of preparation, interesting optical, as well as electronic and thermal properties, and the possibility to functionalize them in a variety of ways.

1.4.1 History

The name Phthalocyanine refers to a class of organic molecules similar of porphyrins as shown in fig. 1.9 left and right. They were first discovered by Braun and Tcherniac in 1907 at the South Metropolitan Gas Company in London while they were testing a synthetic route to produce a cyanobenzamide.
The first metal phthalocyanine was synthesized 20 years later (in 1927) by Diesbach and coworkers, who accidentally synthesized a compound to which the assigned the formula $C_{26}H_{18}N_6Cu$ which was remarkably close to the one for copper phthalocyanine ($C_{32}H_{18}N_8Cu$). Unfortunately they did not investigate further their discovery due to a lack of time.
In 1928 Dunworth and Drescher, while trying to prepare phthalimide from phthalic anhydride and ammonia, also synthesized iron phthalocyanine due to an impurity in the reaction vessel. They after characterized the chemical and physical properties of the compound, and in 1929 the first patent on the compound we now designate as phthalocyanine was submitted. It was only in 1933 that Prof. Linstead and coworkers published the first atomic structure of the iron and other phthalocyanines. From

there on the industrial interest in these molecules grew rapidly due to the ease and low cost of manufacturing, great thermal and chemical stability and interesting chromogenic properties, leading to the synthesis of multiple different phthalocyanine single, double, triple, substituted with a large diversity of different groups, with a metal, rare earth, metal oxide as a central ion.

1.4.2 Structure and properties of phthalocyanine

Pcs are planar aromatic macrocycles consisting of four isoindole (see Figure 1.9) units bound by 4 nitrogen atoms, called "azabridge". They present an 18 π-electron aromatic cloud delocalized over the entire molecule. The molecule therefore belongs to the D_{4h} point group. The central cavity of the macrocycle can contain two hydrogen atoms (metal-free Pc or simply H_2Pc, in which case the symmetry is reduced to D_{2h}), or a metallic cation (metal phthalocyanine, MPc) in the oxidation state +2 (the phthalocyanine anion being Pc^{2-} after the removal of the two hydrogen).
Phthalocyanine are resistant to high temperatures: most of them do not decompose up to 900 °C and are therefore suitable for sublimation. Also they are chemically stable: they are not attacked by concentrated nitric acid. This great stability is due to the strong stabilization by the large delocalized system which is unfavourable to break by removal of the metal cation or by oxidation/reduction by an acid/base.
In single crystals H_2Pc and MPc usually adopt the stable β phase (see Figure 1.10 (b)), a monoclinic phase with the molecules stacked in a herringbone-like structure with a stacking angle (defined as the angle between the normal to the molecular plane and the b axis) of $45°$ in the (001) plane, the symmetry group is the P 2_1/a. The unit cell for the metal-free phthalocyanine was found to be: a=19.85 Å; b=4.72 Å and c=14.8 Å, β=$122.25°$ [118] and only slightly dependent on the dimension of the central atom, which mostly influences the stacking distance along the b axis (out of the molecule plane). The macroscopic crystals have a needle shape and can be up to 1cm long (see fig.1.10 c)). Another known metastable phase is the α phase(see Figure 1.10 (a)), which is usually obtained after deposition on a substrate kept at room temperature. It is again a monoclinic phase with the molecule stacked in a herringbone-like structure, but this time along the (100) axis the stacking angle is $26°$ in the (100) plane, and the space group is C 2/n. The lattice parameters are a=26.14 Å; b=3.81 Å and c=23.97 Å, β=$91.1°$ [4]. Irreversible transition $\alpha \rightarrow \beta$ can be obtained by heating up the sample to 310 °C for H_2Pcs [152], showing the metastability of the phase.

Optical Properties The first interest on phthalocyanine was sparkled due to their bright blue/green colour. It is therefore important to describe their optical properties, as a mean to explain their molecular and electronic structure.
All phthalocyanines have similar optical properties, as shown in Figure 1.11, which implies that they are mostly due to the organic macrocycle, and have little contribution from the central metal atom [35]. In the UV visible four main absorption bands

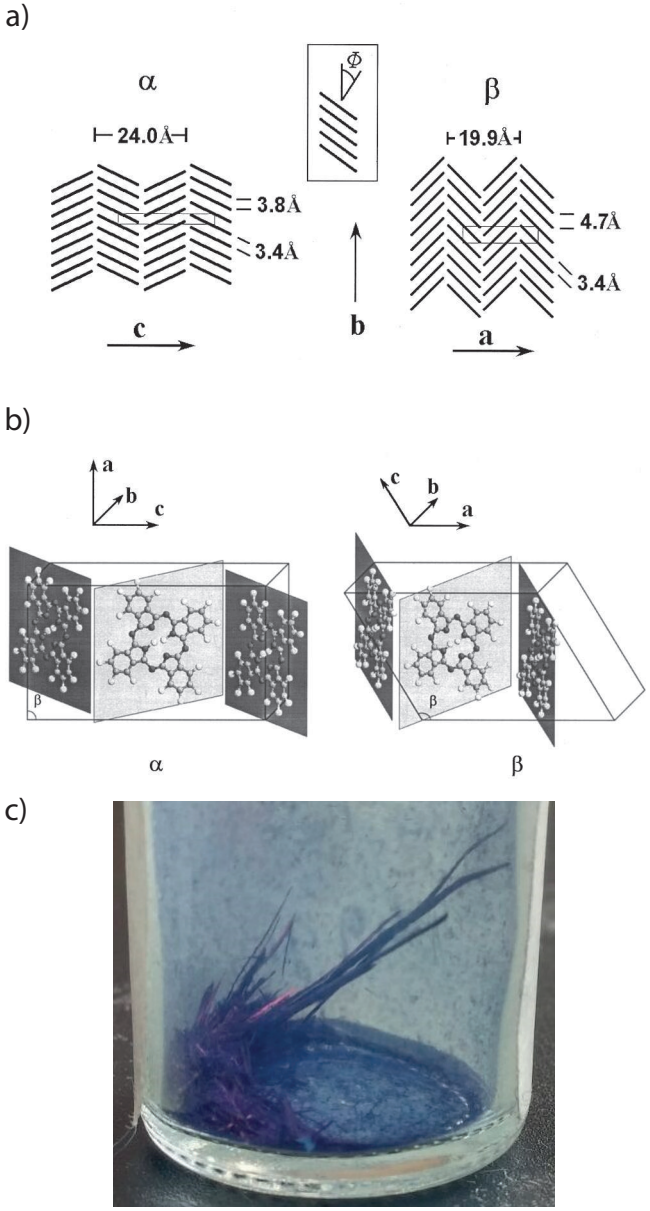

FIGURE 1.10: Crystal structure of the α and β phase of H_2Pc. (a) Schematic depiction of the α (left) and β (right) projected on the (100) and (001) plane respectively. (b) view of the molecular plane arrangement in the structure. c) needle like shape of crystals of CuPc. Image a) and b) taken from ref. [152].

are found: the Q Band around 1.8 eV (690 nm) and the B band (or Soret band, in analogy to porphyrins) around 3.9 eV (320 nm) are the two most intense. The relative electronic transitions were explained by Orti and coworkers [107], as both coming from different π-π* transitions.

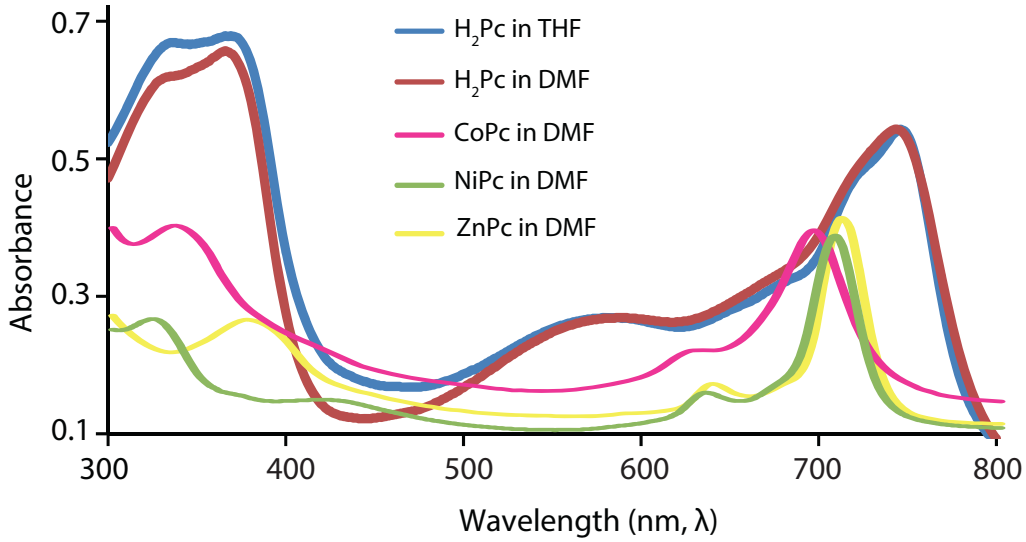

FIGURE 1.11: UV-Vis spectra of different phthalocyanine. Adapted from ref. [58].

1.5 Reactivity

The field of reactivity of organic and metallorganic thin films is not so developed, even though it could shred light on the causes that lead to the premature degradation of most of organic devices. Regarding phthalocyanine a few works have been published. Lozzi and coworkers [88] studied the effect of NO_2 doping on CuPc, showing by both theoretical and experimental methods the formation of a Cu-NO_2 (or NO, as they could not exclude dissociation of NO_2 in NO+1/2O_2) bond, with the oxidation the Cu atom which led to a charge transfer from the pyrrolic nitrogen atoms. Similarly it was shown by Flechtner and coworkers [48] that NO adsorbs on top of the Co atom in Co tetraphenyl porphyrin (TPP, an organic macrocycle similar to phthalocyanine). This also leads to a decreased electronic coupling between the Co atom and the silver substrate due to the so-called *trans effect*, which is a competition between two ligands in trans position which occupy the d_{z^2} orbitals. So when NO (which is considered a ligand with a strong trans effect) is added the bond with the Ag surface is weakened. Another interesting study on the reactivity of MPcs was published by Sedona et al. [123] who investigated the different reactivity of different phases of FePc deposited on Ag(110). They first shown by STM the presence of two different phases, a low density square phase, and a high density hexagonal phase. In a mixed theoretical and experimental work carried out at room temperature, they showed that oxygen is able to penetrate below a loosely packed (square phase) Pc monolayer and bind to both the underlying Ag surface atoms and the Fe atom in the Pc in a FePc-(η-O_2)-Ag chain, but the bond is metastable. The high density hexagonal

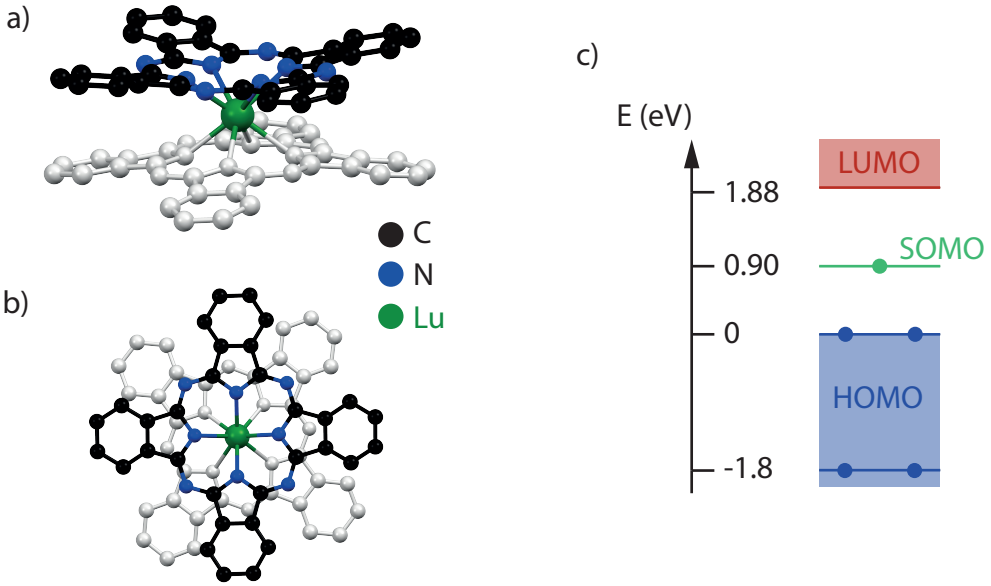

FIGURE 1.12: Ball and stick model of a lutetium bis-phthalocyanine a),b); schema of the electronic configuration of the frontier orbital of $LuPc_2$ c).

phase instead was found to be unreactive. Zhang et al. [153] studied the reactivity of MnPc towards activated N_2 molecules (which means that N_2 was dosed in presence of a heated filament, which can result in N, N^+, N^{2+}, N_2^+ or N_2*). They found that only neutral activated species (N*) are adsorbed on the central Mn atom, resulting in a reduction of electron density on the Mn atom (shown by STM images). Last Corva et Vesselli [32] studied the adsorption of CO on FePc deposited on Ir(111) at high pressure (1 mbar), showing the formation of a Fe-C-O bond formation (typical of metal-carbonyl bond), and more interesting, that a ML of phthalocyanine was sufficient to passivate the surface. This brief overview indicates that in single decker phthalocyanine, the reactive site is the central metal ion. It was shown by Flyagina et coworkers [50] by DFT calculations that the main factor to determine the reactivity of organic macrocycles towards ORR is indeed the nature of the central metal atom, while the nature of the surrounding macrocycle can just be used to tune the strength of the reaction. An older study by Ottaviano et al. [108] focused on the reactivity of naphthalocyanine towards oxygen. No metal atoms are present in this molecule, so in this case the reaction takes place on the central ring, and in particular on the azabridges nitrogen atoms.

1.6 Structure and Properties of Lutetium Bis-Phthalocyanines

Another group of Pcs is represented by the multi-decker Pcs, which are composed of two or more superimposed macrocycles linked by a metal cation caged in the middle, see Figure 1.12. The first of which to be synthesized was that of Sn in 1936. Most of the molecule belonging to this group are in fact rare earth (RE) phthalocyanine. In particular the first synthesis was proposed by Chang and Marchon in 1981 [23], but the first reliable method was found by Clarisse et Riou six years later [26], following the reaction in the formula 1.2.

$$Lu(CH_3CO_2)_3 + C_6H_6(CN)_2 \rightarrow LuPc_2 + H_2Pc \tag{1.2}$$

In these molecules the RE 3+ cation is sandwiched between the two macrocycles. This is due to the big atomic radius of the cation (ranging from 111 pm for Lu(III) to 130pm for La(III) while for example it is just 74 pm for Pt(II) [69]) it cannot be accommodated inside the phthalocyanine ring (which has a cavity diameter of around 3.9 Å [135]). It was shown by De Cian et coworkers [36] that the bonds between the central cation and the 8 pyrrolic nitrogens are all equivalent, leading to an eight-fold coordination for the RE cation, which is the most common for RE complex. The interaction with the central metal atom leads to a distance between the two rings of 2.7 Å, which is smaller than the Van der Waals distance (3.4 Å). This leads to a strong repulsive interaction between the two macrocycle, in particular between the benzene rings. To reduce the overlap between the two electronic clouds, and the consequent electrostatic repulsion the two rings are in a staggered position, leaving the central cation in a square antiprismatic coordination [20]. Bis-phthalocyanines are also slightly domed due to the RE cation-pyrrolic N attraction and the electronic repulsion between the rings, which leads to a bending of the pyrrole units. Moreover a slight bending of the pyrrole unit towards the inner cation leads to a better overlap between the N sp^2 and the Lu 3d orbitals, leading to an increased strength of the σ N-Lu bond [107]. This coupled push-pull interaction is strong enough to force the ring out of planarity, and therefore reduce the stabilization by the aromatic electron cloud. Another difference with the simple phthalocyanine is in the electric charge of the ligands. The first double phthalocyanine was, as said, $SnPc_2$, with a Sn(IV) cation. However RE cations only have a RE(III) stable configuration. It was shown by Orti and coworkers that the two rings split equally the charge, thus formally being written as $Pc^{1.5-}$. This would lead to a D_{4d} symmetry group. However it has been shown experimentally [36] that the two rings are staggered by an angle $\neq 45°$. This is due to the Ian-Teller effect, which forces a molecule to have a less symmetrical stable state to remove the degeneracy at the ground state and reduce the total energy, which leads to a D_{4h} symmetry.

What drove the interest on this kind of molecules are mostly their electronic properties. The 3+ cation leads to an imbalance in the filling of the electronic levels, leading

to a Semi Occupied Molecular Obrital (SOMO) between the HOMO (Highest Occupied Molecular Orbital) and the LUMO (Lowest Unoccupied Molecular Orbital), as displayed in Figure 1.12c). This peculiar feature also allows the molecule to be easily oxidized and reduced, as the energetic cost of adding an electron is weak (only e-e repulsion in the SOMO, no new orbital occupancy), as well as the energetic gain of removing one is great (the whole most energetic orbital is emptied). Also this ease in adding or removing an electron makes the molecule a good organic semiconductor, as every molecule can be the either a target either a departure for hopping following this equation:

$$2LuPc_2 \rightleftharpoons LuPc_2^- + LuPc_2^+ \rightleftharpoons freecarriers \tag{1.3}$$

In fact $LuPc_2$, on which this work is focused, were the first described organic intrinsic semiconductor [14], where the concentration of charge carriers depends on the oxidation/reduction of the molecular unit, see Equation 1.3.

The optical spectrum of $LuPc_2$ is shown in Figure 1.13(a), showing 4 different absorption bands, at around 320 nm (3.9 eV), at 480 nm (2.8 eV), 680 nm (1.9 eV), and at 920 nm (1.5 eV). To explain these transition it is important to know the energy position of the molecular orbitals. The electronic properties of the molecule have been studied by means of UPS [19], IPS [101] and different theoretical calculations, Valence Effective Hamiltonian [107], DFT [101, 10], or extended Hückel [120]. All studies agree that the frontier orbitals have little to no contribution from the central Lu cation (see in particular [101]). Instead the orbitals are localized on both the phthalocyanine ring, as is shown in Figure 1.13(c). The only major contribution of the central cation is due to its size. Orti and coworkers [107] showed that the interaction between the two phthalocyanine rings is important, as it induces a lift of the degeneracy of the frontier orbitals of the two different macrocycles. Further the delocalization of the electronic states is a consequence of this strong interaction. The distance between the two rings was shown to depend on the size of the central cation [100]. It is clear from what stated here that the optical properties of the molecule mostly depend on the delocalized π system, as is shown from the transition assignation in figure 1.13. From there we can start assigning the optical transition to electronic transition, as shown in Figure 1.13 b). The band at 3.9 eV is called the B band, which is related to π-π transitions. The band at 2.8 eV is called the Charge Transfer band, which correlates electrons from an σ orbital (mostly localized on the N atoms) to an π orbital, localized only on the pyrrolic carbons. The band at 1.9 eV, called the Q band, is an intermolecular charge transfer from the orbitals that are mostly centred on the pyrrolic carbons to the lowest unoccupied orbitals, which are mostly localized on the nitrogen atoms (both pyrrolic and azabridge). Last the large band centred at 1.5 eV is due to another π-π transition, but this time is between a ring-ring bonding orbital and a ring-ring antibonding orbital.

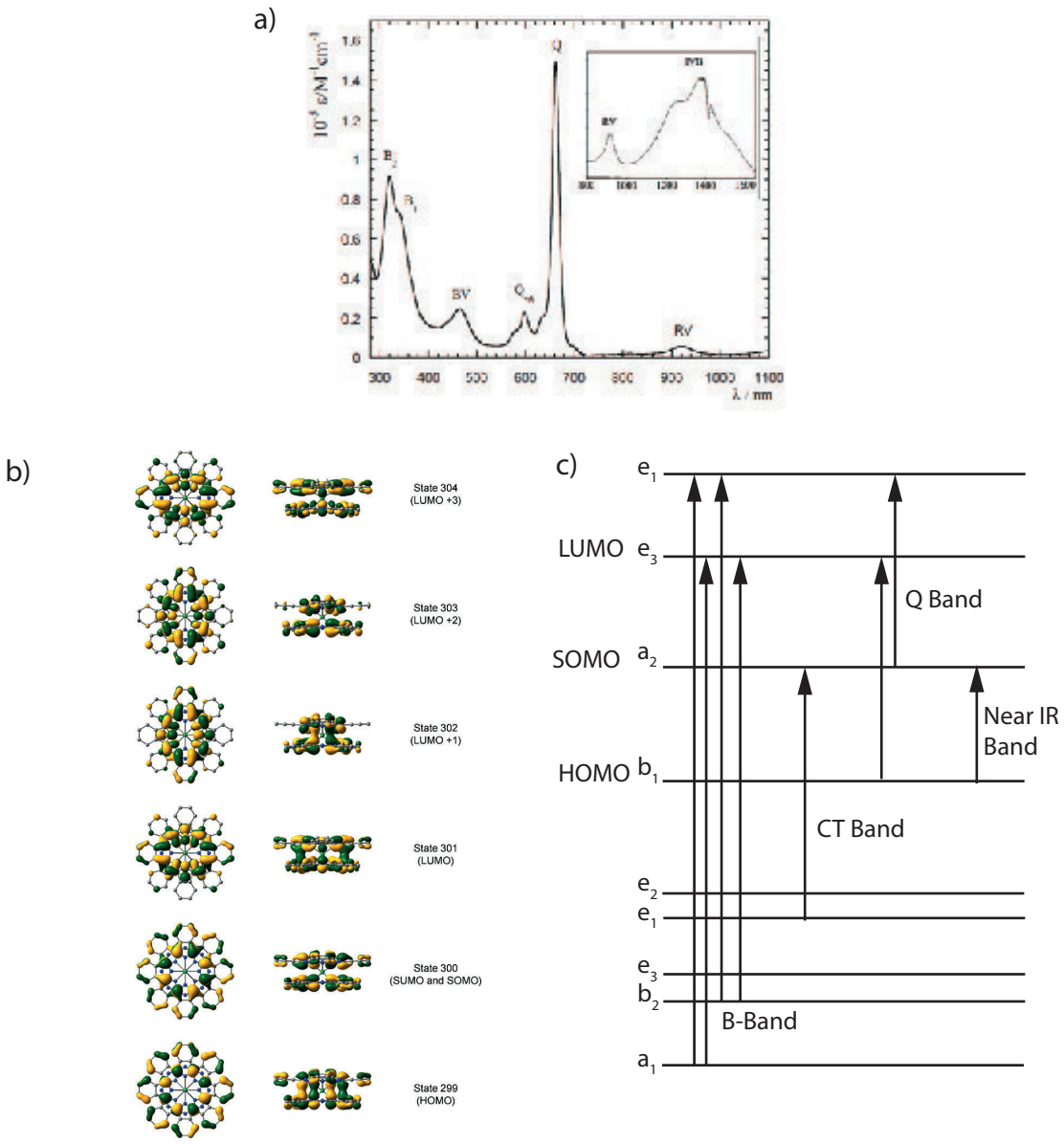

FIGURE 1.13: Optical absorption spectra of the molecule in dichlorometane (a); Frontier orbitals for $LuPc_2$ as calculated by DFT (b); spatial localization of the frontier orbitals(c). (a) taken from ref. [12]; (b) adapted from ref. [120] and (c) from ref. [101].

Chapter 2

Experimental

2.1 Ultra High Vacuum

2.1.1 General considerations

The Ultra High Vacuum (UHV) is a condition where the pressure is below 10^{-8} mbar. This condition is necessary for the study of the surface as the time constant τ for the deposition of a monolayer (ML) of contaminants depends on the pressure, by the relation:

$$\tau = n_0 \frac{\sqrt{2\pi m k_B T}}{p} \tag{2.1}$$

where n_0 is the atomic density of the overlayer, k_B is the Boltzmann constant, p is the pressure and T the absolute temperature [109]. At a pressure of 10^{-9} mbar τ=1 hour (with n_0 assumed to be $1{\cdot}10^{15}$cm^{-2}), so to keep the surface clean during a normal experiment time scale (from some hours to some days) the pressure has to be reduced below 10^{-10} mbar. It has to be noted that this calculation implies a sticking coefficient (the probability that an impinging molecule is retained on the surface [73]) of 1, which is quite high, and close only to the value of gases on very reactive surfaces (CO or O_2 on Ti at room temperature have a value of 0.9 and 0.95 respectively [73]), while the range can vary of some orders of magnitude. Another reason is that a lot of the most popular surface science techniques employ electron beams (Scanning Electron Microscopy, Low Energy Electron Diffraction and Microscopy, X-ray Photoelectron Spectroscopy, etc...) which would be scattered by gas molecules, the mean free path λ of a molecule being given by the equation [109]

$$\lambda = \frac{RT}{\sqrt{2}\pi d^2 N_A p} \tag{2.2}$$

where d is the molecular diameter (cross section), R the perfect gas constant and N_A is Avogadro's number. This means that for a pressure of $1{\cdot}\ 10^{-9}$ mbar the mean free path is of the order of magnitude of a few km, which implies that the reactions take place on the surface and not in the gas phase.

2.1.2 Pumping Systems

Achieving such conditions is a technological challenge. The whole experiment takes place in a sealed stainless steel chamber. Stainless steel (usually AISI 304) is chosen due to its poor permeability to gases, and consequently to its low gas release when exposed to vacuum. Ultrahigh vacuum is obtained by different pumping system:

- Primary pumping (from atmospheric pressure to 10^{-4} mbar): is most of the time made with rotary pumps, where an eccentric rotor rotates in the vane to compress and expel the gas. These pumps employ vacuum oil as a sealant and a lubricant, so it is necessary to be careful when switching them off, to avoid oil reflux in the camber. Other kinds of primary pumps such as the screw, and the diaphragm pumps can be used alternatively.

- Ion pumping (from 10^{-5} mbar to 10^{-11} mbar): they are composed by two titanium plates mounted close to the entrance of the pump that work as a cathode and an anode. Two magnets are mounted perpendicular to the cathode-anode axis. The high electric field between cathode and anode leads to field emission, and the electrons move towards the cathode in a spiral trajectory due to the magnetic field. They then ionize gas molecules, which are accelerated onto the cathode, and then buried in it. As this pump is not evacuated, it has to be regenerated by thorough heating to desorb the gas molecules. Since the advent of turbomolecular pumps their use has been limited for pressures below 10^{-8} mbar.

- Turbomolecular pump (from 10^{-3} mbar, now some models even from ambient pressure, to 10^{-10} mbar): it is a momentum transfer pump, composed by a serie of alternating rotors with multiple blades angled towards the exit and stators invertedly mounted. Both are suspended in the housing via a permanent magnet, to avoid friction in absence of lubricants. The rotors are turning at around 1 kHz, and the effect is to push gas molecules from the entrance to the exit. Therefore a molecular flow is needed for the optimal working of the pump, as the momentum gained by the molecule hitting the rotors' blades is not dispersed via collisions with other molecules. As it is a momentum transfer pump, the compression rate (ratio between the exit and entrance pressure) is strongly dependent from the considered gas: 10^8 for N_2 and 10^3 for He or H_2. Also a finite compression ratio means that the exhaust of the pump must be at his turn pumped (usually with a primary pump, or even with a combination of a smaller turbomolecular pump and a primary pump) to achieve UHV.

- Titanium sublimation pumps (TSP) are auxiliary pump used from time to time to maintain UHV. Titanium is sublimated on a shield by passing a high current (up to 40 A) through a Titanium rod. When it deposits on the shield, it is then able to react with oxidizing gases such as O_2 and H_2O removing them from the chamber.

All these systems allow to achieve pressures around 10^{-8} mbar, but to reach UHV another step is needed. When the chamber is opened to the atmosphere (to modify the experimental setup, or to repair broken parts) water from the atmosphere will adsorb on the chamber's wall. To prevent this from happening the chamber is usually filled with Nitrogen or Argon gas prior to the opening, which will saturate the walls and reduce water adsorption. To completely remove water from the walls a thorough heating (bake out) of the whole chamber has to be performed. During this procedure the whole camber is heated up to around 150 °C while pumped with turbomolecular pumps to desorb and evacuate gas molecules from the walls.
Following carefully all these steps allows to reach UHV in the 10^{-11} mbar range.

2.1.3 Monitoring vacuum

The pressure inside the camber is usually measured via ionization gauge, where the gas molecules are ionized, and accelerated towards an anode via a potential (usually $\sim$100 V, the ion current on the cathode is therefore proportional to the gas pressure. The ionization can take place via a hot filament (ion gauges), or via a glow discharge (cold cathode). Of course another really important parameter that influence the current reading is the gas composition, and in particular the ionization probability of the molecules that compose it. Therefore Ion gauges are usually calibrated on a single gas (usually N_2).
Another fundamental tool is the Quadrupole Mass Spectrometer. It is composed of a hot filament to ionize gas molecules and a quadrupole analyser to select ions via the $^q/_m$ ratio, thus measuring the composition of the gas inside the chamber. It is not only useful to measure the purity of gas dosed into the chamber, but can also be used to detect leaks.

2.2 Experimental techniques

Here are briefly introduced the experimental techniques used during this work.

2.2.1 Synchrotron radiation

The use of synchrotron radiation greatly improved the quality and the amount of information that can be obtained with a lot of different techniques, in particular surface science related techniques, as X-ray Diffraction (XRD) and X-ray Photoemission Spectroscopy (XPS), while allowing the introduction of completely new techniques like X-ray Absorption Spectroscopy (XAS). The interest in synchrotron radiation is due to its high brilliance (which is defined as the number of photons per second, per angular divergence, per area of the beam, per 0.1% of the wavelength bandwidth, and is a measure of how many photons can be concentrated in a defined

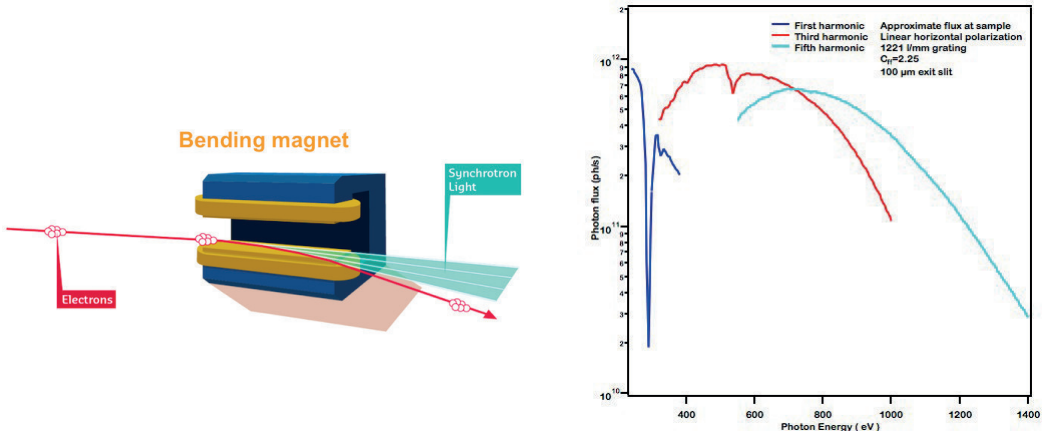

FIGURE 2.1: Working principle of a bending magnet (left); Emission spectrum of the bending magnet at the I1011 at Maxlab (right).

area), the tunable photon energy, high monocromaticity, high level of polarization, pulsed emission.

Insertion devices Depending on architecture of the insertion devices three different categories can be differentiated: undulators, wigglers and bending magnet [18].

- Bending magnet: They are placed along the ring where their principal task is to bend the charged particles (invariably electrons or positrons, as the emitted power depends on the inverse of the mass, see below) along the circular trajectory of the synchrotron [95]. The emitted power P is proportional to the square of the acceleration a, which in turn is proportional to ω_L, the cyclotron frequency ω_L=e$B_L/\gamma m_0$, where B is the applied magnetic field, γ=1/$\sqrt{1-v^2/c^2}$ and m_0 is the rest mass of the particle. The emission spectrum of a bending magnet is influenced by the short emission time, i.e. the time an electron passes in the range of the magnet itself. In fact the maximum frequency is the reciprocal of the emission time, giving rise to the plot shown in Figure 2.1. in a broad and continuous spectrum, but poorly focused and with low intensity.

- Wiggler: it works as a series of bending magnets, so the obtained spectrum is broader. A great improvement respect to the bending magnet is the possibility to increase the magnetic field, which expands the obtainable energies.

- Undulator: Electromagnetic radiation is emitted by charged particles which are accelerated by a magnetic field. In particular the electron which circulates

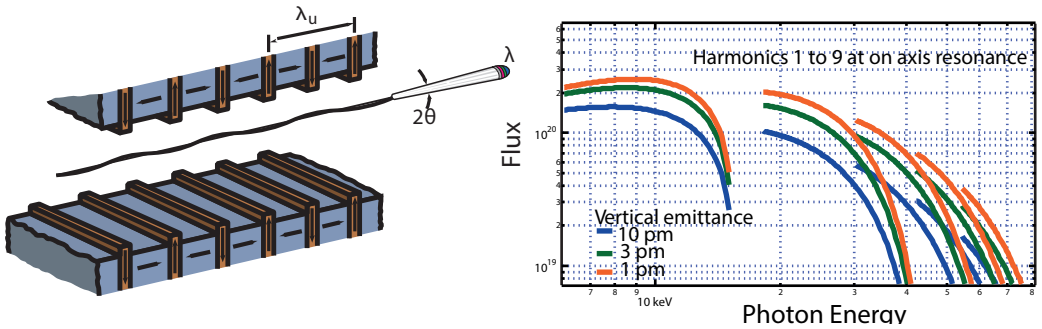

FIGURE 2.2: Schematic of an undulator (left); Intensity as a function of the chosen harmonics (right).

in the ring encounter straight sections where magnets of alternating polarization are placed. The electron (which is moving respect to the magnets) therefore sees an electromagnetic wave of wavelength λ=L/γ where L is the period of the undulator. The radiation is emitted at every bending, and interfere with that of the preceding generating a much more intense, collimated (the angular spread varies with $\sqrt{N}$, where N is the number of periods) and monochromatic (the energy dispersion varies with 1/N) beam than the bending magnet. The gap of the undulator can be finely tuned to vary the photon energy following the equation: $\lambda = \frac{L}{2\gamma^2 n}\left(1 + \frac{K^2}{2} + \gamma^2\theta^2\right)$ where n is the harmonic number, K=$\gamma\delta \approx B_0(T)\lambda_w$ (B_0 is the magnetic field, and L is the undulator period) and θ the emission angle. From this equation it is apparent that for a low applied magnetic field only the fundamental (n=1) harmonic is present, while for a strong magnetic field a large number of harmonics appears, leading to an almost continuous spectrum (similar to the one of the bending magnet) appears (see Figure 2.1).

A few factors have to be taken into account that can modify the wavelength:

- the relativistic Doppler effect, which depends from the angle θ, adds a correction factor (1+γ^2 θ^2)
- the movement of the electron in the undulator reduce the average x component of the velocity, leading to a correction to γ and ultimately to λ of a factor (1+bB^2)

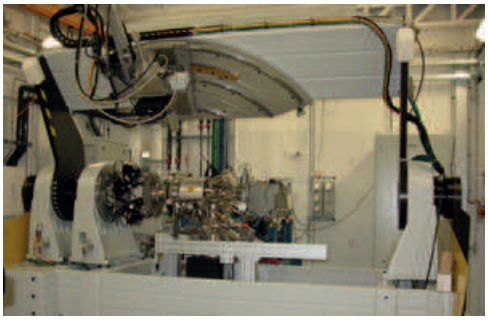

FIGURE 2.3: Photo of the UHV diffractometer on the SIXS beamline.

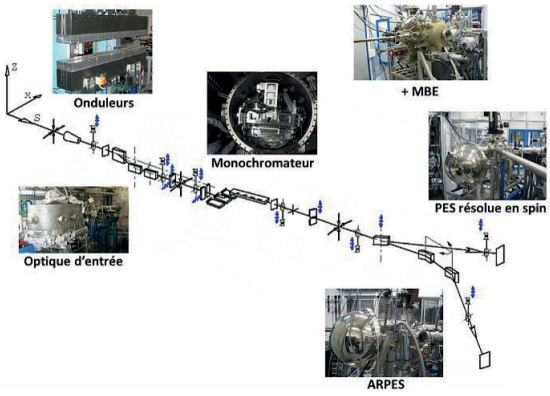

FIGURE 2.4: Image of the optics on Cassiopée beamline.

Instrumentation Three different synchrotrons have hosted the experiments presented in this work: SOLEIL (France), Max-IV (Sweden), Elettra (Italy). They all are 3rd generation synchrotrons, meaning that the ring is composed by alternating bending and straight segment where the insertion devices are incorporated. This allows to achieve a high brightness and high coherence.

Beamline SIXS at SOLEIL SIXS is a beamline dedicated to structural studies on surfaces by means of Grazing Incidence X-ray Diffraction (GIXD), Grazing Incidence Small-Angle X-ray Scattering (GISAXS), X-ray Reflectivity (XRR). The insertion device is an undulator U20 (20 mm gap). The beamline couples a UHV chamber (consisting of 3 separate chambers: one dedicated to sample preparation, one equipped with an STM and the diffraction chamber) to a diffractometer, see Figure 2.3. The sample is mounted on an exapode which allows a fine positioning of the sample, with precision of 0.0002°. The beam size on the sample is around 30x30 um^2.

Beamline Cassiopée at SOLEIL Cassiopée is a photoemission spectroscopy beamline (spin resolved and angle resolved) at SOLEIL synchrotron. The insertion

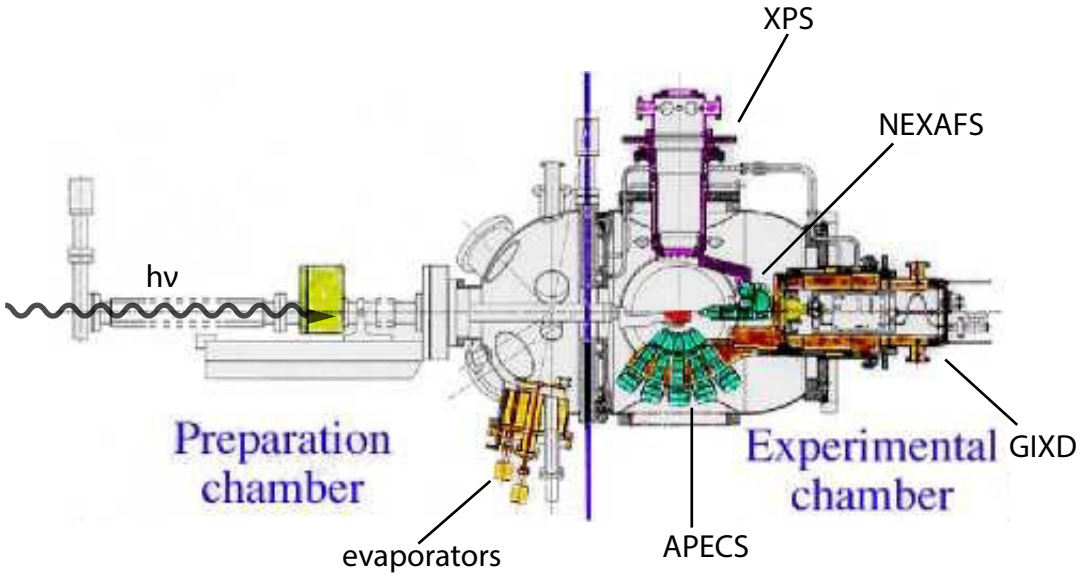

FIGURE 2.5: Image of the geometry at beamline Aloisa.

device is composed by two different undulators: one for the low energy with a period of 256 mm and one for the high energy with a period of 60 mm with an energy range of 90-1000 eV (during our experiment only the one for the high energy was used). The beam size on the sample depends on the photon energy, but is always in the range of ten microns. The analyser is a Scienta R4000 multichannelplate.

Beamline Aloisa at ELETTRA Aloisa is a multipurpose beamline for photoemission, photodiffraction, X-ray absorption and He Atom Scattering[49]. The newly installed undulator, while allowing easier movimentation and better stability, drastically reduced the energy range from 100-8000 eV to 130-1500 eV, hindering the possibility to do X-ray diffraction. The X-ray beam impinges on the sample at a grazing angle, variable between 0 and 20°. Photoemission spectroscopy spectra is measured with a 66 mm homemade electron analyser with a 2D delay line. NEXAFS is acquired via a channeltron with a retarding grid to remove secondary electrons. Rotation of the manipulator along the beam axis allows to measure NEXAFS in different polarizations.

Beamline D1011 at Max-IV The D1011 is a photoemission and photoabsorption beamline at MaxIV Laboratory [105]. The insertion device is a bending magnet covering the energy range from 30 to 1600 eV. The beam can be linearly or elliptically polarized. The photoelectron analyser is an upgraded Scienta SES200 hemispherical electron analyser. X-ray Absorption can be measured in partial electron yield (see 2.2.3) via multi-channel plates or total electron yield via multi-channel plate or by directly measuring the sample current.

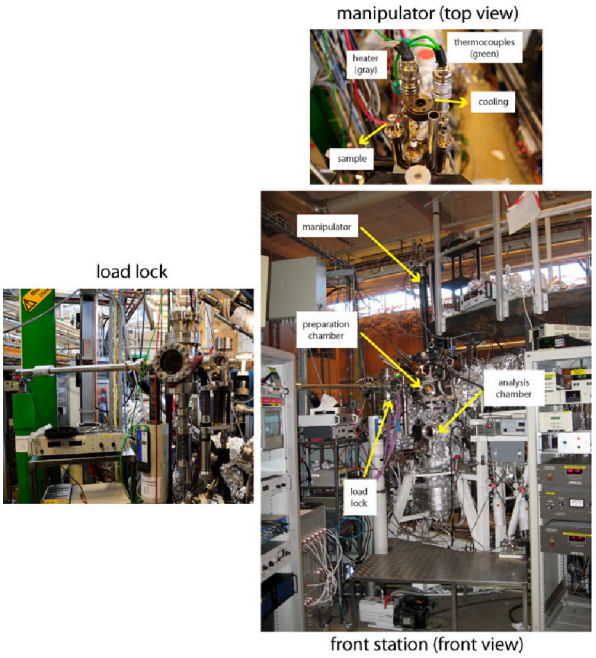

FIGURE 2.6: Photo of the cooling system at the D1011 beamline.

2.2.2 X-ray Photoemission Spectroscopy

X-ray Photoemission Spectroscopy (XPS) is a powerful analysis tool for surface science, which allows to study the chemical properties of a sample.
It is based on the photoelectric effect, explained by Einstein in 1905 [43], which states that when a material is shined with a sufficiently energetic light it will emit electrons, following the energy conservation principle stated in the following equation:

$$E_K = h\nu - E_B - \phi_{sample} \tag{2.3}$$

where hν is the energy of the incident photon, E_K is the kinetic energy of the emitted electron, ϕ_{sample} is the work function of the sample, and E_B is the binding energy of the electron inside the atom. The binding energy is a measure of the energy needed to eject an electron, i.e. how "bound" an electron is to a nucleus, and is specific of a single orbital in a single atom, therefore XPS is sensitive to the chemical composition of the sample (see Figure 2.7). It has to be noted that a photoelectron to escape from the sample has to overcome a barrier equal to $BE + \phi_{sample}$, but to be analysed it needs to be injected in the channeltron of the analyser, which in turn has a work function $\phi_{analyser}$, therefore a contact potential equal to $\phi_{sample} - \phi_{analyser}$ is present when the sample and the analyser are put in electrical contact. This means that all the measured kinetic energies are shifted of a value $\phi_{sample} - \phi_{analyser}$. This can be tackled by calibrating all the binding energies to the Fermi level, which is, of course, independent of the work function, and is the same for sample and analyser.
Equation (2.3) is called Koopmans' equation [76], and the so calculated E_B is the

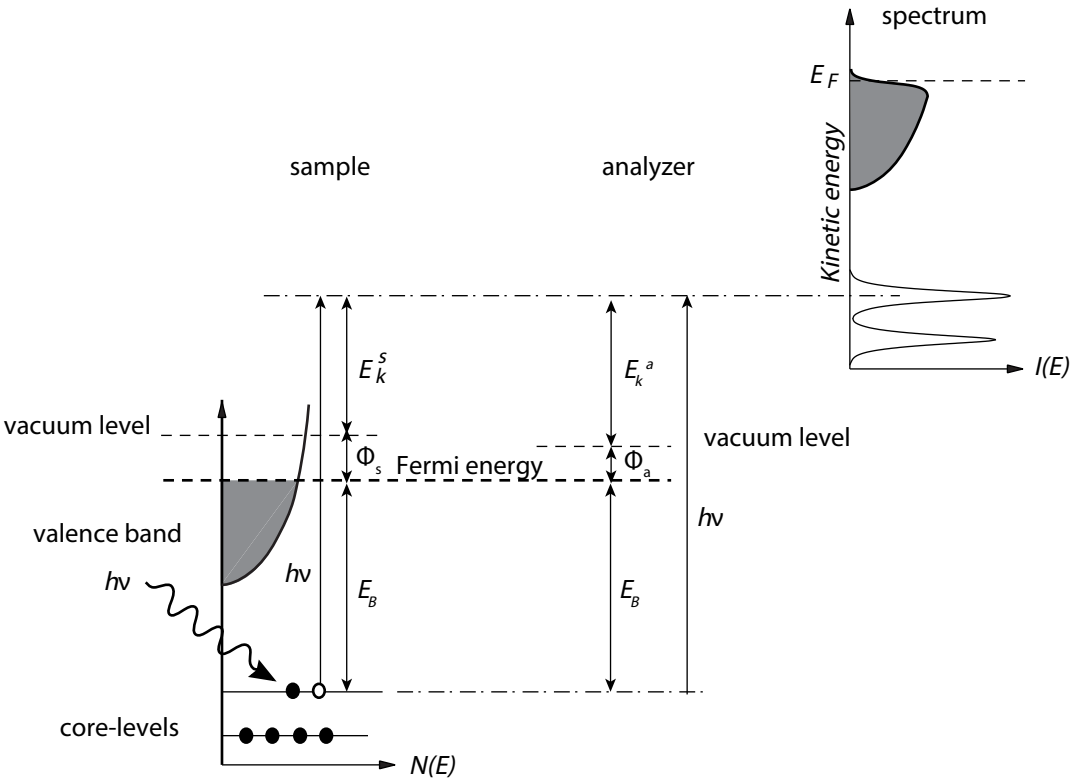

FIGURE 2.7: Relation between the energy levels in a solid and the photoemission spectrum obtained for photons of energy hν. The energy scale is set to 0 at the Fermi level.

Koopmans' binding energy. The underlying assumption is the so-called "sudden approximation" which states that the emitted photoelectron does not interact with the system while escaping from the solid (which works better at high photon energies) and that all the relaxation phenomena are instantaneous. Under this approximation the photoelectron intensity is proportional to the transition probability (W) (which is proportional to the signal intensity I) can be calculated from the Fermi golden rule [68]

$$I \propto W = \frac{2\pi}{\hbar}|\langle\Psi_f|\mathbf{\Delta}|\Psi_i\rangle|^2\delta(E_f - E_i - \hbar\omega) \tag{2.4}$$

where Ψ_f and Ψ_i are the initial and final state eigenfunction, and the second term is a Dirac function for the energy conservation with E_f the final state energy, E_i the initial state energy and $\hbar\omega$ the energy of the photon. The system is ultimately described by the product of the wavefunction of the leaving electron and the wavefunction describing the remaining electrons:

$$\Psi_i = \phi_i^k \Psi_{i,R}^k(N-1) \tag{2.5a}$$

$$\Psi_f = \phi_f^{E_k} \Psi_{f,R}^k(N-1) \tag{2.5b}$$

If we substitute them in Equation,(2.4) we obtain Eq.(2.6)

$$\langle\phi_f^{E_k}|\mathbf{r}|\phi_i^k\rangle\langle\Psi_{f,R}^k(N-1)|\Psi_{i,R}^k(N-1)\rangle \tag{2.6}$$

If we consider that the wavefunction describing the remaining electrons remains unaltered before and after the photoemission process (i.e. $\Psi_f^k, R(N-1) = \Psi_i^k, R(N-1)$), the so-called Frozen Approximation, than the overlap integral becomes unity, and the remaining matrix element is exactly the energy calculated with the Koopmans' formula in Equation (2.6). Of course these approximations are too extreme as they do not take into account the relaxation of the system (final state effect) after the creation of a highly energetic core hole. In this case we also have to evaluate the same integral over all the -s possible final states

$$\sum_s \langle \Psi_f^k, R(N-1) | \Psi_i^k, R(N-1) \rangle \tag{2.7}$$

and every -s state which gives a non-zero result in the overlap integral will give rise to an additional line.

Between the final state effect of particular importance are the plasmonic resonances, which give rise to the asymmetric peaks in metal spectra [40], shake-up and shake-off (see below), charge transfer satellites and others.

Another major effect is the one which causes the so-called chemical shifts. This is an initial state effect, as it is due to the situation of the atom before the photoemission process takes place. In particular considering a heteronuclear bond (for example a metal oxide molecule M-O) the two involved atoms will have a difference in electronegativity, which will lead to a charge disparity between the two (M^{2+}-O^{2-} for example). In particular the metal (oxygen) atom will be surrounded by a smaller (bigger) electron density than in the neutral form. This leads to an overall more positive (negative) potential acting on the remaining electrons which in turn leads to a change in potential leads to an increased (decreased) ionization energy, hence an increased (decreased) binding energy. This difference in binding energy is the so-called Chemical Shift, which allows to discriminate the oxidation state of the species that compose the sample. This can be rationalized in the following equation:

$$E_B = K \cdot Q + L + E_R \tag{2.8}$$

with E_B the binding energy, K and L are two constants and Q is the charge on the atom, E_R is the relaxation which is the energy regained from the reorganization of the N-1 electrons remaining in the system.

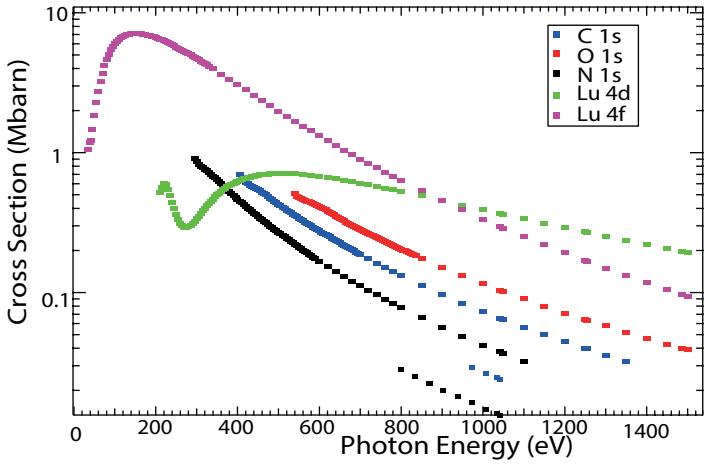

FIGURE 2.8: XPS cross section taken from ref. [150].

The intensity of a photoemission peak (measured as a number of detected photoelectron as a function of the kinetic energy N_k) is calculated as follows:

$$dN_k = \left[\begin{array}{l}\text{X-ray flux}\\ \text{at x,y,z}\end{array}\right] \times \left[\begin{array}{l}\text{Number of atoms}\\ \text{in dx dy dz}\end{array}\right] \times \left[\begin{array}{l}\text{Differential cross-}\\ \text{section for k subshell}\end{array}\right]$$
$$\times \left[\begin{array}{l}\text{Acceptance solid angle of}\\ \text{electron analzer at x,y,z}\end{array}\right] \times \left[\begin{array}{l}\text{Probability for no-loss}\\ \text{escape from specimen}\\ \text{with negligible}\\ \text{direction change}\end{array}\right] \times \left[\begin{array}{l}\text{Instrumental}\\ \text{detection}\\ \text{efficiency}\end{array}\right] \tag{2.9}$$

- the [X-ray flux at x,y,z] is the brilliance of the flux divided by the attenuation of the X-ray in the solid. It has to be pointed out that, as the penetration depth of the X-ray in a material is big compared to other terms (in particular the escape depth of the electrons), from a few um to a few mm, this term is often neglected. It can be calculated as: $I_0 \exp\left[-\frac{z}{\lambda_x sin\phi}\right]$ where λ_x is the attenuation length and ϕ is the entrance angle.

- the [Number of atoms in dx dy dz] can be calculated as $\rho(z)(dxdydz)$ where ρ is the material density at the depth z.

- the [acceptance of the electron analyser] can be thought as the probability that an electron from the -k orbital is emitted from the sample with a specific angle (θ) and collected from an analyser with an angular acceptance (Ω). If we then imagine the total cross section (σ_{nl}, the ratio between the impinging photons and the emitted photoelectrons, see Figure 2.8) to be related to the differential cross section $\left(\frac{d\sigma_k}{d\Omega} = \frac{\sigma_{nl}(E_k)}{4\pi}\left[1 - \frac{1}{2}\beta_{nl}(E_k)\left(\frac{3}{2}cos^2\alpha - \frac{1}{2}\right)\right]\right)$, where β_{nl} is the asymmetry parameter that characterizes the angular distribution of the

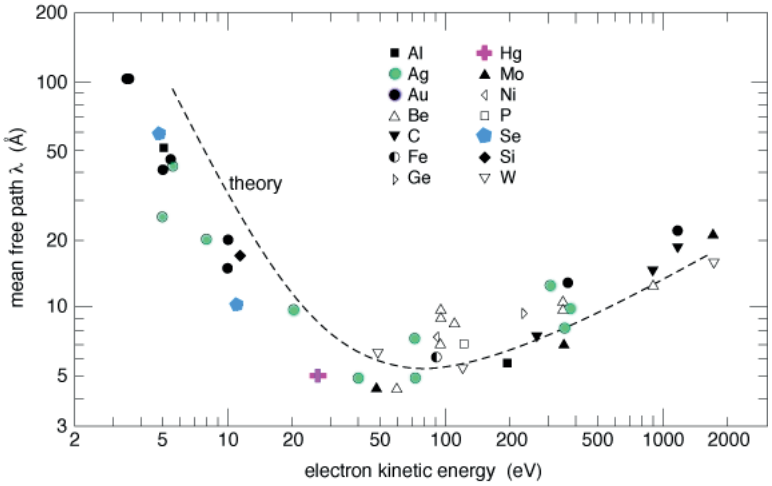

FIGURE 2.9: "Universal curve" for the inelastic mean free path, taken from Ref. [68].

emitted photoelectrons, and depends from the orbital studied (is 2 for an s orbital, and varies for p, d, f...) and α is the angle between the impinging X-ray and the emitted photoelectron.

- the [probability for the electron to escape without scattering events] depends on the electronic kinetic energy and also on the inelastic mean free path λ_e, which takes into accounts the inelastic scattering of the photoelectrons by the electrons of the material. The angle dependence shows the surface sensitivity of the sample. Here in Figure 2.9 a display of the value of λ_e for electrons in different solids [137] is presented. It can be calculated as $\exp\left[\frac{-z}{\Lambda_e sin\theta}\right]$.

In the end Eq.2.9 can be rewritten as follows:

$$dN_k = I_0 exp\left[-\frac{z}{\lambda_x sin\phi}\right] \rho_z(dxdydz) \left(\frac{d\sigma_k}{d\Omega}\Omega(E_k,\theta,x,y)\right) exp\left[\frac{-z}{\Lambda_e sin\theta}\right] D_0(E_k) \tag{2.10}$$

Shake-up phenomena Among the different processes that can reduce the energy of the outgoing photoelectron there are the shake-up and shake-off phenomena. They both refer to an energy transfer from the photoelectron to another valence electron, which, depending from the amount of energy transferred, can be promoted in an antibonding orbital (shake-up) or be ejected (shake-off). As they are related to a loss of energy, they always appear in the lower kinetic energy side of the spectrum, or in the higher BE side.

$$I \propto \langle \psi_{ijk}^{ion} | \psi_k^{rel}(N-1) \rangle \tag{2.11}$$

It is shown in Equation (2.11) that the shake up processes are driven by the overlap between the wavefunction relative to the frozen core hole and the one relative to a relaxation process involving a transition to the $-j$ orbital. This kind of phenomenon is

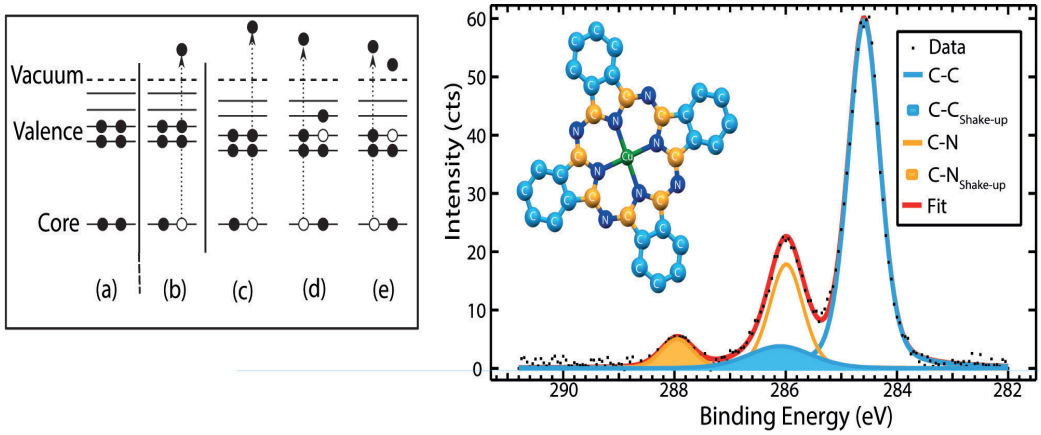

FIGURE 2.10: Left: schematic of the different de-excitation processes. (a) the unperturbed system, (b) the photoemission step, (c) the Koopmans' binding energy, (d) the shake-up process, (e) the shake-off process. Image adapted from ref.[8] Right: C 1s spectrum of CuPc deposited on Au/Mica. Inset: CuPc molecule.

well known in atoms and in metals [114], and can be addressed in a straightforward way. Also in simple molecules relatively easy calculations can lead to a consistent assignment of the shake-up peak, see for example the work from Rennie [116] and coworkers on the shake-up peaks of benzene. They were able to assign the different satellite in C 1s spectrum of benzene from the molecular orbitals. On more complex molecules calculations becomes important due to the greater number of inequivalent atoms and therefore of transitions. Scholl et al. [121] discussed the assignment of the shake-up peaks in different π-conjugated molecules functionalized with an electron acceptor group with the help of Singles and Doubles Configuration Interaction (SDCI) calculations. They were able to unequivocally assign the different peaks to different transitions, and were also able to show different factors influencing the intensity of the transition, namely the extent of the aromaticity which increase the intensity of the transition and lowers the peak - shake-up distance, the molecule polarity, which also increase shake-up intensity. Later Gao et al. [55] showed on different allotropic forms of carbon (C_{60}, C_{70} and carbon nanotubes) the different transitions that give rise to the shake up features, and also the electronic charge redistribution after the core hole excitation. Experimentally shake-up peaks are seen as additional peaks on the high Binding Energy side of the principal peak. Their separation from the principal peak depends on the energy of the excited transition. Their intensity depends on the oscillator's strength. In particular in Figure 2.10 the spectrum of C 1s in CuPc is shown. It presents three peaks, where the first one is due

to the benzenic carbon, the second one is due to the sum of a principal peak due to the carbon atoms bound to nitrogen atoms, and a shake-up peak due to the benzenic carbon, the third peak is due to a shake-up from the C-N peak.

Experimental details

Background removal Before the lineshape and the different components of an XPS peak are analysed the background of inelastically scattered electrons have to be removed. Different shapes of background have been proposed [142]: the Shirley background, which in its iterative way uses the areas of the computed peaks to calculate the intensity of the inelastic electrons, or the Tougaard background, which is based on the assumption of the existence of an energy loss cross section which represents the probability of an electron undergoing inelastic scattering processes as a function of its kinetic energy. In this work Shirley background has been used.

Lineshape and Peak Fitting The shape of an experimental peak is considered to be a Voigt curve. The Voigt curve is defined as the convolution of a Gaussian curve and a lorentzian curve. The Lorentz component arises finite lifetime of the core hole, which in turns induces a spectral broadening. The Gaussian component is due to thermal broadening, and vibrational spectra. Also very important are all the experimental causes, as finite analyser resolution, band width of the impinging X-ray radiation (which is a lorentzian for anode discharge X-ray source but becomes a Gaussian in case of synchrotron radiation) and slits resolution. Unfortunately an analytic Voigt curve is not possible to calculate [45] and a linear combination of Lorentz and Gauss curve was used. The coefficients of the linear combination were adapted as a function of the FWHM (Full Width at Half-Maximum) to account for the constant width of the lorentzian contribution (i.e. a wider peak will have a larger Gaussian component but the same lorentzian component than a narrower one coming from the same element). The fitting have been carried out using the free software XPS peak. In certain cases asymmetric lineshape had to be used (for example to simulate the Doniach-Sunijch lineshape of metallic sample or other final state effects, or components that are too close to be resolved. This is dealt by the software XPS-Peak by setting a second Gaussian with centroid at higher BE respect to the principal one. Two parameters have to be set: the distance between the two centroids and the intensity ratio between the two Gaussian.

Thickness Determination It was evident from Equation 2.10 that the intensity of an XPS peak depends from the depth of the emitting atom, by the inelastic mean free path λ. In fact the addition of an overlayer of thickness t on top of the measured element causes an attenuation of a factor $exp - [t/\lambda]$. These results have been extensively used to measure the thickness of the deposited overlayer by measuring

the attenuation of the peaks from the substrate. In case no peaks coming from the substrate could be seen the thickness is thought to be greater than 3λ, as from basic statistics it is evident that 99% of the XPS intensity comes from a thickness of 3λ. λ for different materials have been found or on or calculated with the free software QUASES - IMFP calculation by TPP2M formula [137].

2.2.3 X-ray Absorption Spectroscopy

X-ray absorption is a powerful tool to study the unoccupied states of an element in a molecule [132]. It gives precise informations on the surroundings of the sampled element, and in particular its bonds in the molecule, and, to some extent, outside the molecule. In particular during this thesis we worked with Near Edge X-ray Absorption Spectroscopy Fine Structure (NEXAFS) spectroscopy, also called XANES (X-ray Absorption Near Edge Structure) Spectroscopy, which considers only the region around the ionization threshold (the ionization threshold is defined as the minimum energy necessary to excite an electron into the continuum, and is apparent as a strong step-like transition in the spectrum).
The absorption process can be described starting from the transition probability, which can be defined from the Fermi's Golden Rule:

$$P_{if} = \frac{2\pi}{\hbar}|\langle f|\mathbf{V}|i\rangle|^2\rho_f(E) \tag{2.12}$$

where $\rho_f(E)$ is the density of states of the final state (which becomes $\delta(E_f - E_i + \hbar\omega)$ when transition to a specific final state are taken into consideration instead that transitions to the continuum, i.e. photemission), $\mathbf{V} = \frac{e}{mc}\mathbf{A}\cdot\mathbf{p}$ with $\mathbf{A}$ is the exciting electric field (written in the Coulomb gauge), and $\mathbf{p} = \sum_i \mathbf{p}_i$ is the linear component of the momentum of all the electrons.
In the case of the electrical dipole approximation, the cross section can then be defined as:

$$\sigma = \frac{4\pi^2\hbar^2}{m^2}\frac{e^2}{\hbar c}\frac{1}{\hbar\omega}\sum_f |\langle f|\mathbf{e}\cdot\mathbf{r}|i\rangle|^2\delta(E_f - E_i - \hbar\omega) \tag{2.13}$$

where **e** is the unit vector of **A** and **r** is the position vector of the electron in the final state. It is possible to evaluate the matrix element in equation 2.13. If we assume to be considering a K-shell excitation (i.e. the initial state is a 1s state), the $|i\rangle$ is spherically symmetric and the final state $|f\rangle$ needs to possess at least one node, i.e. it must be a p orbital, or an hybridized orbital with some p component as the Hamiltonian is represented as a dipolar transition and the same selection rules apply as in optical spectroscopy, i.e. Δl= $\pm$1. Also the vector matrix element points in the same direction of the p-component in the final state orbital on the excited atom. It is there stated explicitly the dependence of the intensity of the signal from the mutual orientation of the light polarization (the versor **e**) and the orbital spatial conformation. This is particularly useful as, if linearly polarized light is used, it is possible to vary the angle between the incident beam and the sample to maximize the cross-section

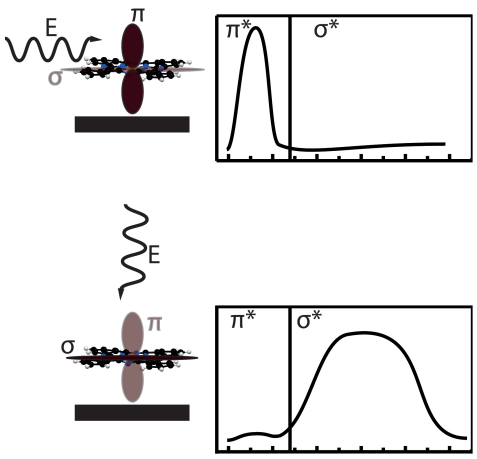

FIGURE 2.11: Effect of the polarization of the impinging electric field **E** on the spectrum of well-ordered samples, the so-called Search Light Effect. Note that the σ bonds are in fact formed by two hybridized sp^2 orbitals, and therefore possess a certain amount of s character that allows them to be sampled.

of resonances towards a specific orbital (π* or σ*) as shown in Figure 2.11. From organic chemistry and the LCAO theory it is known that σ bonds are directed between the atoms forming them, while π bonds are perpendicular to the bond direction, and keeping that in mind it is possible to sample the molecular orientation with respect to the beam. Also it has to be remembered that, as the dipole transforms as a vector or ungerade, and the initial state is totally symmetric (s state, gerade) the final state also has to transform as a vector (i.e. have x; y; z in its representation) for the integral to be $\neq 0$. It is important to note that the presence of the core hole can shift the final state orbitals, as well as modify the density of empty states.
Another interesting feature of the NEXAFS spectra is the possibility to correlate the position of the σ* resonances with the bond length [132]. At first it was predicted by means of theoretical calculations with the molecular orbital theory. It has then been demonstrated for different kinds of molecules (aromatic, aliphatic, adsorbed, chemisorbed and in gas phase, see ref. [132] and references therein) that an increase of the bond length leads to a shift of the σ* reference closer to the ionization potential.

Experimental details

Spectra acquisition To measure an absorption spectra different methods are applicable: electron yield and fluorescence yield. Also there is the possibility to measure the absorption directly, i.e. measure the intensity of the beam passing through the sample, but this technique requires very thin samples (again, X-ray penetration in matter varies from some μm to a few mm), and is not really surface sensitive. In this work we mostly used the electron yield, which is based on the photoemission

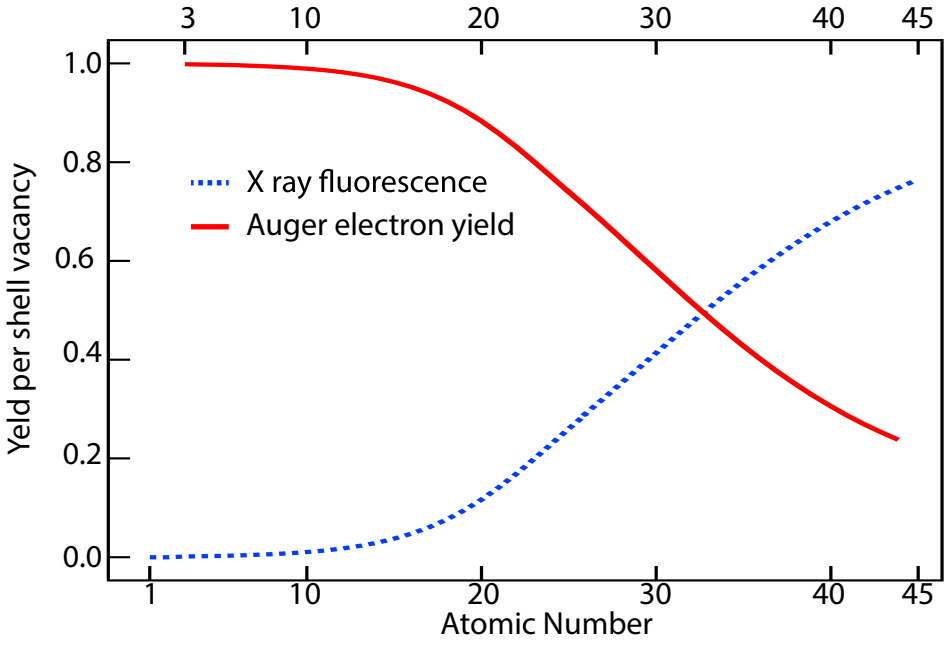

FIGURE 2.12: Cross section for the Auger and X-ray Fluorescence process for increasing values of the atomic number. Taken from ref. [73].

principle, which is the dominant process in the interaction between X-ray and matter at energy range below 2000 eV. Both measuring principles are based on a decay principle: when a photoelectron is emitted the highly energetic core hole is filled by a valence band electron either radiatively (X-ray fluorescence) or non radiatively (Auger). Figure 2.12 shows the variation of the cross section of the two processes for increasing Z, which shows why for atoms smaller than Ge the Auger process is favoured (i.e. will yield a better signal/noise ratio). Also the measure of photoelectron guarantees that high adsorbate sensitivity is achieved due to the low escape depth of low kinetic energy photoelectron (see. Figure 2.9). This can be further enhanced by applying a retarding voltage before the channeltron.

Spectra Calibration NEXAFS is strictly a synchrotron technique, as it requires variable photon energy. The problem is that photon energy might be different from the chosen one for many reasons: the monochromator is mechanically moved, and perfect reproducibility of this kind o movement is rarely achieved, phenomena of backlash or drift in the mechanical movement are frequently seen. Also beam misalignment might influence the λ of the outcoming photon. Therefore different procedures are put in place. The most common is to record an XPS spectrum of a peak (with a given photoelectron kinetic energy E_k), and then look again for the same peak at $E'_k = E_k + h\nu_{set}$. This exploits the fact that the second diffraction order is also passing through the slits of the monochromator, and therefore a peek at higher KE is found. Then it is simple to find the positions of the two peaks and the photon energy is given by $h\nu_{real} = E'_k - E_k$. Another way to calibrate the energy of the

spectra is based on the contamination on the beam optics. Every monochromator is covered by a thin layer of impurities, mostly C, N and O, which will yield a characteristic NEXAFS spectrum. This spectrum can be calibrated in energy very precisely by measuring them at the same time (in Partial Electron Yield, PEY, by electrically connecting the monochromator with a microamperometer) with a well-defined sample, for example gaseous CO for C and O and N_2 for N. Then it is possible to measure simultaneously the spectrum of the sample and the spectrum on the monochromator and calibrate the latter on the preceding reference to obtain the energy calibration on the needed spectrum. See Figure 2.13b). After calibration the spectrum has to be divided by an internal sample to remove the feature due to contamination on the beam optics, which give rise to an irradiation on the sample that varies with E_{ph} (see above). This can be done in different ways: if the absorption spectrum is taken on the toroidal mirror this is indeed a first step. Otherwise it has to be divided by the reference take on the clean substrate. This also ensures that absorption feature from the substrate does not alter the spectrum. Another possibility is to have a reference grid (usually gold plated) in front of the sample, and measure its absorption spectrum at the same time.

2.2.4 Surface Differential Reflectance Spectroscopy

Surface Differential Reflectance Spectroscopy (SDRS) is an optical spectroscopy technique which consists in measuring the variations of reflectivity of a sample, to obtain information on the variation of the dielectric constant at the surface for example after the deposition of an overlayer [51]. The measured signal is

$$\frac{\Delta R}{R} = \frac{R_0 - R}{R_0} \tag{2.14}$$

where R is the reflectance at a time t of the reaction, and R_0 at t=0. This signal can be measured almost continuously (the typical duration of a single spectrum is a couple of seconds) to follow in real time a process, as the only requirements to use this technique are two optical viewport in the right geometry (see Figure 2.14) because light is usually not interfering with most of the surface science process. To relate the signal to the optical properties of the film and the substrate, in the case of ultrathin films (film thickness d is $\ll \lambda$) the following equation can be employed [28]:

$$\frac{\Delta R}{R} \approx \frac{8\pi d}{\lambda}[A \times \epsilon^n_{film} + B \times (\epsilon'_{film} - 1)] \tag{2.15a}$$

$$A = \frac{1 - \epsilon'_{substrate}}{(1 - \epsilon_{substrate})^2 + (\epsilon''_{substrate})^2} \tag{2.15b}$$

$$B = \frac{\epsilon''_{substrate}}{(1 - \epsilon_{substrate})^2 + (\epsilon''_{substrate})^2} \tag{2.15c}$$

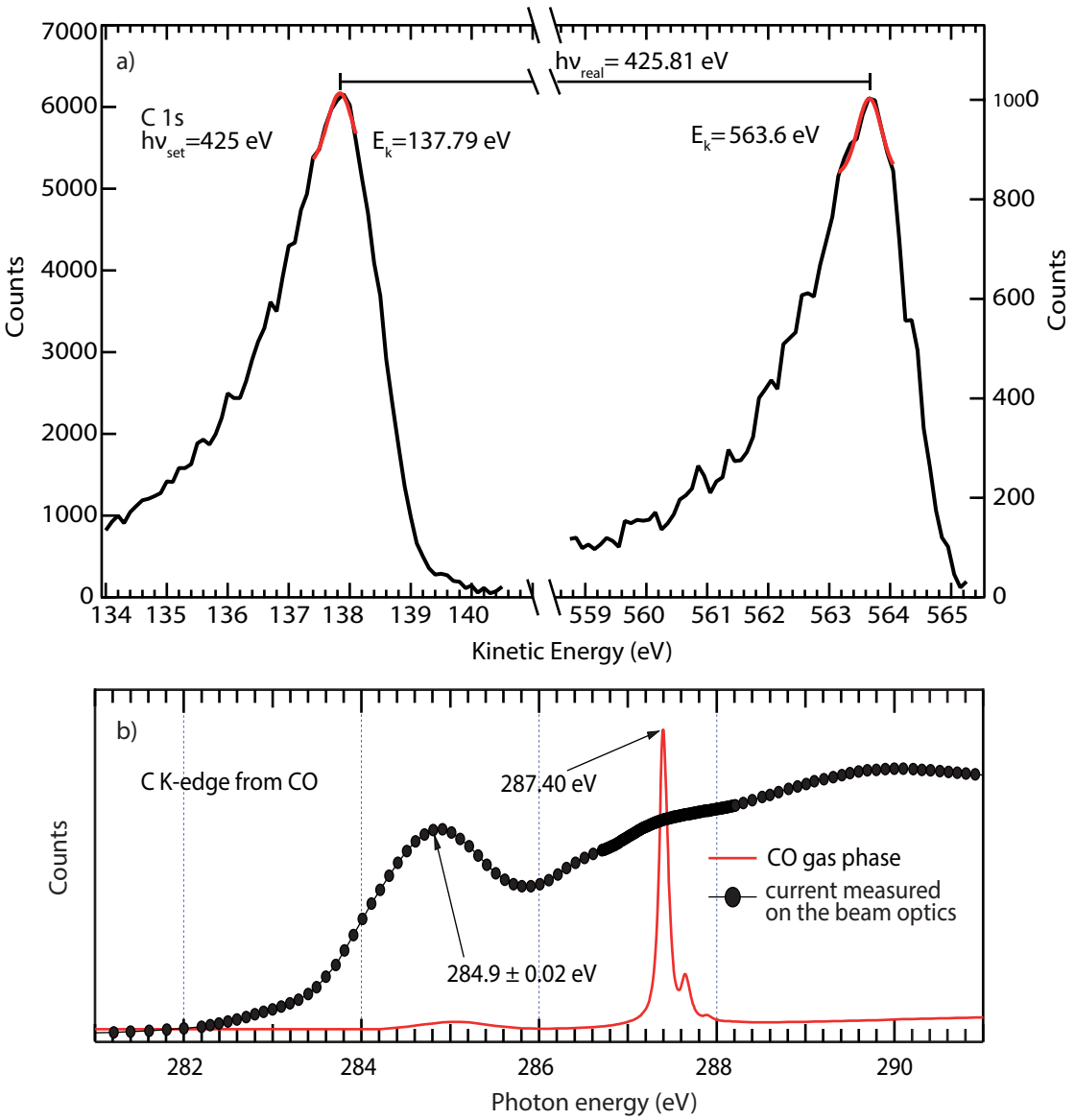

FIGURE 2.13: Two different methods for calibrating the photon energy in NEXAFS spectra: a) Carbon 1s spectrum measured using the first (left) and second (right) diffraction order of the monochromator. The peaks have been fitted with a Gaussian curve. b) internal standard using the impurities on the monochromator. Image b) courtesy of L. Floreano.

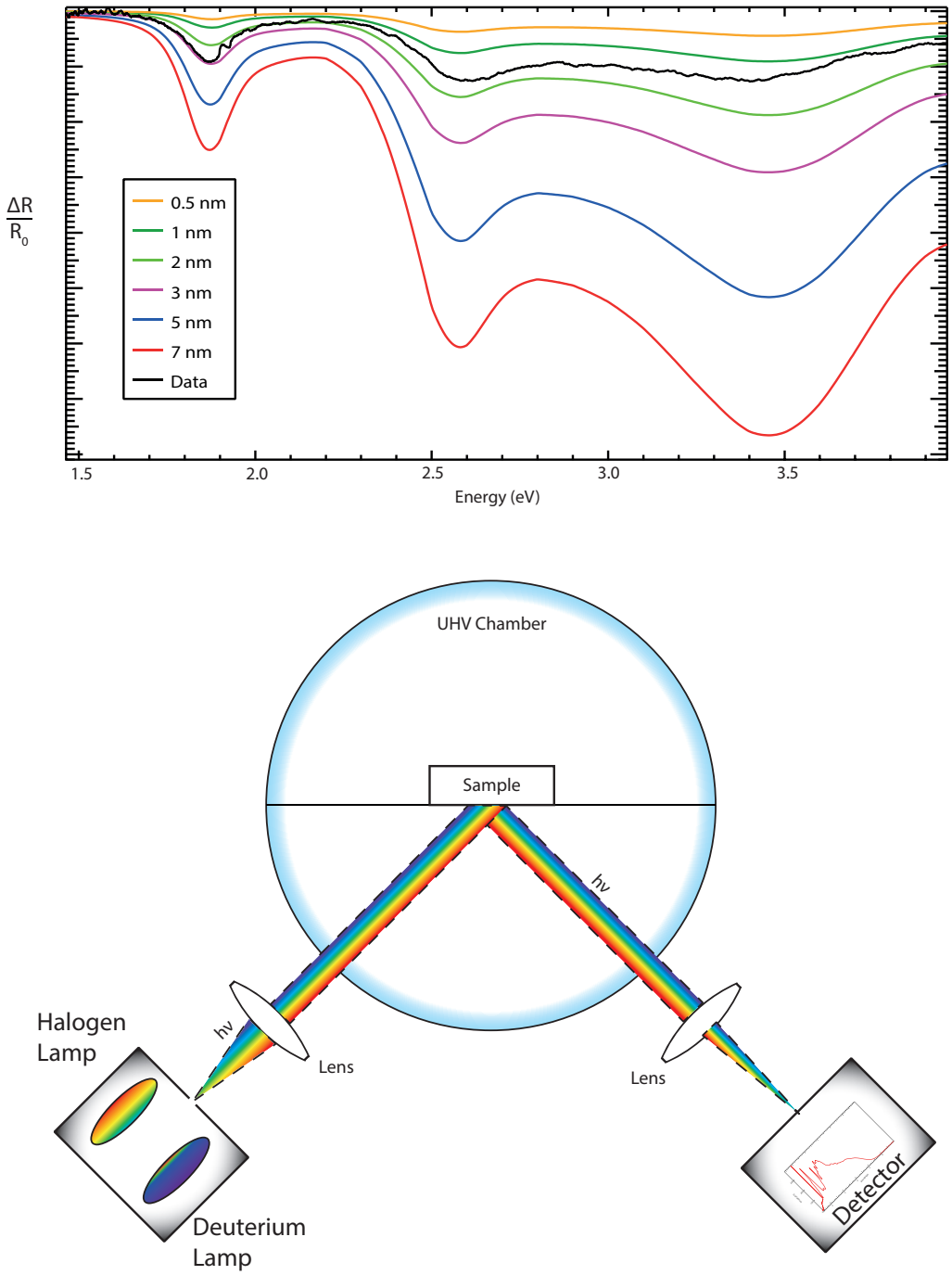

FIGURE 2.14: a) schema depicting the experimental setup used in this work; b) the calculated SDRS spectrum for $LuPc_2$ thin film deposited on gold, with the Data relative to a ∼2 nm thick film obtained experimentally.

where ϵ' and ϵ'' are the real and imaginary component of the dielectric constant (i.e. ϵ' - iϵ'')=n^2). From Equation 2.15 it is clear the dependence of the measured signal from the dielectric constant of the overlayer, this allows to know exactly which kind of adsorbates are present on the surface. In particular during this work we constantly verified the absence of H_2Pc in our samples, as the two have quite a different optical signature (see Figure 2.14). Also from Equation 2.15a it is possible to see the dependence on the thickness film d, which allowed us to simulate the optical signal for a range of thickness, and by comparison to obtain a reliable measure of the thickness of the film in real time. The geometry of the system is shown in Figure 2.14. Light is emitted by a halogen and a deuterium lamp, allowing a measuring range from 1.4 eV to 5.5 eV. It is then guided by an optical fibre to a lens to obtain a parallel beam which hits the sample at an angle θ. The beam is reflected to an angle θ (defined respect to the normal to the surface), and is reflected with the same angle. It then passes through a mirror that focalizes it on the detector, a S2000-TR (Ocean Optics). It is now possible to understand one of the drawbacks relative to this technique: it requires two viewport (possibly optical viewport, made out of quartz, with good transmission coefficients in the UV range) at the right angles, namely at the same angle respect to the normal to the sample surface. Otherwise the same technique can be done in normal conditions (i.e. light comes in and gets out from the same viewport, placed normal to the sample surface) with the aid of an optical fibre. Also, of course, a third flange has to be pointing to the sample in the same conditions to allow to evaporate the molecules on the sample.
Other possible drawbacks of this measurement are that the optical signature (i.e. the two parts of the dielectric constant) of the molecule has to be already known, usually measured by ellipsometry, the measurement being differential makes it really sensitive to changes in the illumination in the room (lights switched on and off, or even daylight from the windows changing angles). The experimentator has to be particularly careful while installing the setup, to have a perfectly stable installation, without vibrations on both the lenses and the optical fibres otherwise noise or drift problems can arise. The sample has to be as thermally stable as possible (possibly with thermal oscillation being kept below 0.1 °C) to ensure that no thermoreflectance effects perturb the measurement.

2.2.5 Scanning Tunnelling Microscopy

Scanning tunnelling microscopy (STM) was invented at the IBM laboratories of Zurich by Gerd Binning and Heinrich Rohrer in 1981, who were awarded with the Nobel prize in 1986 for this invention and its development. Since then STM has become a valuable technique to characterize the morphological as well as electronic properties of a surface. The probing system is constituted by a sharp tip (ideally monoatomic) which is brought at a few angstrom from the sample, a bias V is applied between the tip and the sample, and, due to the tunnel effect, a current will pass through the vacuum between the tip and the sample. As the tip is moved back and forth on

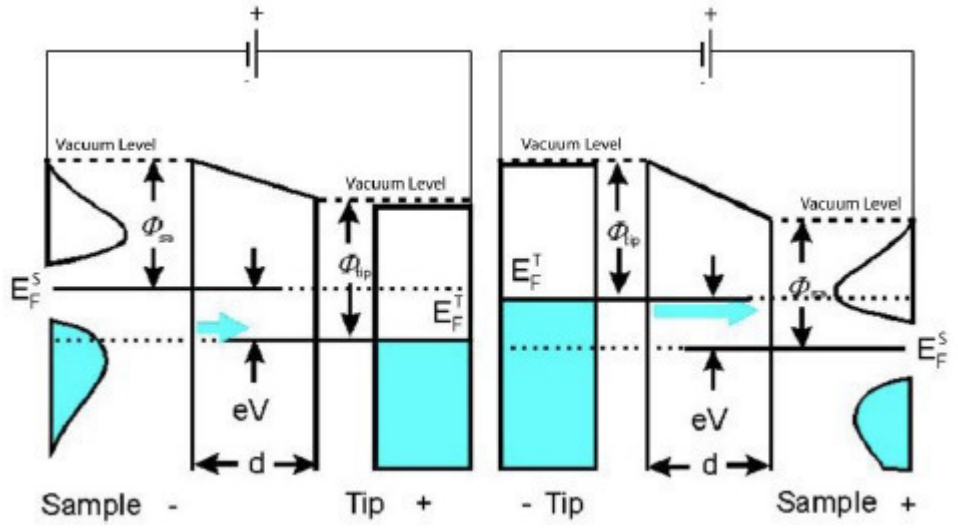

FIGURE 2.15: Changes in tip-sample system energy and tunnelling conditions as the bias polarity is inverted.

the sample's surface by a piezoelectric system, a map of the sample morphology is obtained. As mentioned the technique is based on the quantum tunnelling effect, discovered by Friedrich Hermann Hund in 1926. It describes the possibility that a quantum object of kinetic energy E_k is able to overcome a potential barrier of height V_0 ($V_0 > E_k$) if the barrier is thin enough. This is quite remarkable if confronted with its classical equivalence, which gives a transmission coefficient which is identically 0. This is due to the requisite of continuity for both the wave function and it is first derivative in every point of the space, which implies an exponential decrease of the wavefunction inside the barrier, so if the barrier is thin enough the wave function will not be 0 after the barrier. The tunnelling current can be written as

$$I = \frac{2\pi e}{\hbar} \sum_{\mu;\nu} [f(E_\mu) - f(E_\nu)] |M_{\mu;\nu}|^2 \delta(E_\mu + V - E_\nu) \tag{2.16}$$

where $|M_{\mu;\nu}|^2$ is the tunnel matrix element between the two electronic wavefunction ψ_{mu} and ψ_{nu} representing an electronic state in the sample and one in the tip respectively, f represent the Fermi distribution for an energy E_i, which can be approximated with the step function (i.e. the Fermi distribution at T=0K). Within the hypothesis above the equation can be evaluated as follows:

$$I = \frac{2\pi e}{\hbar} \sum_{\mu;\nu} |M_{\mu;\nu}|^2 \delta(E_\nu - E_f) \delta(E_\mu - E_f) \tag{2.17}$$

with $|M_{\mu;\nu}|^2 = \frac{\hbar^2}{2m} \int dS (\Psi_\mu \nabla \Psi^*_\nu - \Psi_\nu \nabla \Psi^*_\mu)$ As seen above the measured current is due to a combination of different factors: in the hypothesis of a positive bias applied to the tip there must be an empty electronic state on the tip, and an occupied state on the sample (for a reverse bias the occupation of the states must be reversed as well),

as shown in Figure 2.15. The presence of the applied bias V in the equation takes into account the fact that the electronic levels will be shifted after the application of the bias. This means that the tip is not sampling the actual morphology of the sample, but instead the Local Density of States (L-DOS) is being sampled. Therefore to resolve morphological from electronic effects and calculate the morphology of the surface DFT simulation (in principle of both the tip and the sample) are required.

Experimental details

Vibration Isolation The main problem of STM is due to the need for a very stable system. The z displacement of the tip must be controlled in the range of pm, needing a perfect insulation (z noise must be below 0.01 $\mathrm{angstrom}$, x and y below 0.1) from external vibrations.
Vibrations can come from a lot o different sources. Building vibrations are usually found at low frequency (between 5 and 100 Hz), and are their intensity increase the higher the floor, and the further from the supporting pillars. Then there is the line frequency (50 or 60 Hz), vibration induced by irregular events (door closing, people walking) and conveyed by the floor, and, of course, the vibration produced by moving parts (rotors in rotative and turbomolecular pumps).
To isolate from the low frequency vibrations an effective way is to suspend the whole system on compressed air legs. To isolate from medium frequencies it is possible either to mount the system on a set of materials with different elastic moduli, or to suspend the scanner on springs with eddy current damping. In particular the latter was implemented in the VT-omicron scanner that we used for the measurement presented in this work. The working principle is the following: the microscope is mounted on a copper support with palettes at the extremity; this support is suspended via springs in a magnetic field generated by a permanent magnet; when the support starts vibrating it behaves as a conductor moving in a magnetic field (i.e. experiencing a variable $\mathbf{B}(t)$), which generates parasitic currents in the conductor, which act to reduce $d\mathbf{B}/dt$, i.e. reducing the vibration amplitude. The high frequencies are usually cut off with electronic filters.

Tip Preparation It is crucial to achieve a good resolution in an STM experiment to have a sharp and stable tip. Tips are usually made of a Pt-Ir alloy (mostly used for Scanning Tunnelling Spectroscopy), or W. They can be either cut from a wire or electrochemically etched in a basic solution (usually KOH or NaOH at different concentration). Our tips were made by polycrystalline W wire usually 0.2mm thick. The electrochemical etching was by dipping the tip in a NaOH solution ≈ 2 M with a bias of around 10 V. When the lower part of the tip detaches the remaining part is suddenly removed from the solution and rinsed with ultrapure water. This step is crucial as the electrochemical etching will continue for several minutes after the voltage is removed, and this will result in a dull tip. After this procedure the tip is

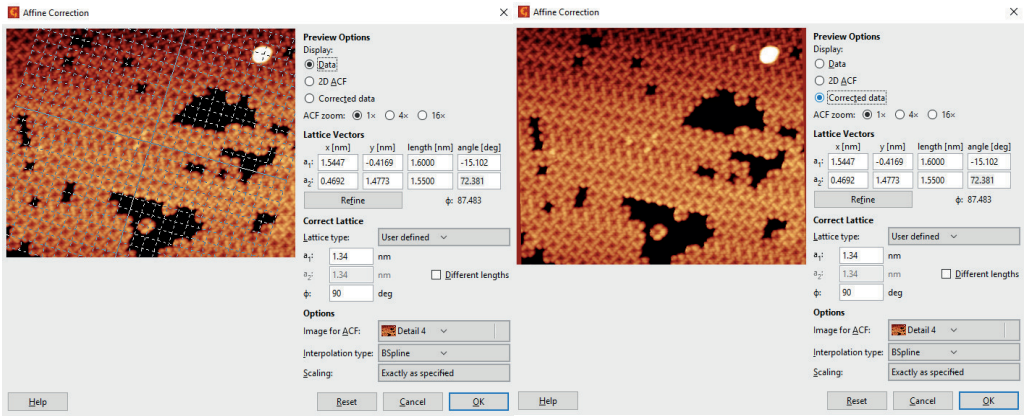

FIGURE 2.16: STM correction procedure: a)superposition of the measured lattice on the image; b)distortion of the original image to match the measured lattice.

inserted in the vacuum chamber, and heated by direct current to ≈ 200 °C overnight to outgass. It is then flashed 3 times at high temperature (until it starts emitting visible light) for 30 seconds (pressure below 10^{-9} mbar) to remove the native oxide layer. It is very important not to heat the tip to higher temperature or too long to avoid blunting effects.

Drift Correction To interpret correctly the STM images it is necessary to correct for distortion effects. These effects might be due to many different reasons: drift is often seen at the beginning of a scan or after a long movement (starting an image from the beginning), or due to temperature variations; piezoelectric motors can be miscalibrated, the system itself can possess a certain inertia that lead to a hysteresis cycle. To avoid all these artifacts the following procedure was put in place on the software Gwyddion [103] in all the images the measured lattice was confronted with the one measured with grazing incidence X-ray diffraction, see Figure 2.16.

2.2.6 X-ray Diffraction

Diffraction is a phenomenon observed when a wave impinges on a periodic structure which has a repeating structure of roughly the same size of the impinging wavelength λ. Interatomic distances are in the range of the $\mathrm{angstrom}$, which corresponds in the electromagnetic spectrum to photons having energies between 1 and 10 keV (soft X-rays).
When a highly energetic photon hits a solid different phenomena can occur: X-ray absorption has already been dealt with in sections 2.2.2 and 2.2.3, the alternative is represented by scattering, which might happen in the form of inelastic scattering (Compton), or elastic (Thomson). The latter is the one relevant for diffraction. In this case the electrons oscillate as Hertz dipoles (nuclei also oscillates, but due to the higher mass the contribution is negligible), becoming itself a source of X-rays.

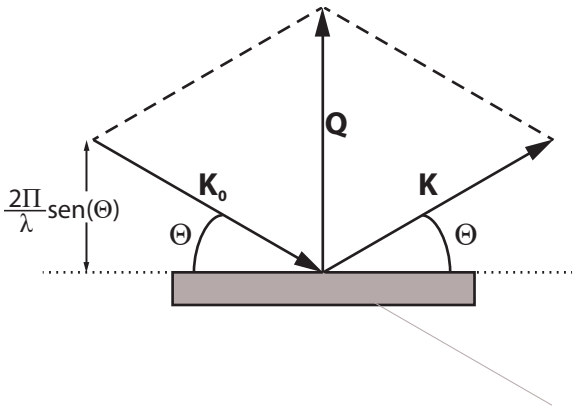

FIGURE 2.17: Geometry of the scattering vector construction.

The wavelength of the incident radiation is conserved as we are dealing with only elastic scattering. A phase shift of 180° occurs with the scattering, but as this shift takes places for every scattering centre it has no effects on the definitive interference pattern. According to the Thomson model the electric field at a distance **R** from the scattering centre (thought to be an atom) is described by the equation

$$\mathbf{E}(\mathbf{R}) = \mathbf{E}_0 \frac{1}{4\pi\epsilon_0 R} \frac{Ze^2}{mc^2} sin(\widehat{\mathbf{E}_0\mathbf{R}}) exp(-i\mathbf{K}\mathbf{R}) \tag{2.18}$$

where ϵ_0 is the vacuum dielectric constant and c is the speed o light, **E** il the electric field vector and Z is the atomic number (as all the electrons in the atom act each as a scattering centre). If we consider to shine a perfect infinite crystal, for simplicity a simple cubic of lattice vector $\mathbf{r}_{n_1 n_2 n_3}$ the intensity calculated at a point **R** will be (for $\mathbf{R} >> \mathbf{r}_{n_1 n_2 n_3}$, also called Fraunhofer condition)

$$I = \mathbf{E}_0 \frac{Zr_e}{R} C exp(-i\mathbf{K}\mathbf{R}) \sum_{n_1 n_2 n_3} exp\left(-i(\mathbf{K} - \mathbf{K_0})\mathbf{r_{n_1 n_2 n_3}}\right) \tag{2.19}$$

from Equation (2.19) it is apparent that the intensity is critically dependent from the spatial orientation of the K_0 and **K** with respect to the crystal lattice vectors. To explicit that the difference K_0 - **K** is also explicited as:

$$\mathbf{Q} = \mathbf{K} - \mathbf{K_0} \tag{2.20}$$

From both the graphics in 2.17 and equation (2.20) it is evident that **Q** depends both from the wavelength of the probing light and the geometry of the experiment (via θ). This implies that the magnitude and direction of the scattering vector are completely under the control of the experimentalist. Evaluating separately the three terms in eq. (2.19) leads to

$$\sum_{n_1=0}^{N_1-1} \sum_{n_2=0}^{N_2-1} \sum_{n_3=0}^{N_3-1} exp\left(-i\mathbf{Q}\left[n_1 a\mathbf{c_1} n_2 a\mathbf{c_2} n_3 a\mathbf{c_3}\right]\right) \tag{2.21}$$

then to evaluate the intensity the result has to be multiplied by its complex conjugate, which results in the interference function

$$\Im(\mathbf{Q}) = \frac{sin^2(N_1 a\mathbf{Qc_1}/2)}{sin^2(a\mathbf{Qc_1}/2)} \frac{sin^2(N_2 a\mathbf{Qc_2}/2)}{sin^2(a\mathbf{Qc_2}/2)} \frac{sin^2(N_3 a\mathbf{Qc_3}/2)}{sin^2(a\mathbf{Qc_3}/2)} \tag{2.22}$$

as the number of scattering centres is really big the three factors in eq. (2.22) have nonzero values only if the denominators are close to zero, i.e.

$$\Im(\mathbf{Q}) \to max \Leftrightarrow \begin{aligned} a\mathbf{Qc_1} &= 2\pi h \\ a\mathbf{Qc_2} &= 2\pi k \\ a\mathbf{Qc_3} &= 2\pi l \end{aligned} \tag{2.23}$$

Here h, k, l can range from $-\infty$ to $+\infty$ and have the same meaning of the diffraction orders. The three equations (2.23) are the three Laue equations in the specific case of a cubic lattice. This set of equation allow to reconstruct the relation between the scattering vector $\mathbf{Q}$ and the lattice vector $\mathbf{r_{n_1 n_2 n_3}}$ in condition of constructive interference. Equations (2.23) represent in fact a system of three equations, that have to be all fulfilled to appreciable intensity. This leads to the vectorial equation

$$I(\mathbf{R}) \leftarrow max \Leftrightarrow \frac{|\mathbf{Q}|}{2\pi} = \frac{\sqrt{h^2+k^2+l^2}}{a} \tag{2.24}$$

which, remembering that $|Q| = 4\pi sin(\theta)/\lambda$ (see Figure 2.17) and assuming we are dealing with a cubic lattice can be rewritten as

$$I(\mathbf{R}) \leftarrow max \Leftrightarrow 2\frac{a}{\sqrt{h^2+k^2+l^2}} sin(\theta) = \lambda \tag{2.25}$$

where $\frac{a}{\sqrt{h^2+k^2+l^2}}$ is the geometrical distance between the planes perpendicular to the scattering vector d_hkl, which substituted in Equation (2.25) gives the well-known Bragg equation

$$2d_{hkl} sin(\theta_B) = \lambda \tag{2.26}$$

Different Experimental Setup There are multiple possible experiments that involve X-ray diffraction, in many different geometries:

θ /2θ Scan Is the most used method, usually to measure Bragg reflection from a sample. In this case the sample is shined with X-rays with a well-determined incident angle (θ), and a detector is placed at the reflection angle θ (see Figure 2.18 for clarification on the term). Then the sample is rotated to modify the angle with the impinging beam, while the detector is also rotated (at twice the angular speed) to remain in the reflection condition. In this way the scattering vector $\mathbf{Q}$ remains perpendicular to the sample surface, and the only thing that vary is its absolute value. This way the interplanar distance of the planes parallels to the surface of the sample

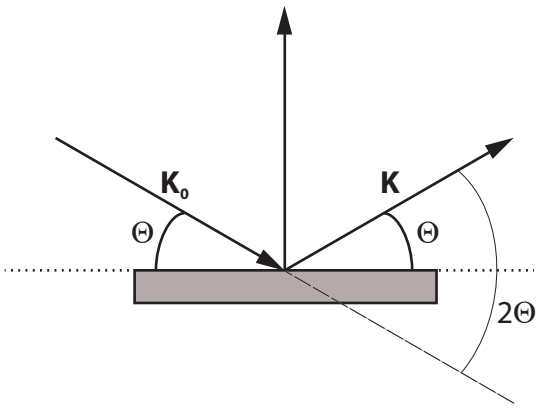

FIGURE 2.18: Schematic representation of a $\theta/2\theta$ experimental setup.

is measured. It is particularly useful with polycrystalline sample because of the presence of multiple planes families with the correct orientation. The rocking curve data were collected with a Siemens D501 equipped with a Cu kα X-ray tube (λ=2.29Å, see Figure 2.19 a)).

Pole Figures In normal rocking curves only the planes that are parallel to the surface are sampled. This implies that only a subset of the grains are sampled, the ones with the one with a preferential orientation of the planes parallel to the sample surface. A variation of the $\theta/2\theta$ scan is the pole figure scan [117]. A single pole figure scans the orientation of the scattering vector in the reciprocal space. This is performed by rotating the sample around the tilt angle ψ (which implies that this is a non coplanar configuration) and the azimuthal angle ϕ angles (see Figure 2.20). This is allowed thanks to the experimental setup (sample is placed in also called Euler-cradle having four angular degrees of freedom) which allows the rotation of the sample around the surface normal (ϕ angle) and the tilting around the rotation axis (ψ angle), while the 2θ angle is kept constant. Usually pole figures are presented in different geometries due to the different way to project a sphere on a flat surface. In this work the constant $\Delta\psi$ is used. The technique is currently used also coupled with synchrotron radiation to accurately determine the faceting of organic thin films [29].
The pole figures are collected with a Philips X'Pert system, with an ATC3 texture cradle mounted in a Bragg-Brentano focusing geometry. The Cr kα X-ray tube was collimated with two perpendicular 1° slits before the sample, and one 1° slit after the sample. This leads to an acceptance angle slightly larger than 1° $\Delta 2\ \theta$. Also a $\theta/2\theta$ scan was performed on the sample to test the positioning and also because the instrument geometry allowed to perform different scans at different Φ angles.
This technique, coupled with $\theta\ /2\theta$ scans, were performed at Technische Universitat Graz in the lab of Prof. Resel to obtain preliminary results on the self-organization of $LuPc_2$ thin film on different substrates, see Fig.2.19 b).

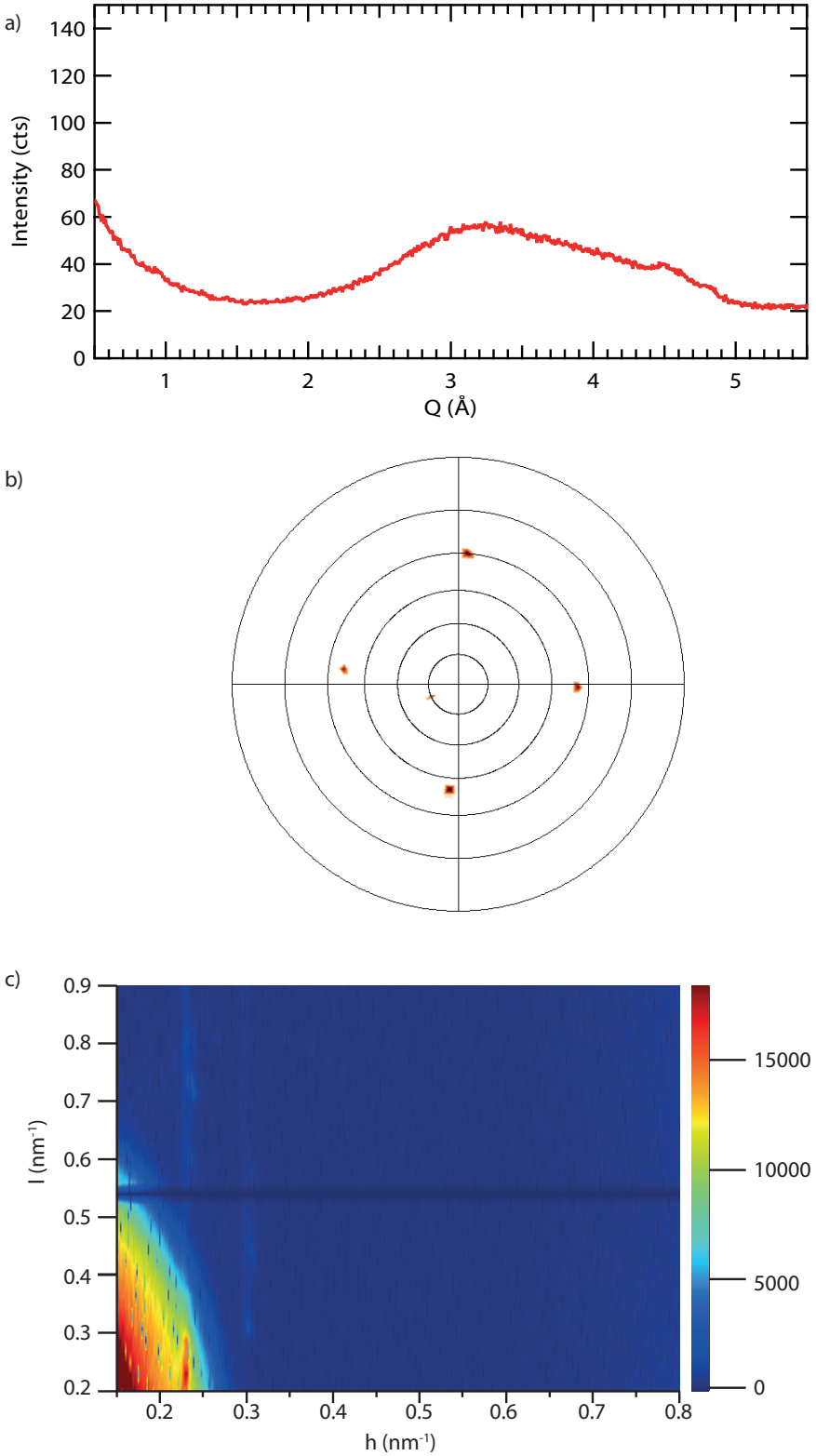

FIGURE 2.19: Example of the different X-ray diffraction techniques used in this work: a) $\theta/2\theta$ scan of $LuPc_2$ on H terminated Si(100); b)pole figure on the Si(111) peaks of $LuPc_2$ on H terminated Si(100); c)out of plane map of $LuPc_2$ over Au(111).

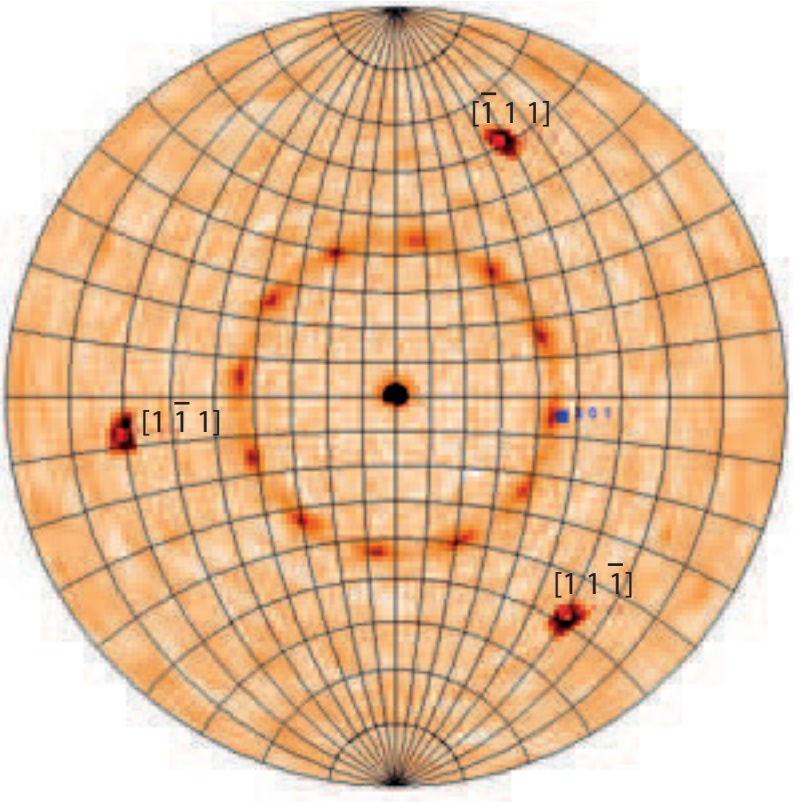

FIGURE 2.20: Schematic of a pole figure measurement.

Grazing Incidence Grazing incidence X-ray Diffraction (GIXD) is a powerful tool to study the structural properties of thin and ultrathin films. The penetration depth of X-rays in solids is in the 10-100µm range, while the thickness of films relevant for scientific or technical purposes can be below 1 nm. This directly leads to the fact that the peaks of the layers are buried in the noise coming from the substrate at typical Bragg angles. To increase the travelling path of the X-ray in the film the incident beam's entrance angle can be lowered down to a few tenths of a degree. The geometry is shown in Figure 2.21. In this case the impinging angle is different from half the diffraction angle, and it is kept constant during measurement, while the detector is either moved along the exit angle (2θ-α) or along the Φ angle. This directly implies that the scattering vector is not kept perpendicular to the surface, and hence planes of different orientation can be sampled (see Fig.2.21. A few very important factors have to be taken into account when lowering the angle: first the refractive index of many materials for x-rays is lower than unity. This leads to a total reflection below the critical angle (between 0.6 and 0.1° for most materials). In particular the Φ scan is currently employed to resolve the inplane structure and epitaxial relation between ultrathin films and the substrate in both inorganic [33] and organic materials [77].
This technique has been used at the beamline SIXS at the synchrotron SOLEIL to study the organization of $LuPc_2$ thin films on Au(111), see Fig.2.19 c).

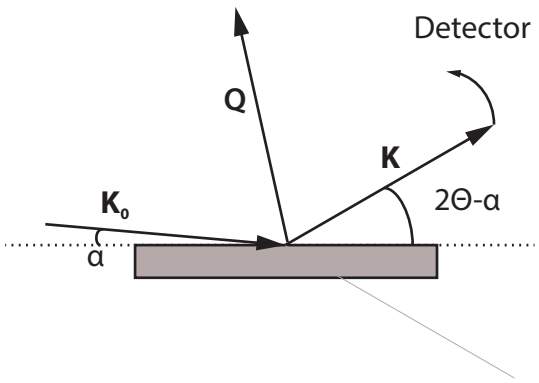

FIGURE 2.21: Schematic depiction of GIXD geometry.

Chapter 3

Results: Structure

In this chapter we present the results we obtained on the structure and the surface morphology of $LuPc_2$ thin films. The results have been acquired by means of different diffraction techniques (XRD, GIXD) as well as XRR and spatially resolved microscopic technique (STM).

3.1 Structure

The first part will present the structure sampled with integral techniques, in particular we used both synchrotron and lab based diffraction techniques to explore the structure of $LuPc_2$ on different substrates.

3.1.1 Structure of Rare Earth Pc_2

Phthalocyanines show a strong polymorphism, they are known to crystallize in different structures which are shown in Figure 3.1. The α structure is a metastable structure found in phthalocyanine thin films [152]. It is a tetragonal structure, with a square base defined by the **a** and **b** vectors and the **c** axis perpendicular to it. The molecular planes are parallel to the basis of the unit cell. Stacked molecules are in staggered position, meaning that the molecular axis (i.e. the axis joining two opposite benzene groups and passing through the central metal cation) are rotated by different angles respect to the c axis. This helps in reducing the electronic repulsion between the benzene rings. The structure was only fully resolved for single decker phthalocyanine, and in figure is represented for LiPc. The β structure is a monoclinic structure with a square basis. The distortion from the tetragonal is due to the offset in the packing. This greatly reduces the electronic repulsion between the benzene groups, that are found to be oriented all in the same direction which would lead to a strong overlap in case of a vertical stacking. This structure is an example of staggered π stacking, which allows for the superposition of the positively charged sides (in the quadrupolar approximation, which is in particular true for the benzene rings) of one molecule with the face of the next neighbour, where the electronic density is localized due to the presence of the delocalized molecular orbitals. The molecular plane is slightly inclined respect to the unit cell side, $\sim 8^\circ$. If the unit cell is tilted so to have the molecular plane parallel to the substrate surface, a perfect square is again

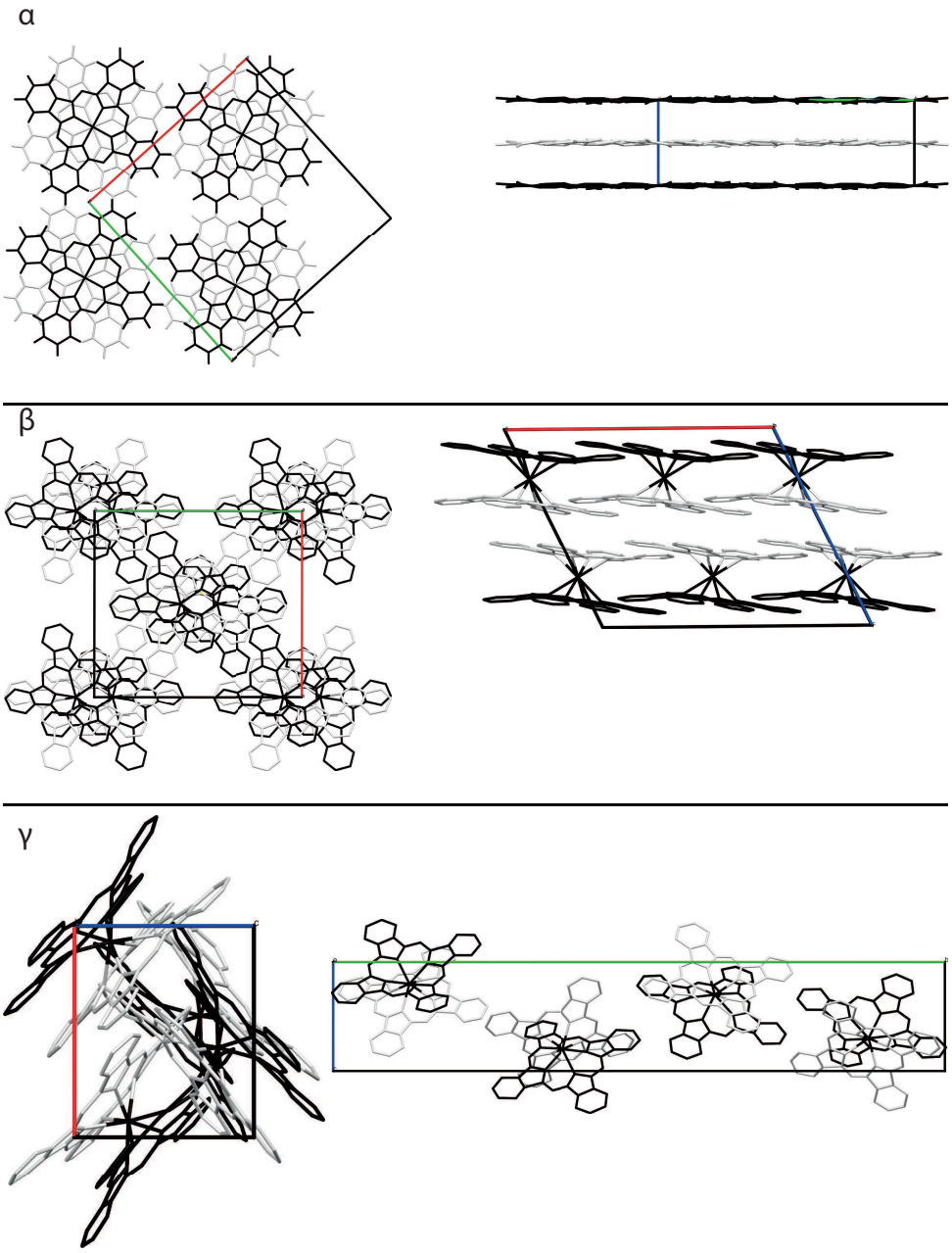

FIGURE 3.1: top: α phase from CuPc as taken from ref. [133], the molecules belonging to the lower planes are coloured in lighter colour; centre: the β structure from $NdPc_2$ taken from ref. [34]; bottom: the γ structure from $LuPc_2$ taken from ref. [98]. The atoms belonging to the lower plateau of double-decker phthalocyanine and the second plane in the structure of single decker phthalocyanine are coloured in lighter colours for clarity.

obtained. The γ structure is a herringbone-like packing with the molecules stacked almost perpendicular to their next neighbour to maximize the attractive electrostatic interaction between the benzene rings (again starting from the quadrupolar approximation). The molecules have their benzene units pointing towards the centre of the next molecule, leading to the zig-zag pattern. Only the γ structure has been fully resolved for $LuPc_2$ [98], as it is the most stable structure in single crystal or in powder. The β structure has been analysed for other $REPc_2$, and here the results for $NdPc_2$ are used. The two complex differ only in the central cation, and the two cations differ only in the atomic number (Lu being 71, and Nd being 60). This implies that while the Lu has a full $4f$ shell, Nd only has 4 electrons, but as the 4f shell is compact and close to the nucleus the difference in atomic radius is only 10% (the Nd(III) being 124.9 pm in the octahedral coordination, while the Lu(III) is 111.7 pm in the same coordination [69]) no major changes are expected in the structure. For the α phase of $REPc_2$ no data have been found in the Cambridge Data Structure Database. Consequently here the version for the single decker phthalocyanine (CuPc) is presented only to explain the stacking.

3.1.2 $LuPc_2$ on H terminated Si(100)

The first result was obtained on a low reacting surface, to study the properties of the molecule in a weakly bound state. H terminated silicon is indeed known to be a low reacting surface. The dimers of the 2x1 reconstruction of the Si(100) are saturated by H atoms, which act as a passivating layer [11]. This way the chemical bonding between the substrate and the molecule [9] is prevented. It has been shown [12] that the molecules are able to freely move on the surface and organize following only molecule-molecule interaction as a driving force. Therefore the packing should be different from to the one observed on metals. To further investigate this hypothesis and complete the NEXAFS data published by Bidermane and coworkers [10] XRD measurement have been performed on a $LuPc_2$ thin film deposited on H terminated Si(100). Our Si[100] sample in particular was presented with a miscut of 4° along the [110] direction, resulting in a stepped vicinal surface, with an average terrace size of a few nm.

The nominal thickness (as measured by SDRS) was $\sim$ 20 nm. However from the reflectivity scan shown in Figure 3.2 bottom and the Kiessig fringes we were able to remeasure the thickness to be 36$\pm$ 2 nm. Due to the inherent difficulty in accurately calculating the thickness from SDRS data, the thickness calculated from XRR data is retained. The sample shows a wide peak at $\mathbf{q}$=0.93 $Å^{-1}$, relative to the (040) plane of the γ structure of $LuPc_2$. The width of the peak is due to a certain amount of amorphous phase. As said before the γ phase is the stable phase in the single crystal, and it is not surprising to find it for thin films grown on slightly interacting surfaces. However the expected value for the (040) plane of γ structure is at 0.98 $Å^{-1}$, showing a relaxation in the out of plane direction. This might be due to the

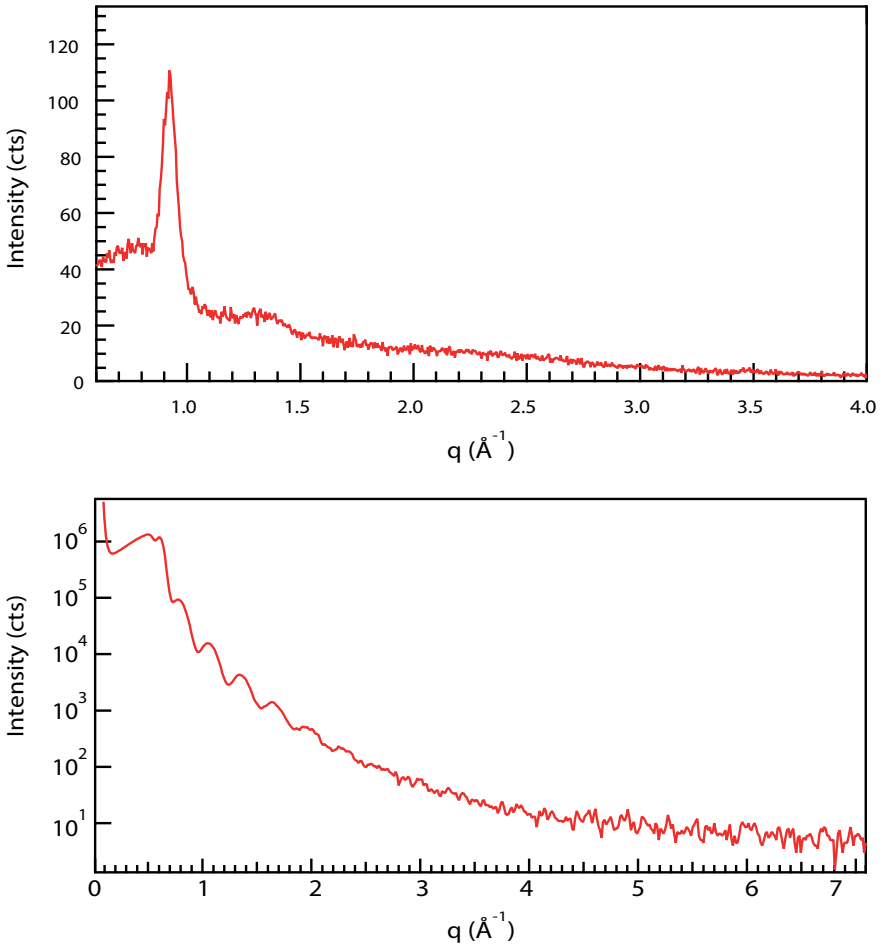

FIGURE 3.2: Specular scan (top) and reflectivity scan (bottom) of $LuPc_2$ deposited on H terminated Si(100).

morphological constraints imposed by the small terraces of the sample, which constrain the in-plane unit cell, causing a relaxation in the out of plane direction. The

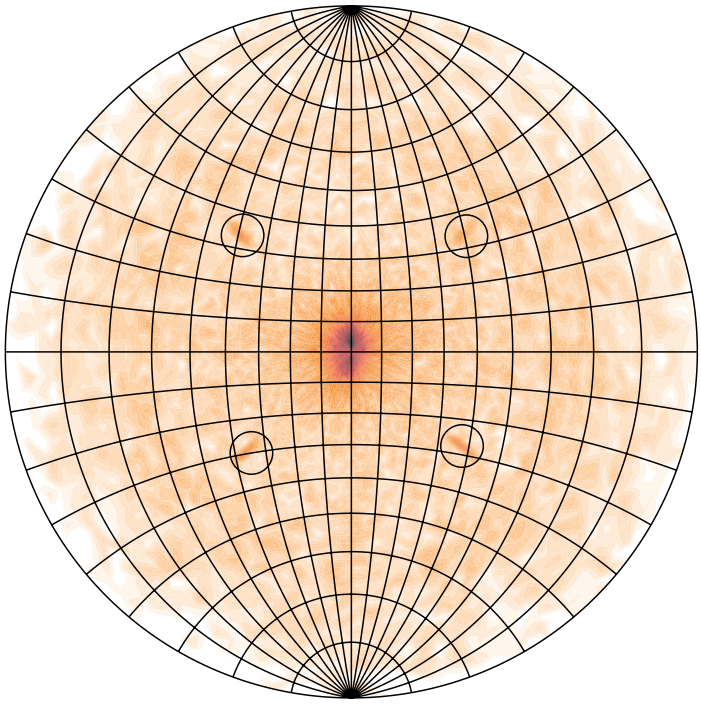

FIGURE 3.3: Pole figure around the (040) peak of $LuPc_2$ on H terminated Si(100).

pole figure taken on the (040) plane (Figure 3.3) shows a homogeneous distribution around the central spot (plus the 4 spots due to the (111) planes of Si, indicated by black circles, whose asymmetry is due to the miscut of the sample and to imperfection in the sample fixing on the goniometer), showing no variation in the direction of the unit cell axis. This can be explained with the template effect of the surface, which only gives a nucleation place for the crystal, but does not influence the crystal growth any further.

We can resume the results obtained on H passivated Si(100) by saying that the molecules absorb on the surface in a semicrystalline film, the crystalline moiety adopts the γ structure, which is known to be the stable phase in the single crystal, as depicted in Figure 3.4.

3.1.3 $LuPc_2$ on Au(111)

The structure of thin films of $LuPc_2$ deposited on Au(111) was analysed by means of different X-ray diffraction techniques: rocking curves, pole figures and GIXD. The first two techniques were employed with conventional X-ray sources in the group of Prof. Roland Resel at the Institute of Solid State Physics at the TU Graz, while the GIXD experiment has been performed at the beamline SIXS at the synchrotron SOLEIL.

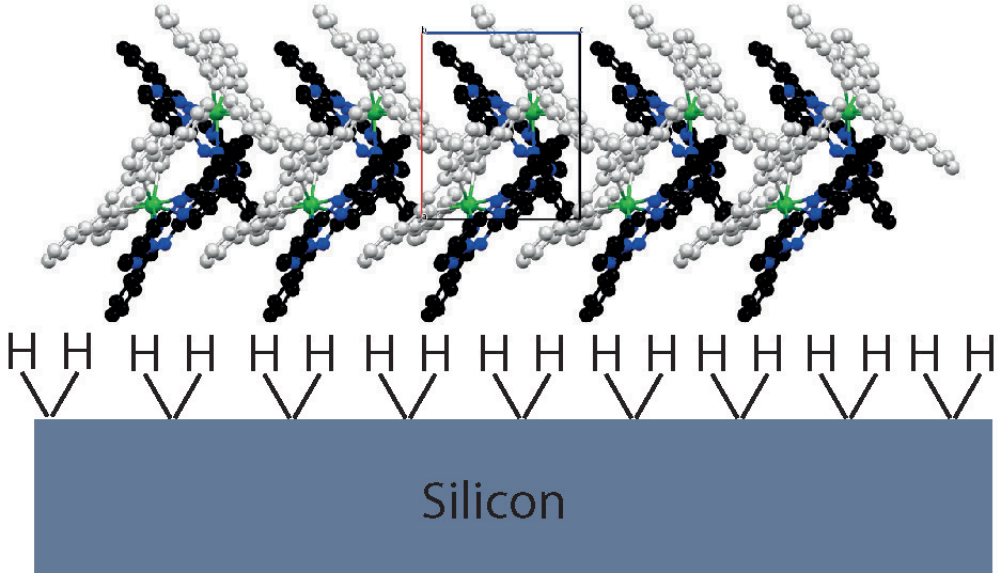

FIGURE 3.4: Depiction of the molecular stacking of $LuPc_2$ on H terminated Si(100).

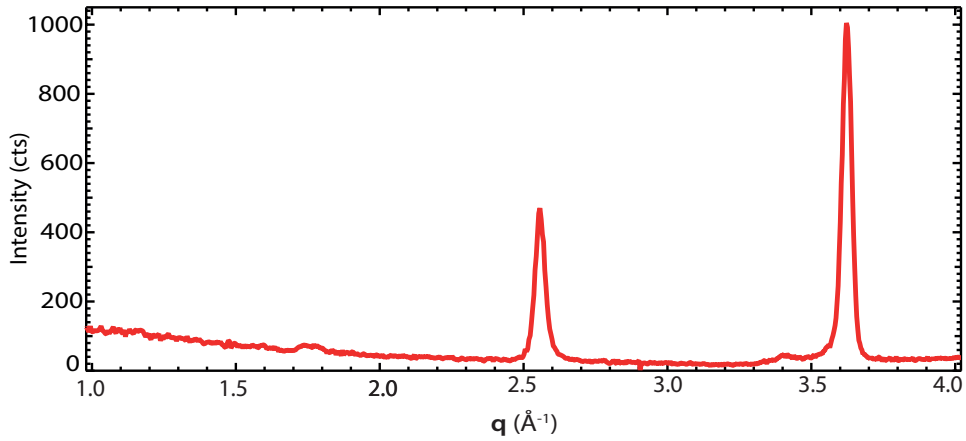

FIGURE 3.5: $\theta/2\theta$ scan on a 200 nm thick $LuPc_2$ thin film on Au(111).

Laboratory results The sample analysed using laboratory techniques was prepared by thermal evaporation of the molecules in UHV on a freshly cleaned, herringbone reconstructed, Au(111) single crystal. The thickness was estimated to 200 nm by means of SDRS. The sample was then removed from the vacuum chamber, transferred to the X-ray lab in Graz, where it was analysed after a few days. Specular scans were taken and are shown in Figure 3.5. The strong peak at **q**=2.53 $Å^{-1}$ is due to the Au(111) substrate. The two shallow peaks at **q**=1.75 $Å^{-1}$ and **q**=3.40 $Å^{-1}$ are due to the (002) and (004) planes of the β phase respectively. The two peaks are expected at 1.46 and 2.83 $Å^{-1}$ respectively. The discrepancy is most probably caused by an expansion of the interplanar distance in the out of plane direction. The strong peak at **q**=3.61 $Å^{-1}$ is due to the (002) plane of the α phase, which is expected at **q**=3.52 $Å^{-1}$. This is representative of a slight contraction along the c axis which might be caused by a relaxation of the in-plane structure due to the interaction with

the substrate or to a simple difference in the planar stacking of $LuPc_2$ respect to $NdPc_2$, as small differences are found [98]. The shrinking of the in-plane unit cell of the β structure and the expansion of the unit cell of the α phase are both most likely due to the influence of the substrate. It has to be noted, respect to the film deposited on H terminated Si(100) (see Figure 3.2), the absence of the large peak due to the amorphous phase. This is due to the higher crystallinity of the film. This is important, as it shows that the stabilization of the α and β structures due to the substrate does not fades far from the interface. We can conclude that the film is a mixture of the two phases (roughly 10% β) but, as both the α and the β phase have the c axis almost perpendicular to the molecular plane (see Figure 3.1) all the molecules are lying almost flat on the surface. The α phase is known to be the most stable phase in phthalocyanine thin films when the molecules are deposited under vacuum on a substrate kept at room temperature. Transition between the two phases is achieved after annealing, as was shown by Yim and coworkers[152].

To verify the presence of different domains pole figures were taken on the same

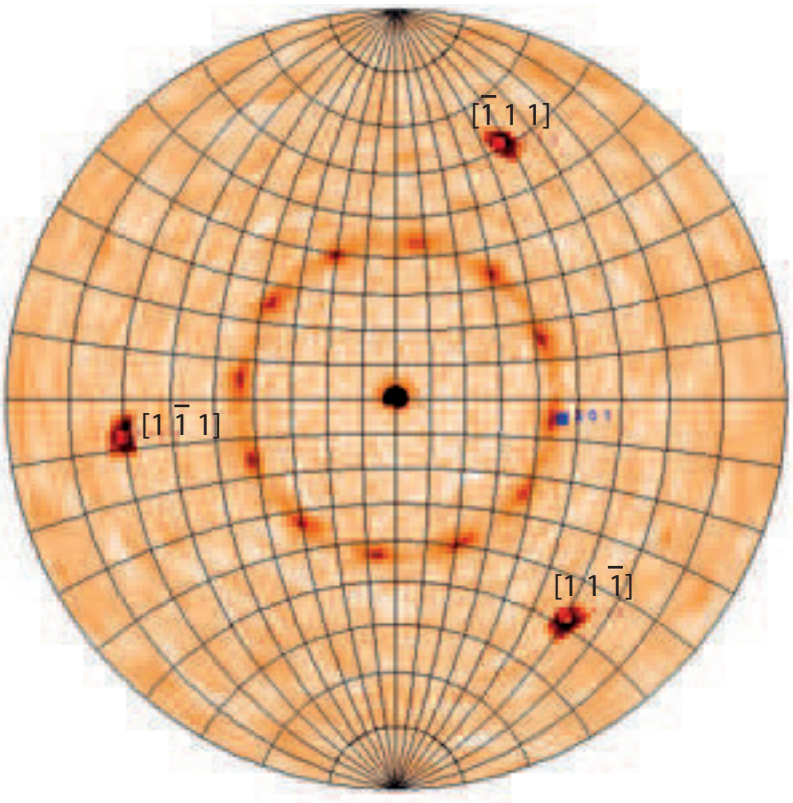

FIGURE 3.6: Pole figure of $LuPc_2$/Au(111) taken at **q**=3.61 Å^{-1}.

sample. The results are shown in Figure 3.6 which represents the pole figure taken around the (002) peak of the α structure. The central spot is the specular reflection of the surface, than the 12 spots around it are due to the epitaxial order of the $LuPc_2$ film, and last the three triangular spots are due to the tree $(1\bar{1}1)$ reflections of gold. The presence of 12 evenly spaced spots at an angular distance of 30° means that 12 different domains are present. Due to the six-fold symmetry of the substrate we can

reduce the 12 domains to only 2 symmetry inequivalent domains. The angle respect to the sample normal indicates that the molecules are not perfectly parallel to the surface but inclined by an angle of 4°.
The first conclusion that we can withdraw is that the molecules arrange on a mixture of α and β structure, instead than in the γ structure which is the most stable for the single crystal. This is due to the stabilization effect of the substrate. Also the film is composed by at least 2 different domains with different orientation respect to the substrate

synchrotron. To acquire further information on the system a GIXD experiment with synchrotron radiation was set up. The additional value of performing an experiment on the SIXS diffraction beamline at the synchrotron SOLEIL are at least threefold. First of all, the better resolution allowed by the synchrotron light will allow to better resolve the different domains. Second the SIXS beamline allows the sample to be prepared in situ, with cleaning facilities in the preparation chamber and deposition in the diffraction chamber (the Berillium Chamber). Third performing GIXD allows to have a stronger ratio between the signal of the overlayer and that from the substrate due to the longer path in the overlayer, and therefore allows the study of thin and ultrathin layers. The photon energy was set at 11 keV, equal to a λ of 1.12714 Å. The sample was prepared in situ in Berillium Chamber after a repeated sputtering and annealing cycles of the Au(111) substrate in the preparation chamber. The deposition was effectuated by thermal evaporation at 340° C and followed in real time by SDRS. The film was subsequently annealed at 300° for 15 minutes to increase long-range order.

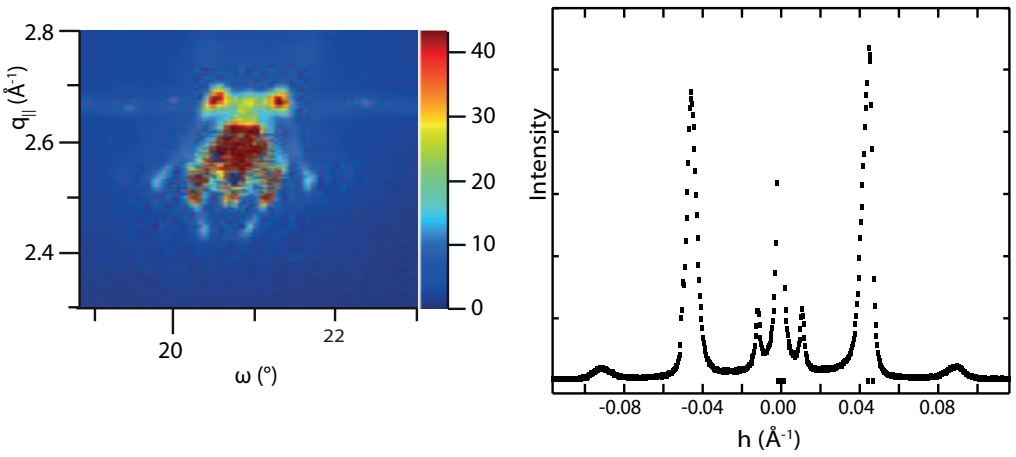

FIGURE 3.7: Inplane mesh (l=0.05) of the $(1\bar{1}0)$ peaks of the clean Au(111) substrate (left) and cut along one of the diagonal of the reciprocal space comprehending the herringbone reconstruction (right). The cut has been projected on the **h** vector of the reciprocal lattice for ease of representation.

Substrate First the gold substrate was investigated, and the results are shown in Figure 3.7. The large spot in the middle of the in-plane mesh in Figure 3.7 left is due to the $[1\bar{1}1]$ peak, surrounded by a hexagon of smaller spots due to the herringbone reconstruction. Note that the deformation is due to the measuring geometry. The hexagon distortion is probably due to the instrument geometry. It is worth noting that the spots are not localized on the direction from the main spot to the centre of the image. This is the $[1\bar{1}0]$ direction, while the reconstruction is perpendicular to it along the $[11\bar{2}]$. The shallow horizontal line at $\mathbf{q}_{||}$=2.68 Å^{-1} is due to a slight polycristallinity of the sample, probably close to the edges. In Figure 3.7 (right) a cut along the diagonal is shown, to better evidence the herringbone reconstruction. The absence of the principal peak at $\mathbf{h}$=0 Å^{-1} is due to the attenuation shutters on the beamline. During the measurement, if the number of photon on the detector exceeds a certain limit, a blade interpose between the sample and the detector, reducing the number of counts. Unfortunately the attenuation factors of the blade are unknown as well as the exact intensity when the shutter is moved and therefore the "real" data cannot be recreated. The Au(111) surface is well known to reconstruct at room temperature (it is in fact the only transition metal with a (111) face reconstructed at room temperature) since 1981 [141]. Since then a great debate has sparked about the size of the unit cell and the nature of the reconstruction, which was settled in 1990 when Barth and coworkers [5] with a joint LEED and STM investigation were able to describe the herringbone pattern on the surface and to measure the reconstruction's unit cell to be rectangular unit cell by means of LEED and STM investigation. They assigned it to a progressive transition from the hcp to the fcc domains, which have very similar energy. This transition is not abrupt but happens on a series of unit cell, and leads the atom in between the two domains to occupy position that are displaced from the highly coordinated fcc and hcp ones, and slightly more on top of the underlying atoms. These two factors generate a displacement in the z direction, which induces the contrast seen in the STM images, and which form the herringbone like pattern, with ridges perpendiculars to one of the close-packed directions. Along this direction atoms experience a contraction of around 5%. The ridges separate the hcp and fcc domains, with the fcc being almost 80% wider than the hcp, resulting in an apparent coupling of the ridges themselves [146]. The cause of this displacement is in the electronic repulsion due to the excessive number of electrons in the Au Wigner-Seitz unit cell, as was explained by Heine and Marks [62]. They showed that the full d band gives rise to an electrostatic repulsion that pushes the atoms out of their most symmetric position.

Film As deposited the molecules self-organize on the surface as demonstrated by the presence of a peak at $\mathbf{q}$=1.92 Å^{-1}, as shown in Figure 3.8, which is assigned to the (200) plane of the β structure. Using Bragg equation it is possible to calculate the interplanar distance to 14.5±0.1 Å. This is in good agreement with the literature results for the β structure, reported to 15.5 Å for $NdPc_2$. The width of the peak can

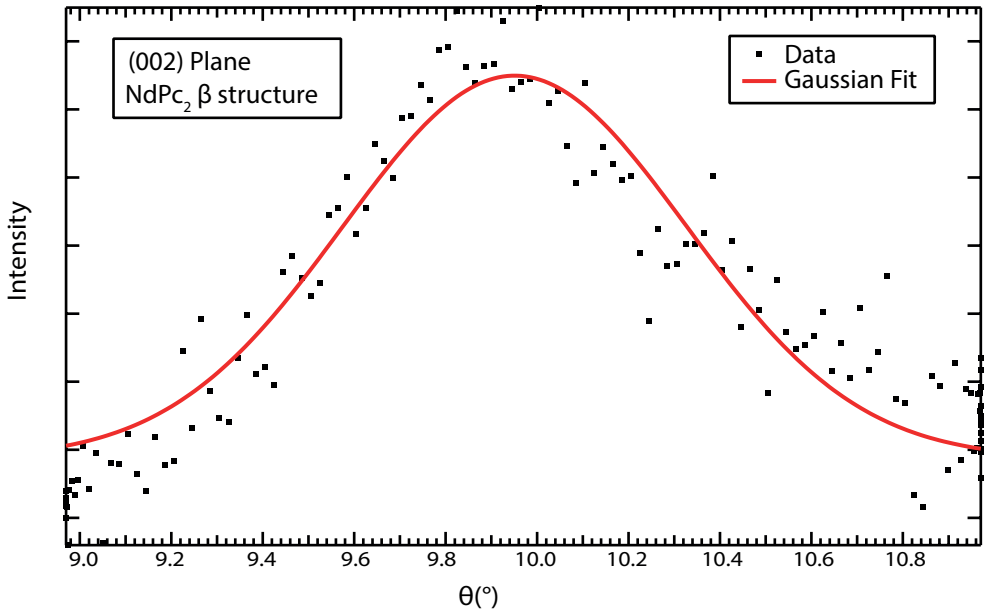

FIGURE 3.8: Specular scan around the (200) peak of the β structure of $LuPc_2$ deposited on Au(111). Red line is the Gaussian fit of the experimental data.

be used to calculate the average thickness of the crystallites (τ) by use of the Scherrer formula: $\tau = \frac{0.92\lambda}{FWHMcos\theta}$ (λ is the incident wavelength and θ is the Bragg angle). The FWHM deduced from the fit in Figure 3.8 is 0.531°, which translates to grain thickness of 11.6 nm, compatible with the thickness value estimated with the SDRS, which is 13±2 nm, see Figure 3.8, meaning that the crystallites extend throughout the whole sample. This is important because it shows how the templating effect of the substrate is not limited to the first monolayer, but is maintained throughout the whole film.

In-plane Geometry The relative orientation of the substrate and the overlayer as well as the inplane lattice parameters has then been extracted to extend the informations obtained in the lab. The main directions the gold substrate were measured with a Gaussian fit on the (110) peak, giving ω=23.9°. Then an in-plane ($q_\perp$=0.07) map of one of the symmetry domains of the overlayer was taken, and is shown in Figure.3.9. Two series of spots are seen: one at $q_{||}$=0.47 $Å^{-1}$, and the other at $q_{||}$=0.66 $Å^{-1}$, which are assigned to the (110) and (200) reflection of the β structure respectively. From this, using Bragg formula it is possible to calculate the inplane lattice of $LuPc_2$, which is a square lattice with **a**=19.43 Å. The fact that the spots are aligned in the reciprocal space is a proof that the in-plane unit cell is squared. From the periodicity of the peaks the exact angle can be calculated, giving 90.0±0.1°. The distance between the molecular centers can be found from geometrical reasoning to be 13.4 Å.

From the lines extracted from the scans in Figure 3.9 bottom, it is possible to note

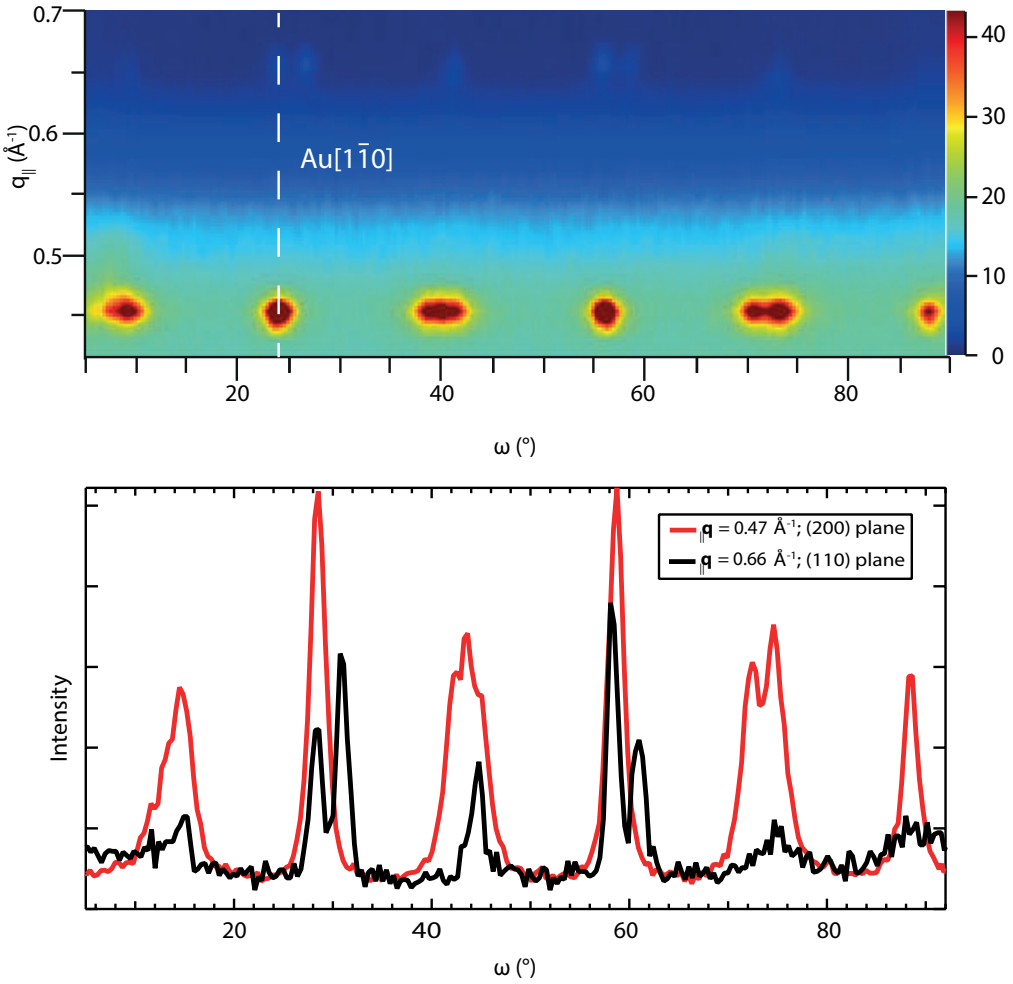

FIGURE 3.9: (Top)In-plane mesh (l=0.05) of the $LuPc_2$/Au(111) sample after heating to 285°C . The position of the 110 peak of gold is at 84.0±0.3°, marked by the vertical line. (bottom) cut along two lines to evidence the alternating pattern of the peaks.

that half of the peaks are split in two. The alternance is in both cases single/double, while, comparing the two scans it is possible to see that to every double peak in the (110) plane correspond a single in the (200) and vice versa. The period between two (double or single) spots is roughly 30°, and the period between two spots (no matter which ones) is 15°. This accounts for a total of 24 domains, which divided by the 6-fold symmetry of the substrate and the 4-fold symmetry of the overlayer reduces it to 2 inequivalent symmetry orientations. The alternance of the single and double peaks between the two different planes can be rationalized like that: The (110) reflection is along the diagonal of the unit cell, while the (200) is along one of the sides. This implies that there is a shift of 45° between the two, which, along with the periodicity of the peaks, shows that every double reflection of the (110) plane corresponds to another (200) double peak. These are shown in Figure 3.10. The first configuration shown in Figure 3.10(top) is relative to the single peaks in Figure 3.9. In this case the diagonal of the unit cell is aligned along one of the close-packed directions of the substrate (for example the [$\bar{1}$10]. It has to be noted that a slight misalignment

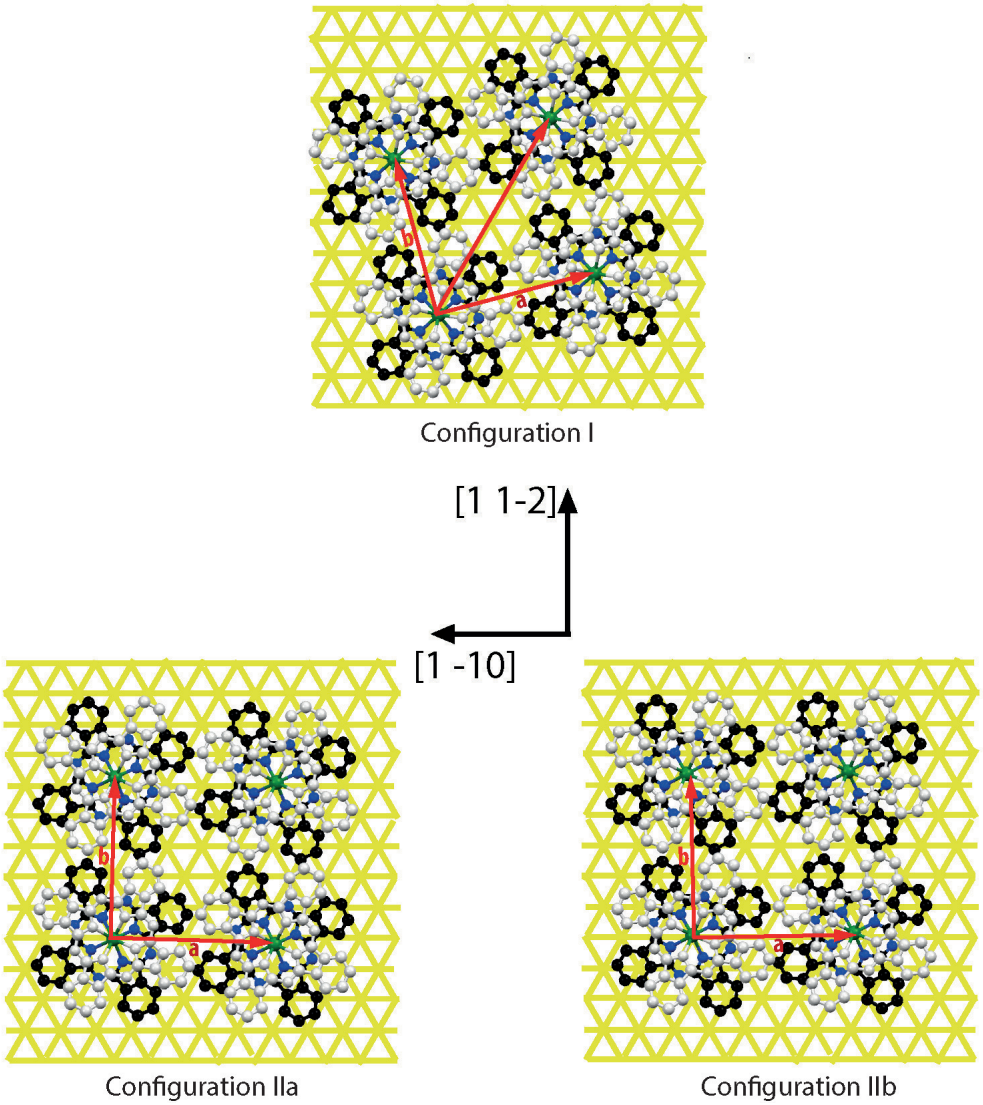

FIGURE 3.10: The different symmetry inequivalent domains of $LuPc_2$ over Au(111). Only the lattice directions of the substrate has been shown as the exact adsorption point could not be extracted from the XRD measurement presented here. The upper $LuPc_2$ plane has been coloured in light grey for clarity. In red the vectors relative to the intermolecular distance are shown, as taken from the β phase, which has the following unit cell: a=19.43$\pm$0.1 Å, b=19.43$\pm$0.1 Å, γ=90°.

is present, as the diagonal of the unit cell forms an angle of 0.12° with the [$\bar{1}$10] direction. The coupled spots in the diffraction pattern are relative to domains 2a) and 2b). The unit cell axis is aligned with the [11$\bar{2}$] family of directions of gold, which is the direction of the corrugation that form the herringbone reconstruction. This leads one of the axes of the benzene rings to directly align with the corrugation of the herringbone reconstruction, while the other align on the [110]. The template effect of the substrate is therefore evident. It was, however, impossible to show if the templating effect is due to the herringbone corrugation, and is therefore a morphological effect or to the close-packed directions of gold, where the van der Waals interaction between the molecule and the substrate are more intense due to the higher atomic density, and therefore is an electronic effect. Zhang et al. [155] have performed STM measurement on YPc_2 deposited on herringbone reconstructed Au(111), they deposited the molecule at room temperature and then transferred the sample in a liquid helium cooled STM where the analysis took place. They showed that the elbows of the herringbone reconstruction were preferential nucleation sites for the small square islands that formed at low coverage. Later Toader et coworkers [138] performed STM analysis on $LuPc_2$ deposited on Ag(111) which does not reconstruct with the herringbone pattern. They evidenced a preferential growth along [1$\bar{1}$0] and the perpendicular direction [11$\bar{2}$], suggesting a strong molecule-substrate interaction. From the two works presented above, we can deduce that even if the herringbone might influence the nucleation site of the islands, it is most likely that the Van der Waals interaction between the sample and the substrate that are dominant for the templating effect of the substrate. This is confirmed by the same order shown on a substrate with the same geometry and a similar electronic structure, but which shows no surface reconstruction. Interestingly the unit cell is not perfectly aligned with the herringbone reconstruction, but present a slight misalignment which, due to symmetry conditions, gives rise to the two different domains. It has to be noted that the two domains are not offset of the same angle from the direction: -1.71° and 0.98° from the [110] direction. The first domain instead present only a low misalignment, which does not generate any twin domain. This is consistent with what has been observed by Kato and his group [74, 75], who described the adsorption of sub monolayer of $REPc_2$ and H_2Pc on herringbone reconstructed Au(111). They showed that the benzene axis aligns with one of the closed packed directions of the substrate ([110] or equivalent) to increase the contact area and therefore increase the stabilization due to the van der Waals interaction. It was shown by Cheng et al. [24] that FePc at the submonolayer coverage adsorbs on two different configurations: either with the benzene axis parallel to one of the closed packed directions (configuration I), either with the same axis rotated by 15° (configuration II). However they also showed that increasing the coverage, the configuration II disappeared due to the stronger molecule/molecule interaction respect to the molecule/substrate. Also they showed that the ridges and in particular the elbow of the curving ridges act

as a preferential adsorption site. The two configurations are in fact the two different domains that we were able to differentiate during our measurement. Regarding double-decker phthalocyanine the adsorption happens in a similar way. The group of Katoh have extensively studied the absorption of double-decker phthalocyanine on Au(111), see for example ref. [75] and reference therein. They argued that the absorption geometry stays the same, due to the similarities between the underlying molecular plateau and a metal-free phthalocyanine. It was in fact shown by Katoh [75] that the lower Pc ring has the axis aligned with the close-packed direction of the substrate.

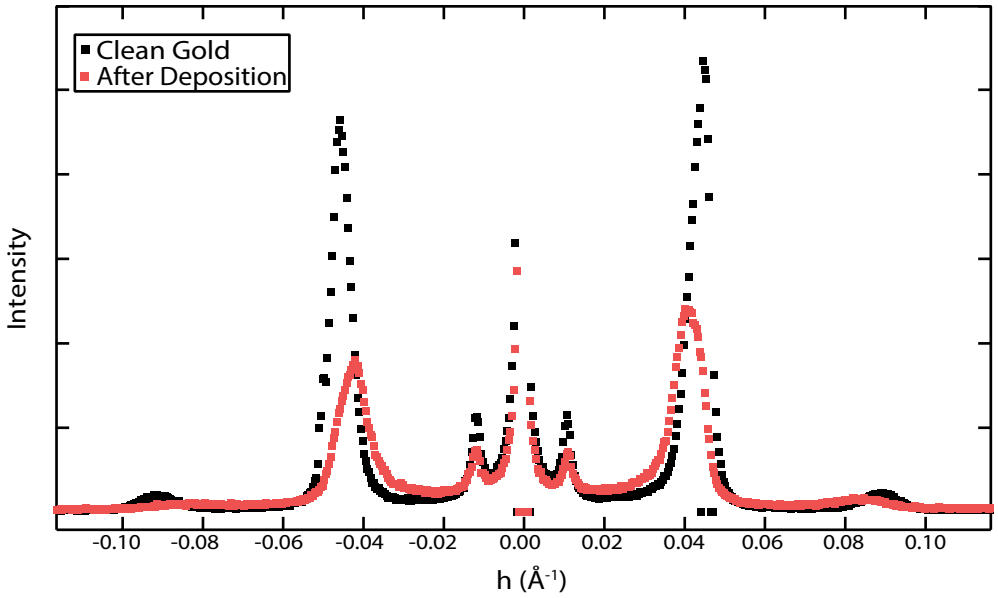

FIGURE 3.11: h scan (0.9<k<1.1; l=0.05) of the $LuPc_2$/Au(111) sample around the $(1\bar{1}0)$ peak of the substrate.

The effect on the herringbone reconstruction is shown in Figure3.11. First thing to be noted is that the reconstruction is not lifted after the deposition of the film. It is in fact just slightly modified: the third order of the reconstruction is no longer seen after the deposition, which is due to a loss of long-range order. More interesting is the effect on the first order peaks of the reconstruction. They both lose intensity (around 60%) and shift towards lower **q**. The average position before the deposition is **q**=2.51 $Å^{-1}$, while after the deposition it is **q**=2.42 $Å^{-1}$. This shrink in the reciprocal space is equivalent to an expansion in the real space, i.e. the reconstruction gets looser due to a reduction of the surface stress. A similar result was obtained by Wang [144] who deposited alkaline metals on herringbone reconstructed Au(111), showing a loosening and even a lift of the reconstruction with increase of the deposition. This was interpreted as a consequence of the charge transfer from the substrate to the overlayer, which helped reducing the electronic repulsion that causes the reconstruction. Similarly here, a charge transfer is expected to occur, probably smaller than the one experienced for metal-free phthalocyanine [10], that also serve to stabilize the β structure.

Conclusions In conclusion, we were able to measure the structure of $LuPc_2$ over different substrates.
When thermally evaporated over low interacting substrates like H terminated Si(100) the molecules are semicrystalline and assume the same structure as in the single crystal: a herringbone structure referred to as γ, with the long axis of the unit cell perpendicular to the substrate surface, having therefore the molecules standing edge-on on the surface.
When deposited over metallic surfaces instead a weak interaction takes place, which allows for the molecules to lie flat on the surfaces, in the metastable α, which can be transformed in the more stable β phase upon annealing. The templating influence of the substrate , in the form of van der Waals forces, is also strong enough to direct the growth of the domains of the organic overlayer. These domains orient along the close-packed direction of the substrate to maximize the electronic overlap.

3.2 Surface Morphology of $LuPc_2$ Thin Films

After analysing the averaged structure, we concentrated our attention on the local morphology of the thin film at the nanoscale. To study this aspect STM measurement both at room temperature and at low (liquid nitrogen (LN)) temperature was performed on a VT Omicron STM. The instrument is composed of two chambers both with a base pressure in the high 10^{-11} mbar. The first one is a preparation chamber, with an ion gun, a heating set up and the evaporators for the molecules. The characterization techniques available are Low Energy Electron Diffraction (LEED), Auger Electron Spectroscopy (AES) and SDRS. The second chamber contained the microscope and a sample storage space. The Au(111) sample was prepared in the preparation chamber by thermal evaporation on a freshly sputtered and annealed reconstructed surface. The surface of the substrate was checked by both LEED and STM. The evaporation was followed in real time via SDRS confirming that the deposition was of $LuPc_2$. Then the sample was moved into the STM chamber. The pressure never exceeded the low 10^{-8} mbar during evaporation, and quickly recovered to the base pressure, in the low 10^{-10} mbar regime after the evaporation.

3.2.1 Au(111)

Measurements on Au(111) were taken mostly to find the main directions of the substrate and to calibrate the displacement of the piezo ceramics in both the lateral and z direction. The results are shown in Figure 3.12 a). This and all the following images have been treated as follows: a plane or a curve has been subtracted to have flat terraces, the piezo have been calibrated in the z directions on the step size of Au(111), 2.35$\pm$0.02 Å (the z resolution of the piezoelectric has been calculated as the standard deviation of a line profile along what should be a flat line; particular care has been taken in levelling the data before this procedure). Also eventual sources of noise like electronic noise, springs vibration, low frequency noise due to mechanical

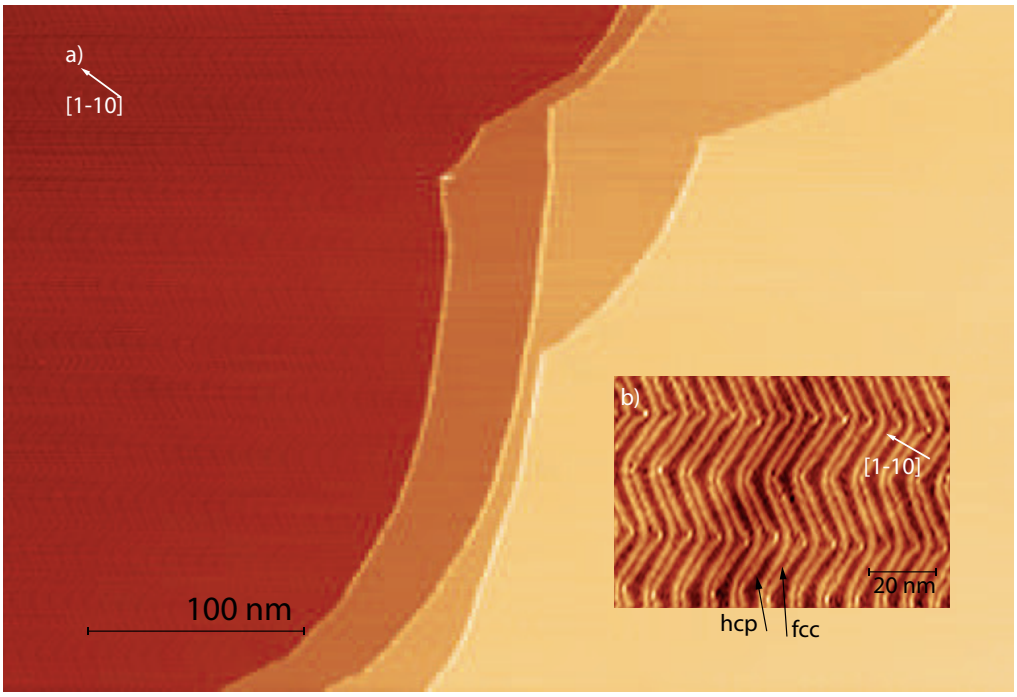

FIGURE 3.12: STM images of the Herringbone reconstruction of Au(111). Large scale a) and small smaller scale b). V=-0.3 V, I=300 pA.

heavy work in the vicinity of the STM room have been removed by FFT filtering. The clean surface is clearly seen in Figure 3.12, with large flat terraces spanning over several hundreds of nm, separated by monoatomic steps. The steps are not straight, but proceed in a curve until a kink, as expected from a hexagonal surface. Even at this large scale it is possible to see the zig-zag of the herringbone ridges. Starting from the ridges, the close-packed directions are found and are indicated by an arrow. In the zoom (Figure 3.12 b)) the ridges are shown with better resolution, they are less than 0.1 Å high, and the dimension of the fcc domains is 3.7 nm in average, while that of the hcp is 5.5 nm. Note the imperfection on the elbows, which always have the right ridge taking a longer path (closing the gap in the right turn and leaving a small hole in the left turn). This has been indicated a possible nucleation site for molecular domains [155].

3.2.2 $LuPc_2$ thin films

As deposited and annealing effects A typical image of the sample a few nm thick (3 nm, as calculated from the SDRS signal) as deposited is shown in Figure 3.13. A lot of instabilities are present due to the mobile molecules: the stripes are caused by the repeated adsorption and release of the molecules on the tip. The sample presents a continuous underlayer with several islands growing on top. The film growth is quite homogeneous as shown by the profile on the right, which shows the height of the islands of around 0.8 nm.

After a slight annealing at 250°C for 10 minutes the film becomes more ordered, as

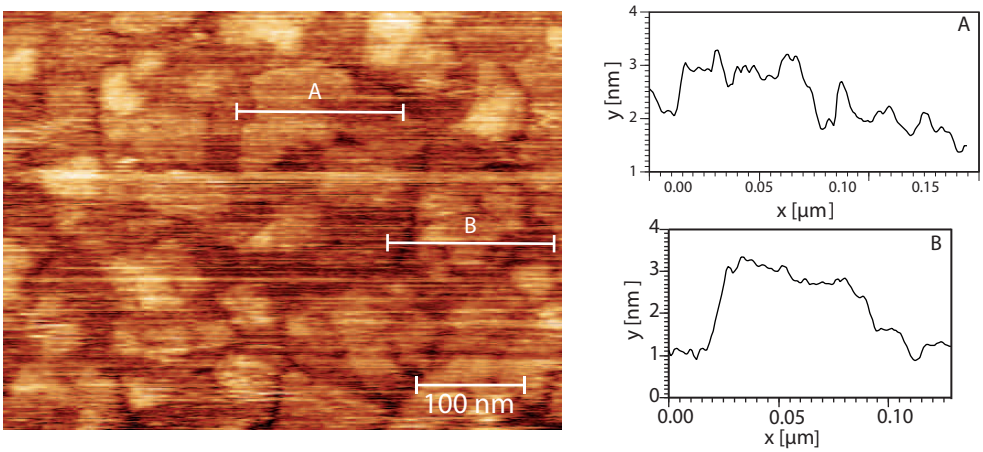

FIGURE 3.13: Large-scale image of the sample as deposited, V=-2 V; I=300 pA, on the right the height profile on the showed lines labelled A and B.

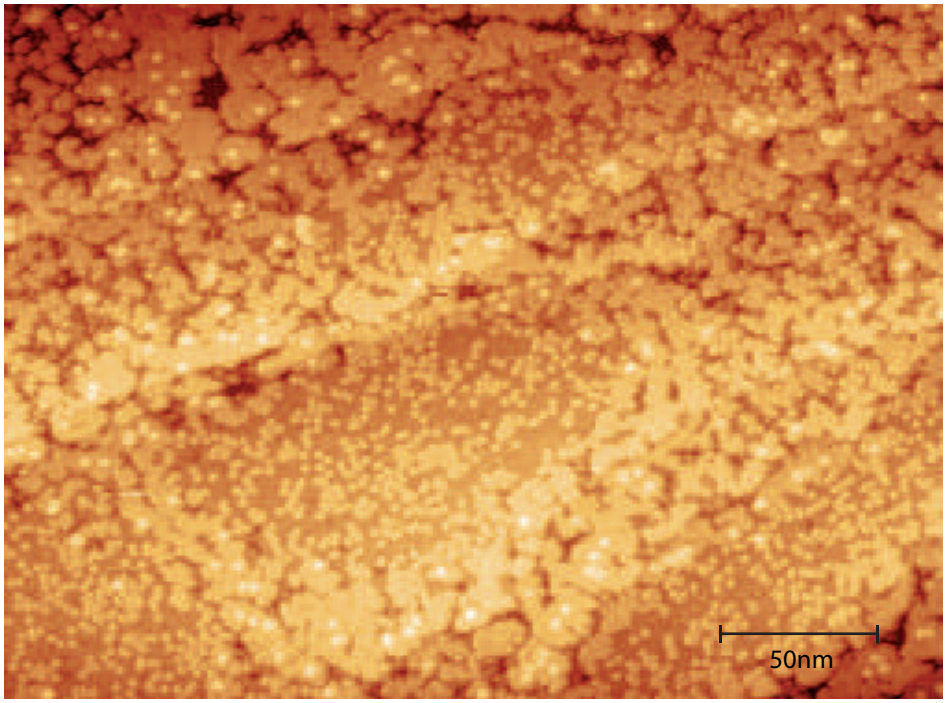

FIGURE 3.14: Large scale STM image of the sample after 10 minutes annealing at 250°C. V= -3 V; I=300 pA.

seen in Figure 3.14. The step edges appear to be a preferential nucleation site, showing that probably the mobility of the molecules across the edges is not activated at this temperature. The molecules on top of the terraces do not seem to follow an order, some almost square domains are seen, but most of the time no principal directions of domains growth are evidenced.

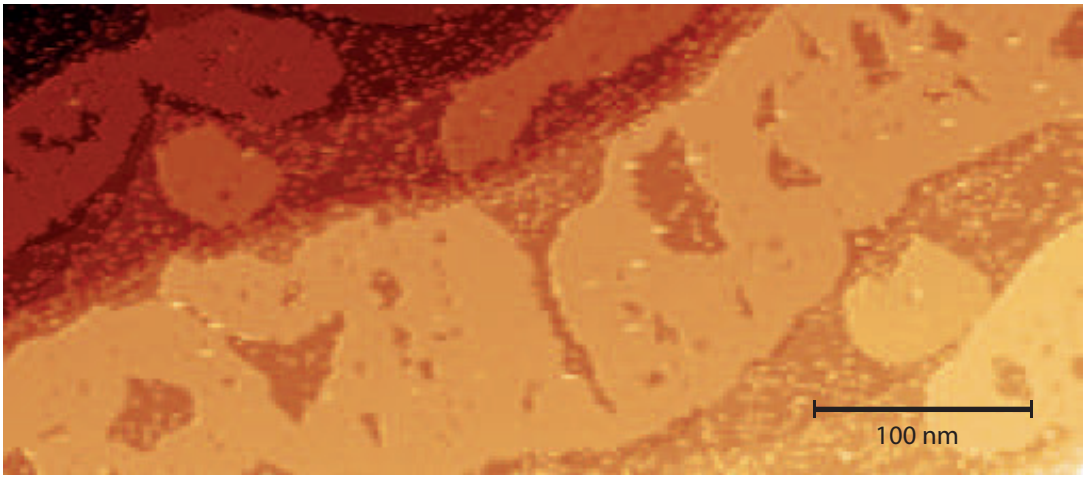

FIGURE 3.15: STM image at large scale of the flat islands that appear after 15 minutes at 300°C. The tilting of the image is due to the drift correction, as explained in the experimental section. V=-3.9 V; I=300 pA.

From Self-Assembled Layer to 3D Packing After further annealing (15 minutes at 300°C) the film presents a peculiar morphology, as shown in Figure 3.15. The large flat terraces are still present, and, even if not well resolved, they are clearly composed by molecules. On top of it, isolated free standing molecules are present, and also flat islands of up to a hundred nm in diameter. The islands have sharp edges, and often present a doughnut shape, with a hole of several tens of nm in the middle. In general all the islands present extended defects (holes) of an irregular shape. In images taken at small scale (< 100 nm) where low noise was present (i.e. few mobile molecules on the surface) it is often possible to see the individual missing molecules that lead to the holes, which usually measure between a couple and a few tens of molecules. The most interesting feature of these islands is evidenced by the height profile shown in Figure 3.16 it is shown a line that comprehends different steps: starting from the left we see a step from the bottom plateau to the upper plateau, then a step from the upper plateau to the island, a step from the island in the hole and a step from the hole to the island again. The sketch in Figure 3.16 (bottom) shows that the island is twice as high (6 Å) with respect to the underlying plateau (2.6 Å). The height is the same both respect to the outer terrace and to the inner hole. This means that the whole island is composed of a double layer of molecules, lying on a single layer one. Indeed the underlying terrace is composed of a single layer of molecules as can be seen from the model depicted along with the profile line. This cannot be an

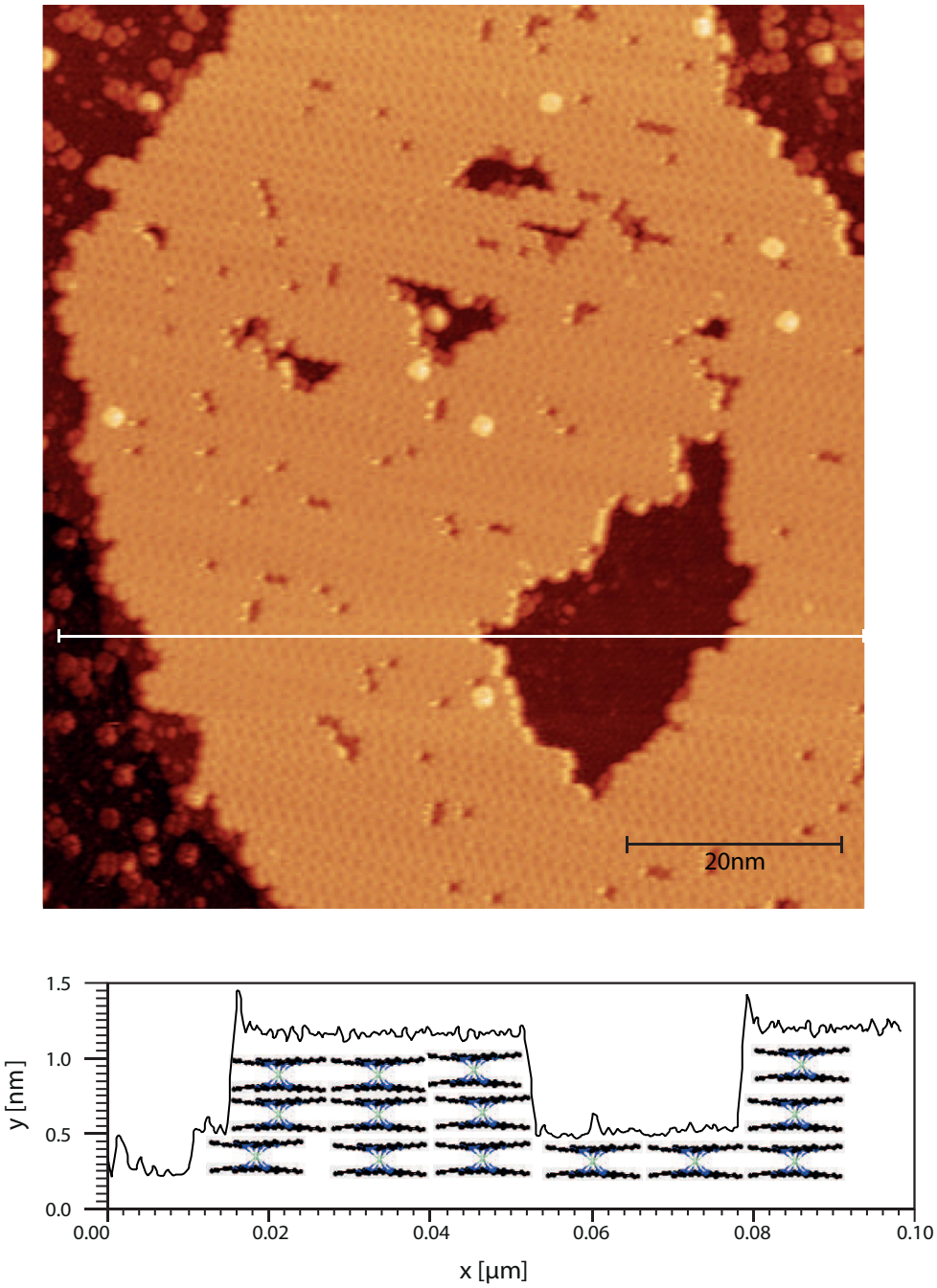

FIGURE 3.16: top: STM image of an island. V=-2.6 V; I=300 pA; bottom: profile obtained over the line shown on the STM image, with a depiction of the molecular stacking (the horizontal axis is not on scale).

Au(111) step due to the higher height and most important the irregular shape. The same behaviour has also been measured on a sub monolayer coverage [8], but the statistics were not sufficient to deduce a general tendency at larger scale. A similar stacking geometry (i.e. bilayer growth) was described for Titanyl Phthalocyanine on Ag(111) [80] and HOPG [112]. The molecule is composed by a single phthalocyanine ring with at TiO group as a central cation, with the Ti atom in the middle of the cavity and the O protruding. Both these works showed that these molecules present a strong intermolecular dipole-dipole interaction. This interaction is screened by the metallic substrate for the first few layers (more in the case of Ag, showing the better screening capabilities), leading to a layer by layer growth. After this "buffer layer" the growth starts to be bilayer by bilayer, with the two titanyl groups facing each other, but staggered, so to have the negatively charged oxygen of each group in front of one of the benzene group's hydrogen atom. This leads to a strong stabilization due to the hydrogen bond. Such dipolar moments are not found in the $LuPc_2$, so other hypotheses have to be made. The adsorption energy for a molecule on top of another molecule has been calculated by DFT, and found to be 4.6 eV per molecule as was calculated by J. Luder (University of Uppsala). This is a very high value if compared to other phthalocyanine, which can explain the Stranski-Krastanov growth mode, but not the stop at two layers. To fully understand this phenomenon further calculation are needed.

It is complicated to fully resolve smaller holes, but for the intermediate one (some tens of missing molecules, as the one shown in Figure 3.17) different situations can be found: in some cases the edges are two molecules deep and sharp all around the hole, meaning that the upper layer is either perfectly aligned with the underlying one, or it protrudes towards the hole. In other cases molecules are seen in the hole which do not look like isolated molecules but as molecules in a lattice. The first case, however, is drastically more common. Instead for the larger holes (the ones in the middle of the islands) as well as for the outer borders the step is perfectly sharp except for rare exceptions. Also molecules are often found lying on top of the incomplete layer, suggesting an island-like growth. This is consistent with a Stranski-Krastanov mixed growth process which was already described for thick films of $LuPc_2$ on low interacting surfaces [12].

Stacking The stacking between different layers can be studied by looking at different features of the thin films. Holes, if resolution is achieved inside, can give information on the ordering of the underlying layer, hole edges sometimes have molecules from the underlying layer peeking out, which can give information on the relative orientation. Also isolated molecules over a lattice (which might lead to the nucleation of the successive layer) can be looked at to see if any preferential orientation is present. This is particularly important since isolated molecules are fixed in the overlayer, again due to the high adsorption energy. Figure 3.17 shows the hole in a doughnut shape, which was large enough to resolve at least the directions of the

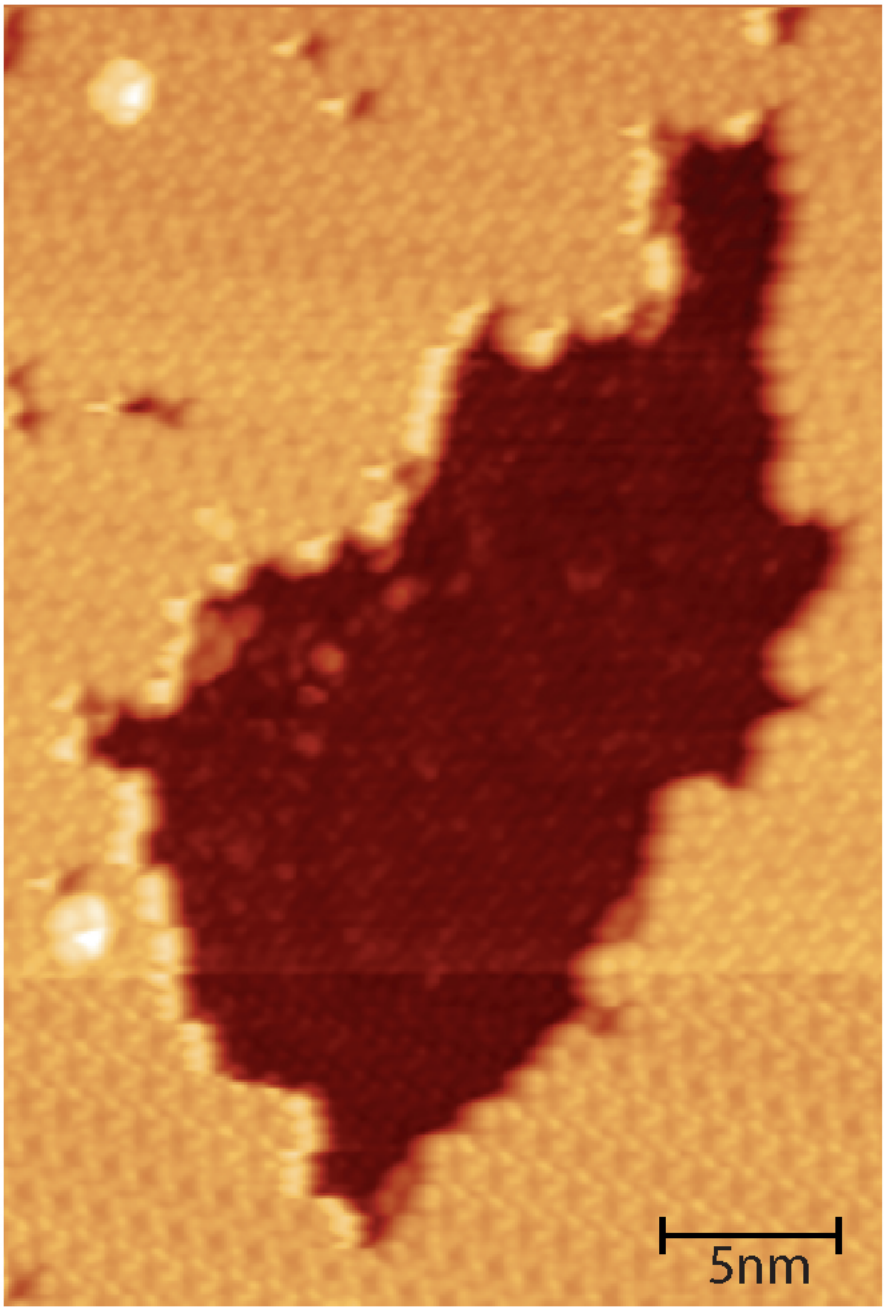

FIGURE 3.17: Magnification of the hole shown in Figure 3.16.

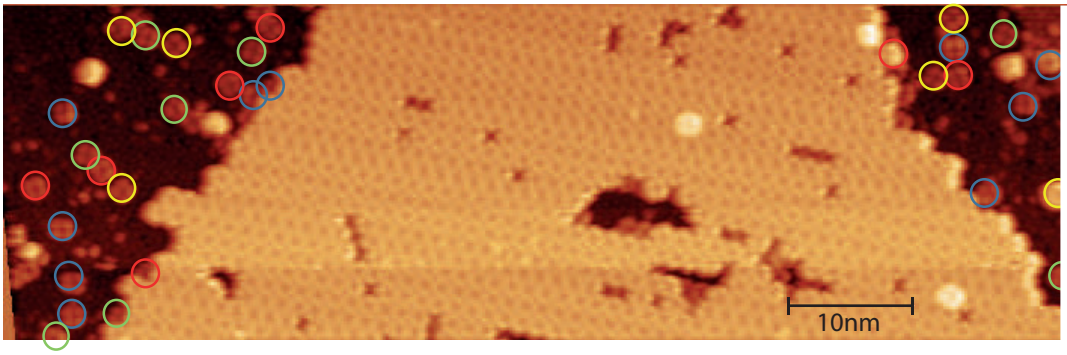

FIGURE 3.18: STM image of an island with some isolated molecules on the underlying plateau. The different colours of the circles showing the different orientation of the molecules on the underlying terrace. V=-2.5 V; I=300 pA.

layer. It has to be kept in mind that the island is formed by a double layer. Although not well resolved, it is possible to recognize ordered lines in the hole, which are interpreted as the orientation of the benzene groups of the molecules. It can be seen that the benzene groups in the hole are oriented in the same direction as the majority of the benzene in the topmost layer (domain A). Also no changes in the benzene orientation are seen in the underlying layer, meaning that only one domain is present.

A lot of isolated molecules can be found either on top of the island or on the underlying terraces, which are well suited to study the intermolecular interactions that lead to the growth of successive layers. In Figure 3.18 the different orientations of isolated molecules on a plateau are evidenced. It is clear that no preferential orientation is found, and a greater statistics on other images did not give any further insight. This is because isolated molecules have different adsorption geometries, all of which allow for a favourable piling of the benzene rings. Better information can be deduced from looking at the isolated molecule adsorbed on top of the islands, as in this case resolution on both the layer and the molecule can be achieved. In this case some striking effect can be found. In Figure 3.19 a few different geometries are shown. Figure 3.19 a) shows for example a molecule that is adsorbed exactly on top of the underlying (assuming that the underlying molecule is oriented in the same way as the adjacent molecules in the lattice). This leads to a face to face contact of the benzene group of the two molecules, which should be highly unfavourable due to the benzene-benzene electronic repulsion (see ref. [70]). This can be explained by taking a closer look at the frontier orbital of $LuPc_2$, as were calculated by Bidermane and coworkers [10] and shown in Figure 3.19 e). This shows the asymmetry of the electron density on the benzene ring, which can lead to an attractive interaction if the electronic densities are on the opposite sides. To verify this hypothesis further calculations are needed. This is indeed the most frequently observed adsorption geometry. In Figure 3.19 b) a second possibility is shown, with the molecule on top having the benzene rotated of around 50° respect to the ones of the underlying molecule. Again the lower benzene rings of the upper molecule arrange on top of

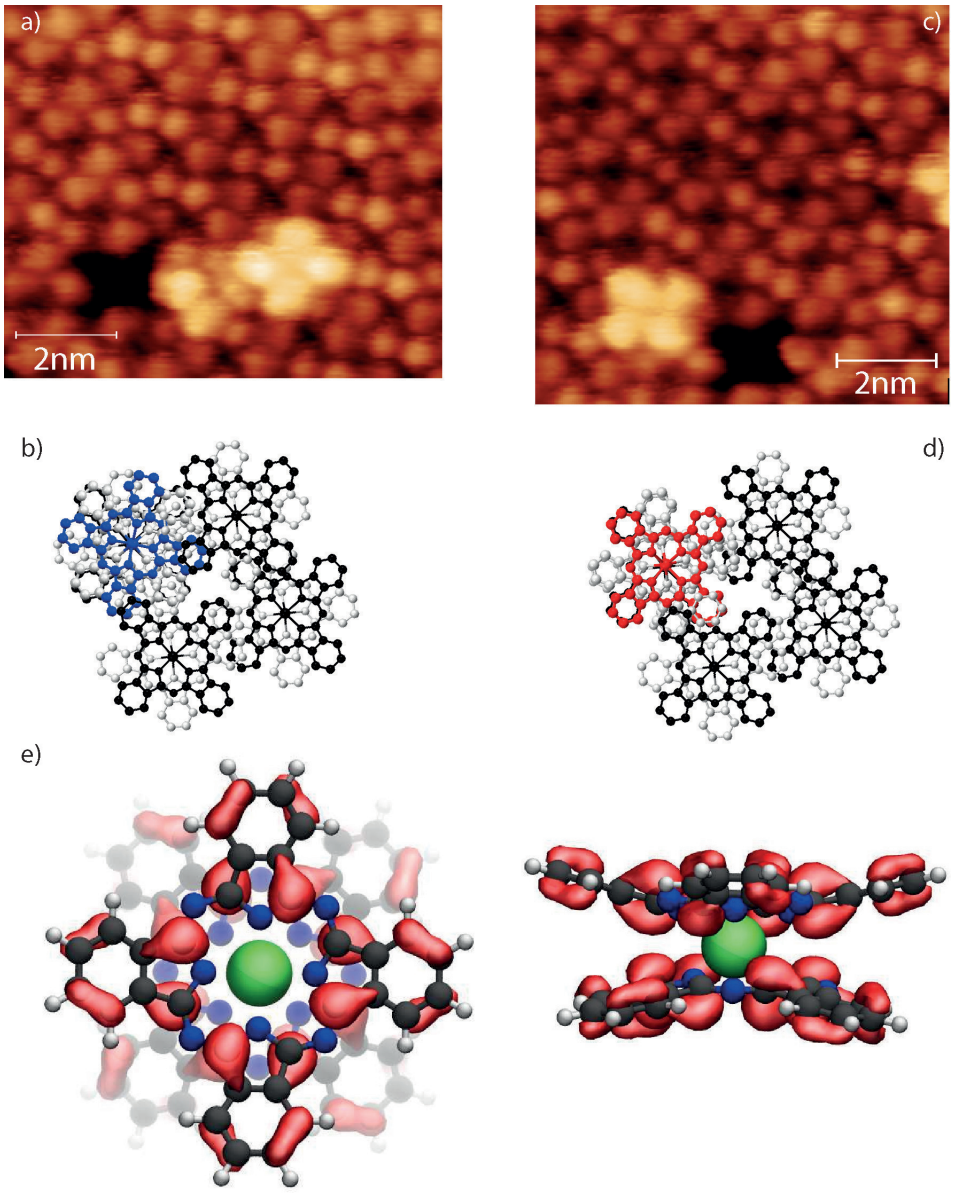

FIGURE 3.19: (a-b)STM image and molecular model of the "on top" adsorption configuration V=-2.5 V; I=300 pA; (c-d) STM image and molecular model of the "staggered" configuration V=-2.5 V; I=300 pA; (e) molecular orbitals of $LuPc_2$ as calculated by DFT in ref. [10].

the benzene of the underlying one as can be seen from the model in Figure 3.19 c). On the contrary the adsorption on the underlying layer seems not to present any preferential orientation.

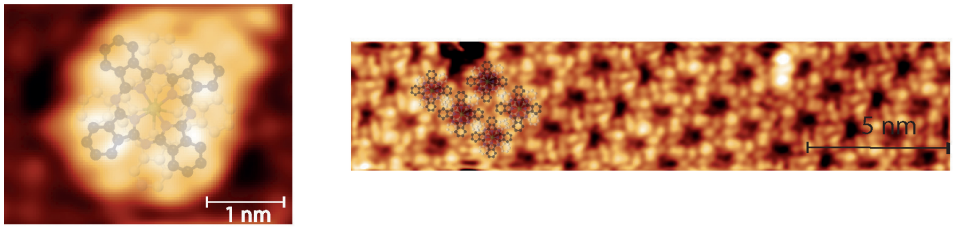

FIGURE 3.20: STM image of a single isolated molecule (left) and of a few molecules in the lattice (right). The molecular model is superimposed. V=-2.5 V; I=300 pA; At the bottom the DFT calculated Lattice for a single layer of $LuPc_2$ deposited on Au(111).

Molecules Aspect It is interesting to study the variations in molecule aspect when included in the lattice. The lattice has been calculated by DFT (again by J. Luder) for a single layer of $LuPc_2$ in vacuum. It shows a square unit cell of 13.4 Å, and the angle between the molecular axis and the unit cell vector is 25.8° as shown in Figure 3.21. When isolated on a surface $LuPc_2$ molecules look like the one shown in Figure 3.20. In the isolated case the molecule has a square shape, with rounded edges. The eight lobes are due to the electronic density on the four benzene rings of the upper phthalocyanine ring, with each benzene ring giving rise to two lobes due to the splitting of the electronic density, as was calculated by Bidermane et coworkers [10] and experimentally shown by for example Toader and coworkers [138]. The two dark lines in that cross in the middle correspond to the spaces between the benzene rings. The hole in the middle is due to the low electronic density on the central Lu cation. There has been a debate about the possibility of seeing the 4f states of the rare earth cation via STM. They are strongly localized, and do not take part in forming any molecular orbital [107] (the HOMO-2 has a slight Lu 4d character), nonetheless Warner and coworkers recently demonstrated the accessibility of the 4f orbitals of Nd in $NdPc_2$ [46] and of Dy in $DyPc_2$ [148] adsorbed on Cu(100) by means of combined STS and DFT approach. It has to be kept in mind that Nd and Dy are both early elements in the lantanide series, and have an electronic configuration $4f^{10}5d^{0}6s^{2}$ for Dy and $4f^{4}$,$6s^{2}$ for Nd. This directly implies that one of the electrons donated to the Pc ligands is a 4f electron. This also means that the orbitals are closer to the vacuum level, making them more prone to be influenced by the ligands or by the surface states of substrate. In contrast are the results presented by Zhang and coworkers [154] for $DyPc_2$ on Au(111), who performed STS and STM at low temperature and found no signal from the Dy 4f orbitals. Similarly all the topographical images reported for RE Pcs [138, 75] adsorbed on less reactive noble metal surfaces (Ag(111), Au(111)) present a molecule with 4 or 8 lobes (depending on the image resolution), which belongs to the benzene ring, with a dark centre.

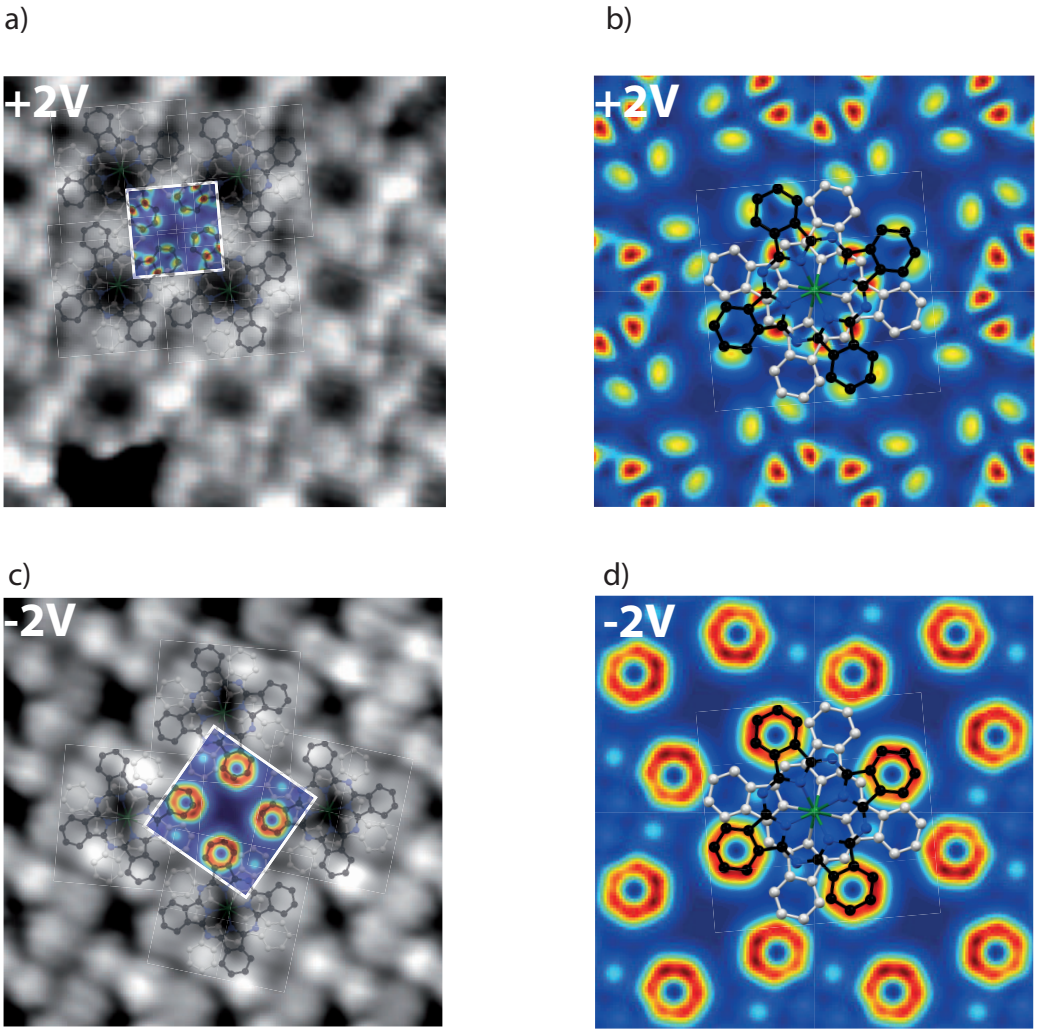

FIGURE 3.21: Top left: STM image at V=2 V, with superimposed the calculated DOS and the molecular ball and stick model; Top right: the calculated DOS at V=2 V with superimposed the molecular model. Bottom left STM image at V=-2 V, with superimposed the calculated DOS and the molecular ball and stick model; Bottom right: the calculated DOS at V=-2 V with superimposed the molecular model. The lower Pc ring is coloured in light grey for clarity.

When included in the lattice instead, the shape of $LuPc_2$ as seen via STM is modified, as shown in Figure 3.20 (right). The frontier orbitals are constrained by the nearest neighbours, as is demonstrated by the molecules on the edge of a defect, which shows the "in lattice" orbital shape on the sides exposed towards other molecules, and the "isolated" shape on the sides towards the hole. Also the molecule apparent radius (calculated as the distance between the centre of two dark spots in the case of the molecule in the lattice, and as the "FWHM" in the case of the isolated molecule) reduces from 22±0.1 to 21 ±0.1Å (the error bar was measured by statistics on the distance between the centre of two adjacent molecules, i.e. the distance between two black spots; dependence on image size, scan speed, and scan angle have been taken into account).
The aspect of different molecular orbitals has been probed by varying the scanning voltage. The results are shown in Figure 3.21. On Figure 3.21 a); c) the same calculated images are shown superimposed to the measured STM images at the same voltage while on b); d) the molecule is superimposed to just the DFT simulated images for clarity. The images have been simulated starting from the calculated molecular orbitals and the Tersoff-Harmann method to model the tip. On top the occupied states are shown, while at the bottom the empty states are shown. A very good agreement can be seen between the calculated and the measured images. It can be seen how, while the SOMO is more ball like, with the density spread around all the benzene atoms the Single Unoccupied Molecular Orbital (SUMO) is mostly localized on the sides of the benzene ring, as demonstrated by the separated spots in the simulated image.

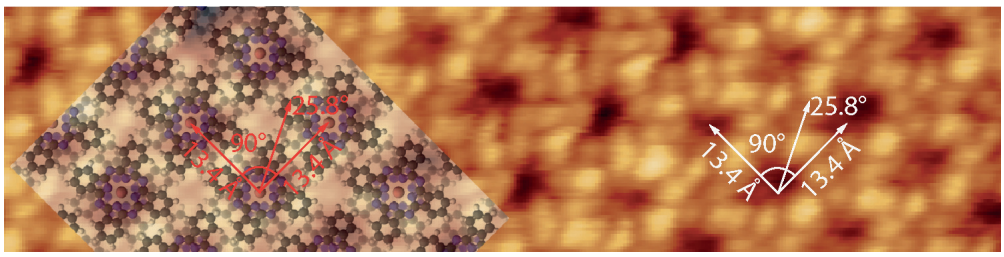

FIGURE 3.22: Calculated DFT lattice for $LuPc_2$ monolayer adsorbed on Au(111) (left), superimposed on the measured STM image (right) V=-2.5 V; I=300 pA.

Molecular Lattice The molecular lattice of $LuPc_2$ molecules in vacuum was calculated by J. Luder with the PW code, including dispersion correction. The results are shown in Figure 3.22. The angle between the lattice vector and the symmetry axis of the molecule (i.e. the axis that runs over the two opposite benzene groups) is 25.8°. The data are in good agreement with the values found experimentally, where the angle between the lattice vectors and the molecular symmetry axis is 25°. This is different from the values shown by Toader and coworkers [138] and for the single crystal, who both report a rotation 45°. The rotation is due to the molecule-molecule

interaction during the self-assembly: the driving force is the superposition of the benzene rings of the upper macrocycle with the ones of the lower macrocycle of the nearest neighbour. It has to be remembered that in the crystalline form the two macrocycles are not rotated by 45 degrees due to the Ian Teller effect,and have been measured via XRD by Darkovish and coworkers [98], as shown in Figure 3.1. This leads to the different rotation as the two different configurations are not equivalent due to the different angles between the lower and the upper plateau.

Different domains are present on the surface, as shown in Figure 3.23 right. The

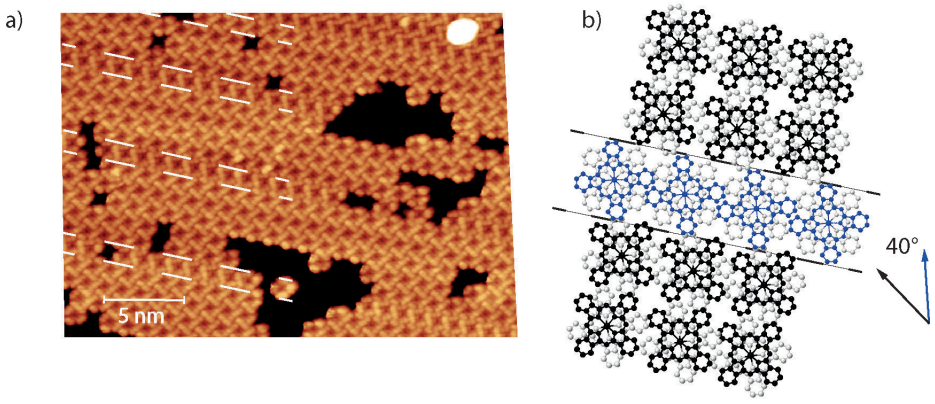

FIGURE 3.23: a) STM image showing different domains V=-2.6 V, I=700 pA; b) model of the two different domains as deduced from the STM image.

lines that cross the molecule centres are parallel throughout the island, what is changing instead is the orientation of the benzene rings. This tells us that the difference could not be told by the diffraction data we acquired as the diffraction data are not sensitive to the molecular orientation but to the orientation of the unit cell. The respective position of the molecules can be seen in Figure 3.23 left. The rotation angle between the benzene axis in the two domains was measured on the molecular model and found to be of 40°. This is lower than the value measured by Toader, which found 60° and assigned it to the orientation periodicity of the substrate. Moreover in that case no alternance of the domains was seen, but separate islands, each of them monodomain. The relative abundance of the two domains, however, is not equally split. The repetition pattern is usually 4±1 A and 1 B. The width of the domain, however, is larger of the distance between two ridges of the herringbone reconstruction, excluding a template effect from the substrate, even if different adsorption geometries were found for metal free Pcs on herringbone reconstructed Au(111). The different relative orientation of the benzene rings between adjacent molecules in the two domains is clear from the model. In fact both domains represent the same packing, only turned by 180° on the horizontal plane (i.e. the plane of the macrocycle). The grey (lower) plateau in the black domain are in the same respective position as the blue (higher) plateau in the blue domain. It is interesting that even if these two

domains should have a quite similar energy the blue one is found on only one every four or five lines. A hypothesis is that the interaction with the underlying layer can act a stabilizing factor for the high energy configuration, which is therefore unfavourable at the surface.
It is interesting to see the rearrangement of the molecular orbitals in presence of a defect which acts as a twining nucleation point.

3.3 Conclusions

The molecular structure of $LuPc_2$ (and in general of $REPc_2$) thin films is dictated by electronic interactions. It is strongly influenced by the substrate and its electronic morphology at the surface, and it is driven by the interaction between the benzene rings for the stacking but not in-plane. When deposited on a metallic substrate, the molecules adopt the metastable β phase instead of the slightly more stable γ phase adopted on less interacting surfaces. In the β structure molecules orient with the molecular planes almost parallel to the substrate surface. This is the first signature of the interaction with the substrate, which is able to stabilize the surface, the second is the relaxation of the herringbone reconstruction of the gold substrate, which is explained as a charge transfer from the substrate to the molecular layer. Another evidence of this interaction is the alignment of the unit cell of the molecular layer on the close-packed direction of the substrate. This is due to the increased favourable Van der Waals interaction between the molecule and the substrate and leading to two symmetry inequivalent domains. At the nanoscale level the morphology as expected present an increasing order degree with consecutive annealings. It goes from a disordered, bubble-like, corrugated thin film, to a disordered dispersion of molecules on some flat terraces, to ordered islands on flat terraces coexisting with little disordered molecules. The islands are in fact composed by a double layer of molecules, probably due to the high molecule-molecule absorption energy. We demonstrated the presence of different domains and described their arrangement in terms of the molecular position in-plane, but no conclusion can be obtained from this as the orientation seems to be random. We deduced the 3D stacking of the molecules on top of an island by studying isolated molecules. We showed two different packing geometries, where the one is with a specular position of the facing Pc ring of the two molecules is preferred with respect to the one with a "staggered" geometry.

Chapter 4

Results: Reactivity

The reactivity of organic molecules has not been largely addressed from a fundamental point of view. It does, however, influence a lot of different properties in organic-based devices [122]. Organic materials are known to exhibit different behaviours when exposed to gases rather than in UHV [61]. They might react with the gases leading for example to less conductive products, or they can even polymerize. The most common result is, however, the creation of deep traps (cfr. Chapter 22), which lead to decrease in the conductivity. But this is not the only process; Kawasaki and coworkers [72] exposed a picene film deposited on Ag(110) to oxygen, and demonstrated an increase of conductivity in the film, due to the reduction of shallow traps, especially at the interface with the substrate. This example perfectly explains the need for a thorough characterization not only of the electronic properties of organic thin films, but also of their evolution under reactive, real (as opposed to UHV) conditions.
The reactivity of $LuPc_2$ towards atmospheric gases in the thin film form has been analysed by means of different synchrotron based spectroscopic techniques: HR-XPS and NEXAFS.

4.1 Pristine molecule

Before discussing the results on the reactivity of the molecule, it is important to present what is known about its electronic structure in the pure form when deposited in thin films.

4.1.1 Electronic structure

The photoemission spectra for a $\sim$1 nm thick film of $LuPc_2$ deposited on Au(111) is shown in Figure 4.1. The survey presented in Figure 4.1(a) displays 4 peaks (the high resolution regions are shown in Figure 4.1 below): Lu 4f in the valence band (b), C 1s (c), N 1s (d) and the peak of Au 4f from the substrate. Lu 4d and 3d are not seen due to the low cross-section. The Lu 4f region shows two peaks at 8 eV and 9.5 eV relative to the 4f 7/2 state and 5/2 respectively. The C 1s region is composed by two peaks at 284.8 eV and 286 eV, with a broad shoulder at 287.2 eV. The N 1s instead presents a single peak at 398.5 eV with a large shoulder at 399.5 eV. In Figure 4.2

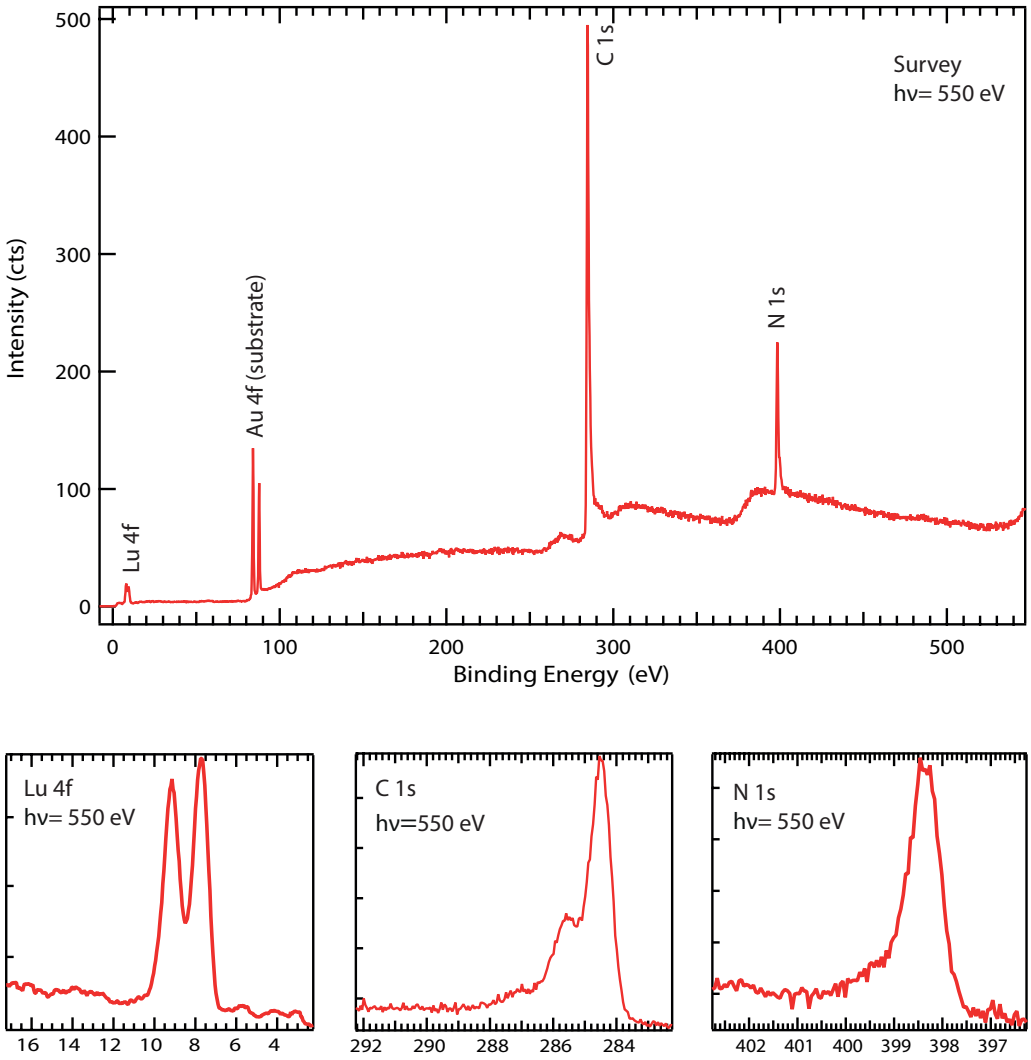

FIGURE 4.1: XPS spectra of $LuPc_2$ ~1 nm deposited on Au(111). a) Survey; b) Lu 4f; c) C 1s; d) N 1s.

the resolution of the single spectral components of the N 1s region is presented. In the case of the N 1s the main peak is fitted with just one component due to the small energy difference between the two inequivalent nitrogens (less than 30 meV) [9], but slightly asymmetric, to still take into account the difference between the pyrrolic and the azabridge nitrogen atoms. The shoulder at higher BE is assigned to a shake-up peak, resulting from an excited final state (see chapter 2). Again the shoulder is fitted with a single peak. Table 4.1 presents the results of the fitting parameters.

In Figure 4.3 the resolution of the single spectral components of the C 1s peak of $LuPc_2$ thin films is shown. Fitting of the carbon peak was achieved with four components, two for the two inequivalent carbons and two for the respective shake-up. The difference between the two different benzenic carbon (the ones with only benzenic carbon as first and second nearest neighbour, and the ones with a pyrrolic carbon as the nearest neighbour, both in black in Figure 4.3) is 30 meV [10], so with the obtained resolution they are not resolved. To still account for the two inequivalent binding energies the first peak is fitted with an asymmetric curve at 284.85 eV.

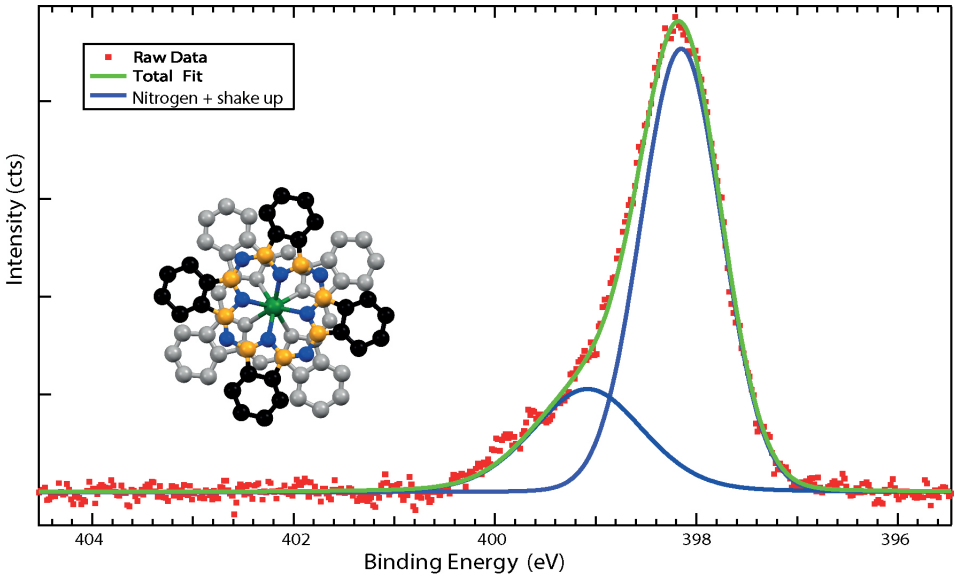

FIGURE 4.2: Resolution of the single spectral components of XPS spectrum of the N 1s peak of a $LuPc_2$ thin film (∼1 nm) deposited on Au(111).

TABLE 4.1: Peak parameters of the N 1s fitting.

Peak	Position (eV)	FWHM (eV)	Area
N	398.15	0.95	0.91
$N_{shake-up}$	399.10	1.45	0.34

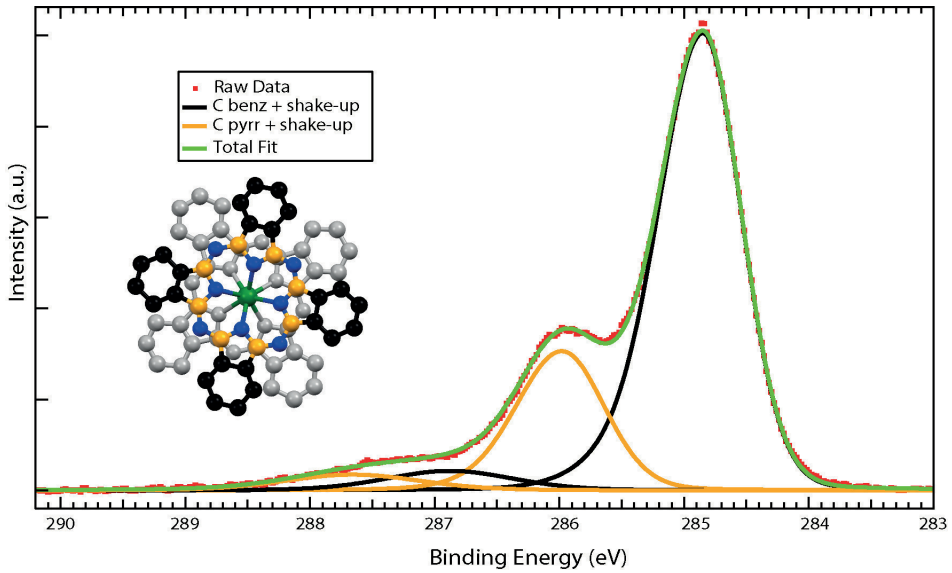

FIGURE 4.3: Resolution of the single spectral components of XPS spectrum of the C 1s peak of a $LuPc_2$ thin film (∼1 nm) deposited on Au(111).

The second peak is fitted with two different components: the first at 285.98 eV is due to pyrrolic carbon (yellow in Figure 4.3) and the second one at 286.9 eV due to the shake-up of the benzenic carbon according to Brena et al. [17] The authors of this

TABLE 4.2: Peak parameters of the C 1s fitting.

Peak	Position (eV)	FWHM (eV)	Area
	Clean		
C benz	284.85	0.73	0.49
C benz$_{shake-up}$	286.88	1.20	0.03
C pyrr	286.00	0.80	0.15
C pyrr$_{shake-up}$	287.65	1.20	0.03

study first recognized that to be consistent with the molecular composition of the molecule the ratio between the benzene carbon and the pyrrolic carbon has to be 1:3, and to obtain this ratio the shake-up peak needs to be placed at BE $\sim$286.9 eV. This is conforted by the experimental and theoretical results on the optical excitations available for the molecule, which shows a strong transition at 1.9 eV, which is close to the energy distance between the principal peak and the shake up. As it is possible to see from Table 4.2 the ratio to be used in the calculations is the total photoemission from the carbon atom, i.e. the sum of the principal peak and the shake-up, if those are employed the resulting ratio is 2.95, which is close enough to the expected ratio, remembering that uncertainties in XPS intensities are around 10%. The different energy separation between the two principal peaks and the relative shake up is probably due to the centering of the peak on a different transition. The relative position between the shake-up and the principal peak in fact may vary depending on the excited transition, while the intensity of the shake up depends on the oscillator strength [55].

The principal peak and the shake-up in N 1s peak are 0.9 eV apart in energy (see Table 4.1), which is in evident contrast with the results obtained on carbon. This is most likely due to a difference in the excited transition. It has to be remembered that the molecular orbital are localized as follows: the SOMO is mostly localized on the carbon atoms (both the α and γ, the LUMO is localized on the same C atoms and on both the pyrrolic and azabridge nitrogens [10]. The HOMO instead is mostly localized on the pyrrolic nitrogens. The oscillator strength for the different transitions were calculated by Orti and coworkers [107] who found an oscillator strength of 3 for the low energy transition that generates the J band at 0.8 eV, and a total of 10.2 for the three transitions centred at 1.8 eV that correspond to the Q band. Therefore in the case of C a HOMO$\rightarrow$LUMO is most probable, which correspond to the Q band, the most intense optical transition, located at 1.87 eV, as was measured by SDRS [13]. For a photoelectron escaping from an N atom instead a SOMO$\rightarrow$LUMO is the most probable, which is the transition known to form the strong J band situated at 0.9 eV [19]. However accurate calculations on the electronic transitions in presence of a core hole should be performed to shed light on this process. It has to be reported that the results agree well with the ones published by Toader and coworkers for the C spectrum [138] and both the C and Nitrogen spectra shown by Bidermane and

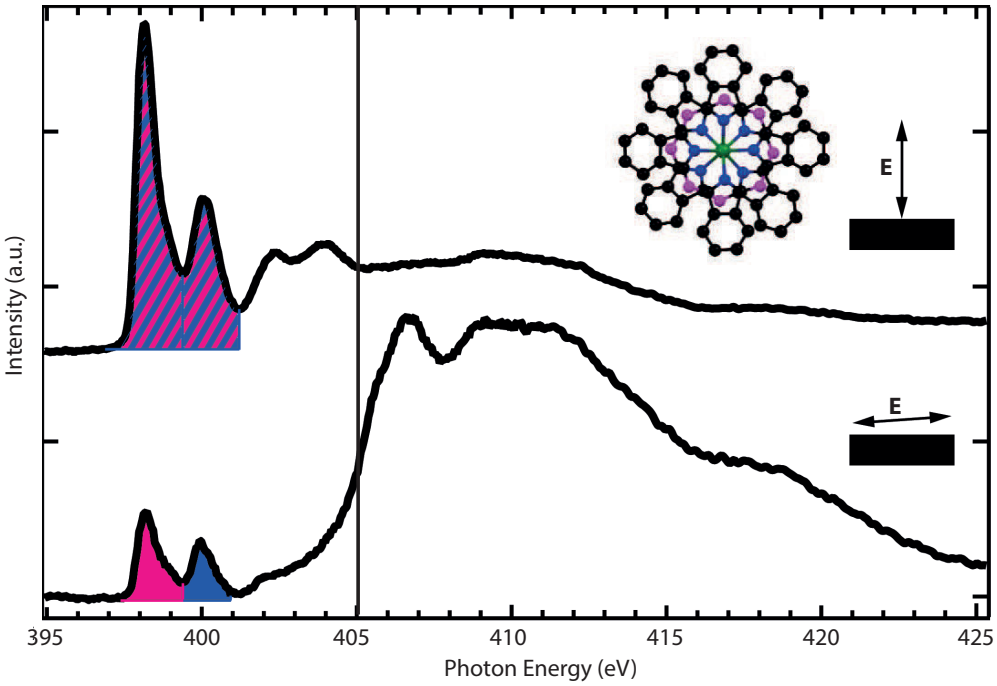

FIGURE 4.4: NEXAFS spectrum of a ∼1 nm thick $LuPc_2$ deposited on Au(111). (top) with polarization perpendicular (90°) to the surface (out-of-plane), (bottom) with polarization parallel (4°) to the surface (in-plane). The filling represents the contributions: pyrrolic (blue) and azabridge (purple) N atoms.

coworkers [9].

4.1.2 NEXAFS

The NEXAFS data for the N K-edge of a clean $LuPc_2$ thin film deposited on Au(111) are shown in Figure 4.4. The ionization threshold is the step in the absorption at 405 eV evidenced by the vertical line, best seen in the in-plane polarization. Below that threshold the π* resonances are present, which are relative to transitions N 1s $\rightarrow$ π*. They are composed by four different transitions at 398 eV, 400 eV, 403 eV and 404 eV, with the last two almost disappearing in the in-plane polarization. Above the threshold the σ* resonances, relative to transitions N 1s $\rightarrow$ σ*, are composed by a transition at 407 eV, which almost disappears in the out of plane geometry, and a broad transition around 409 eV. The position with respect to the ionization potential is due to 1s orbital that relaxes towards higher energies after ionization, and the π orbitals shifted towards lower energies is due to the increased Coulomb interaction with the nucleus. This explains why the transition to the formally antibonding π* orbitals are located below the ionization potential. The energy of the σ* transition instead is strongly dependent on the bond distance and on the size of the two atoms forming the bond [132]; it is possible to approximate that it falls above the ionization

potential if the sum of the atomic numbers of the two atoms forming the bond is above 15. The NEXAFS spectra on this specific molecule has been simulated by Bidermane et al. [10] by means of DFT calculation. They concluded that in the in-plane polarization the first two π* resonances at 398 eV and 400 eV are mostly due to the azabridge and to the pyrrolic nitrogen respectively, as shown by the different colouring in Figure 4.4. In the out of plane polarization instead, the two contributions are mixed and impossible to be separated. A strong dichroism is present: π* resonances are seen most intense in the out of plane polarization while the σ* are most intense in the in-plane polarization. This can be interpreted by remembering that the NEXAFS cross section depends on the angle between the electric field polarization and the linear momentum of the electron in the final state (i.e. the internal product $\mathbf{E}\cdot\mathbf{p}$), and that the π* orbitals are mostly perpendicular to the molecular plane while the σ* are mostly in-plane. From what stated before we can infer that the molecules lie flat on the surface. Still it has to be pointed out that the π* resonances are not suppressed for the in-plane polarization, and the σ* are also present in the out of plane polarization. This was explained by Bidermane and coworkers [10] who simulated the NEXAFS spectra and found a similar result. They assign it to the non-planar geometry of the molecule, rather than to a non-planar geometry of the film. These results confirm what was measured by XRD and by STM, who show that the molecules lie flat on the surface.

4.2 Reactivity Towards Oxygen

The reactivity of the molecular thin films towards oxygen has been tested by means of different spectroscopic techniques and in a variety of pressure conditions, ranging from UHV to NAP, to ambient pressure, and temperatures ranging from liquid nitrogen to room temperature. The gas-sensing devices based on a $LuPc_2$ or on Pcs in general are known to work by gases permeation in the film, which leads to the creation of deep trap states that block charges and reduce conductivity [113]. It has to be pointed out, however, that most of the samples used for this kind of devices was prepared with the Langmuir-Blodgett method, which is a way faster deposition method respect to the thermal evaporation used to prepare thicker films. Most likely there are not as well ordered as the ones prepared by thermal evaporation. Passard and coworkers [113] studied the oxidation behaviour of $LuPc_2$ molecular films when exposed to strongly oxidizing gas (namely NO_2 and Br_2). They showed a drastic decrease in the conductivity which they ascribed to the reduction of available sites for the hopping process, and the creation of deep trap states. Further details of the eventual reactivity of the molecules upon oxygen are missing.

The reactivity of the molecules upon exposition to oxygen was studied in different regimes. We first investigated the reactivity to a "high" dose of oxygen and water separately by means of Near Ambient Pressure (NAP-) XPS. This was performed at the SPECIES beamline at MaxLab on a $LuPc_2$ film a few nm thick deposited on

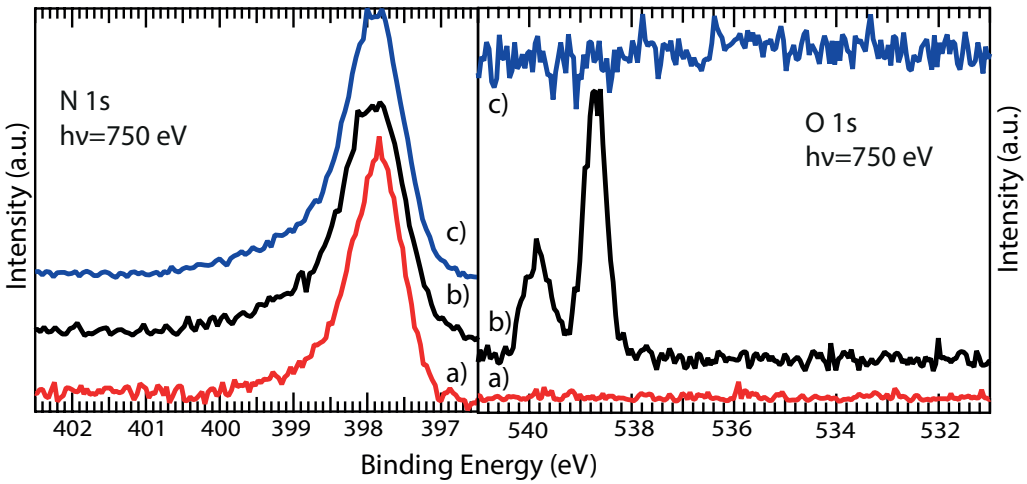

FIGURE 4.5: XPS spectra of the N 1s peak of $LuPc_2$/Au(111) during and after exposure to water (left) and oxygen (right) in the Near Ambient Pressure regime. a)pristine $LuPc_2$ film, b) during oxgygen dose, c) after oxygen has been pumped out.

Au(111). The results are shown in Figure 4.5. The gaseous oxygen peak was indeed present in the measurement during the dose, but after evacuation of the chamber no peak was left, as shown from Figure 4.5. Notably Oxygen region is composed by two peaks due to the multiplet interaction. Moreover no changes were seen in the N 1s and C 1s and Lu 4f peaks during or after the dose (only nitrogen is shown). Only a rigid shift of 0.2 eV is seen, which is probably due to the surface potential, which is different for a molecular layer in contact with vacuum and in contact with (near) ambient pressure gases. This leads to two possible explanations for the working principle of the gas-sensing devices. First hypothesis the oxygen that was able to penetrate through the porosity of the organic layer was also able to escape when pumped. This means that the process is fully reversible of in UHV, or at least below the detection range of a typical XPS measurement, i.e. below 1% atomic density at the surface. Another hypothesis is that even the (relatively) high pressure allowed in a NAP-XPS experiment (tens of mbar) was not sufficient to completely bridge the so-called "pressure gap", which is the assumed difference between a typical surface science experiment that takes place under UHV and the real conditions in which a material will operate. This represents the difficulty but also the necessity of translating the typical surface science experiments to devices operating in real conditions.

To increase the sticking coefficient we tried to expose to pure oxygen at low temperature. The experiment was performed on the D1011 beamline at Max Lab. The sample was prepared by thermal deposition of $LuPc_2$ on a freshly cleaned, herringbone reconstructed Au(111). It was cooled down to $\sim$90 K in a cryostat filled with liquid nitrogen. Temperature was read on a thermocouple placed on the back of the sample. The results of the exposition to different oxygen doses are shown in Figure 4.6. The first evidence is the uptake of oxygen, as demonstrated by the XPS peak of O 1s. This means that the oxygen sticking coefficient becomes non-negligible at

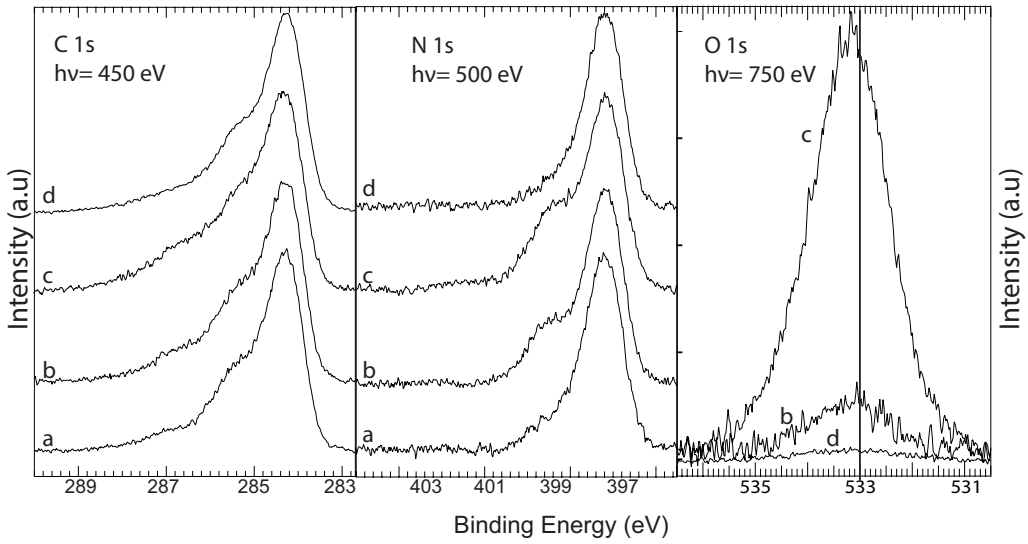

FIGURE 4.6: XPS spectra of $LuPc_2$/Au(111). C 1s (left) and N 1s (centre) and O 1s (right) before (a) after 3600 L (b) after 90000 L (c) of oxygen at 88 K, and after heating up (d) at room temperature.

this temperature. Looking at the C 1s and N 1s spectra the insurgence of a shoulder at higher binding energy is seen after the first dose (3600 L, 1 L = 1×10^{-6} tor $\times$ 1 s), which grows with increased dose. After heating up to RT oxygen is removed, and the two spectra of C and N 1s are perfectly superimposable to the ones relative to the as prepared sample, showing the reversibility of the adsorption process. It is important to note that the O 1s peak after the first dose is asymmetric, with a tail at higher BE, while after the second dose it is shifted at higher BE, as evidenced by the vertical line in the figure. The resolution of the single components did not give any conclusive result due to the wide and varied amount of reference available in literature, with FWHM variable between 0.5 eV and 1.8 eV for similar systems. In principle it is possible to say that at least two components are present, one at lower BE, most visible after the first dose, which is relative to oxygen molecules adsorbed directly on the molecular layer, and a second one, at higher BE due to multilayer oxygen, which drastically increase after the second oxygen dose.

Further information on the oxygen adsorption can be obtained from the analysis of the XPS C 1s and N 1s spectra. The fitting results for the C 1s and the N 1s are shown in Figure 4.7 (1) and (2) respectively, and summarized in table 4.3 and 4.4. We already discussed the results on the clean sample. Here the fitting parameters have been kept constant from the ones used for the clean molecule 4.1, only adjusted due to the different resolution obtained on this beamline. Also the difference between the first peak (composed mostly by benzenic carbons) and the second one (due to the shake-up and the pyrrolic carbon) is not resolved due to beam damage. This has been taken into account by an asymmetry in the peaks of the two carbons.
After the oxygen dose in both C 1s and N 1s spectra a new component is found, at 286.5 eV and 399.6 eV respectively. Interestingly the component on the C 1s spectrum is less intense than the one on the N 1 spectrum respect to the first peak (all the

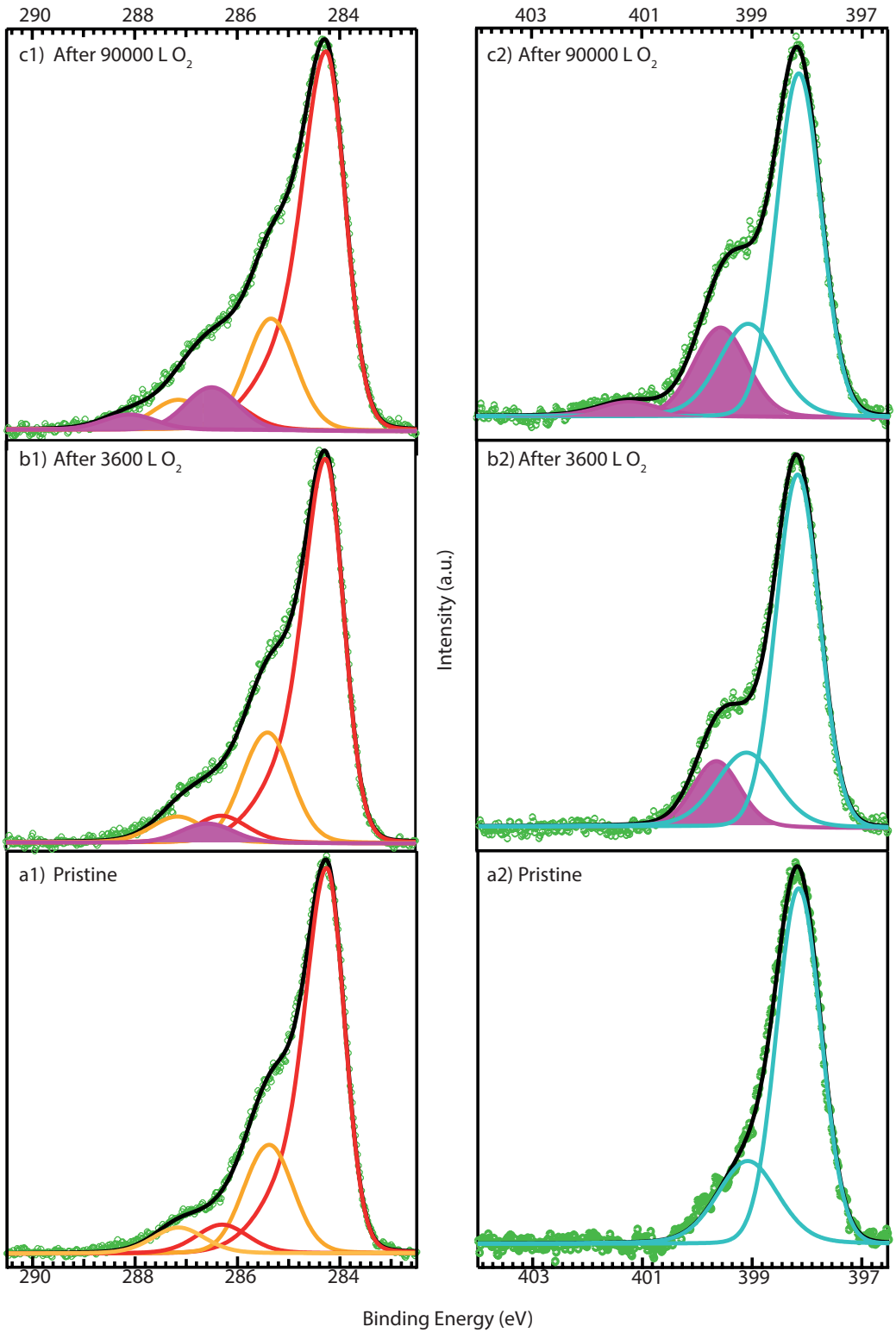

FIGURE 4.7: Fitting results on the C 1s (left) and N 1s (right) peak for the clean $LuPc_2$ / Au(111) film (a), after 3600 L (b) and after 90000 L (c) O_2 at 88 K.

TABLE 4.3: Peak fitting parameters of the N 1s spectra including BE, Area (normalized on the first peak) and FWHM.

Peak	Position (eV)	FWHM (eV)	Area
Clean			
N 1s	398.15	0.95	0.93
N $1s_{sh\text{-}up}$	399.08	1.30	0.32
After 3600 L O_2			
N 1s	398.15	0.95	0.93
N $1s_{sh\text{-}up}$	399.08	1.30	0.29
Additional 1	399.65	1.01	0.19
After 90000 L O_2			
N 1s	398.15	0.95	0.91
N $1s_{sh\text{-}up}$	399.07	1.30	0.35
Additional 1	399.57	1.10	0.29
Additional 2	401.23	1.30	0.06

TABLE 4.4: Peak fitting parameters of the N 1s spectra including BE, Area (normalized on the first peak) and FWHM.

Peak	Position (eV)	FWHM (eV)	Area
As deposited			
C_{benz}	284.26	0.82	1.33
$C_{benz/sh-up}$	286.30	1.20	0.10
C_{pyrr}	285.38	1.10	0.35
$C_{pyr/sh-up}$	287.15	1.20	0.09
After 3600 L O_2			
C_{benz}	284.26	0.84	1.36
$C_{benz/sh-up}$	286.30	1.20	0.09
C_{pyrr}	285.39	1.10	0.35
$C_{pyr/sh-up}$	287.15	1.20	0.09
Additional 1	286.57	1.20	0.06
After 90000 L O_2			
C_{benz}	284.27	0.89	1.44
$C_{benz/sh-up}$	286.30	1.20	0.11
C_{pyrr}	285.34	1.13	0.35
$C_{pyr/sh-up}$	287.15	1.2	0.10
Additional 1	286.50	1.2	0.14
Additional 2	288.1	1.2	0.05

fittings have been performed on spectra that were normalized on the height of the most intense peak). After the second dose both the components increase in intensity, and in both spectra a second additional component is found, at 401.23 eV in the N 1s spectrum and at 288.1 eV in the C 1s spectrum.

The first additional component is referred to C (N) atoms that are close to the adsorption site of the oxygen molecule. In the case of the additional component in the N 1s spectrum the BE is too low to be associated with a C atom bound to an oxygen:

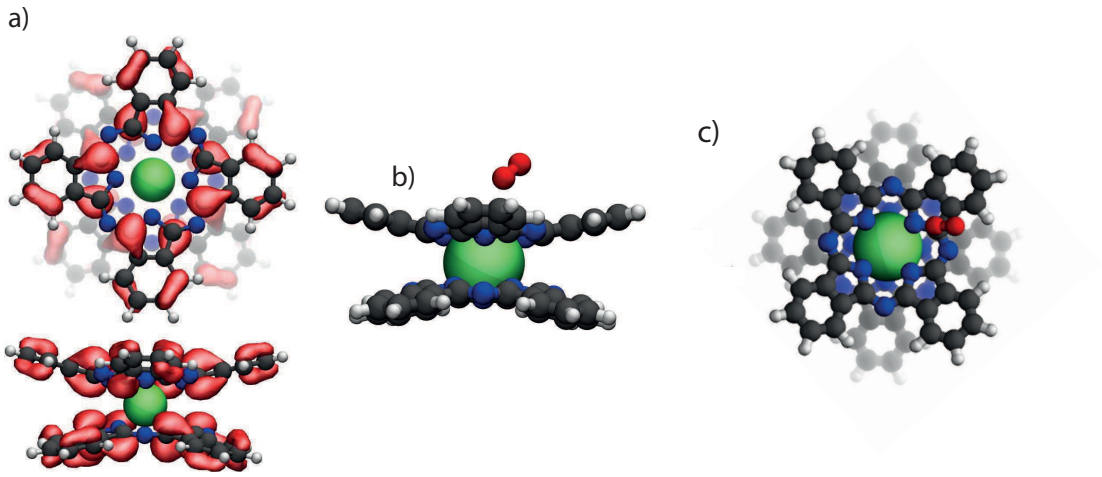

FIGURE 4.8: Molecular orbitals of $LuPc_2$ as calculated by DFT (taken from ref. [10](a)); Geometry of oxygen absorption on isolated $LuPc_2$ molecule as calculated by DFT seen from side (b) and top (c).

the N-O bond is usually found at around 401 eV [6]. In this case the component can be related to N atoms close to a carbonyl group, as in acrylamide [7] or in peptides [27] or in some diamine [82]. In the case of the additional component found in the C 1s peak a direct C-O bond is found at similar binding energies [129, 126] in polymers or small molecules. But in both cases no literature is present on similar systems. This seems to point towards the adsorption of oxygen on top of one of the carbon atoms. The intensity ratio acquired from the fit did not allow any additional conclusive result.

The chemical environment of the Lu atom has been investigated as well. The most prominent peaks are the $4f$, found at 9.5 eV, which shows no changes (not shown). This was expected as the f electrons are close to the nucleus and therefore not reactive. The 3d and 4d peaks have been analysed as well, but again no variations could be evidenced (not shown). This is consistent with the results from the calculation that Orti and coworkers [107] performed by DFT and that Rousseau[120] performed by extended Hükel method who both showed how the Lu does not have any role in the formation of the frontier orbital of $LuPc_2$. This was confirmed more recently by the work of Bidermane et al. [10].

DFT calculations were made by J. Lüder and coworkers at the Uppsala University (Sweden) on the interaction between the oxygen molecule and an isolated $LuPc_2$. They showed that the oxygen molecule adsorbs on top of one of the pyrrolic carbons, as reported in Figure 4.8b),c). This is consistent with the calculation by Bidermane et al. [10] shown in Figure 4.8a), who evidenced the higher charge density for the homo state to be located on the pyrrolic carbon, and with all the known reactivity for organic heterocycles such as isolated pyrrole, which is known to have most of its charge density on the α carbon. This charge density is, of course, what drives the absorption site for an electrophilic molecule as oxygen.

From the analysis of the XPS data, coupled with DFT calculations we can infer that

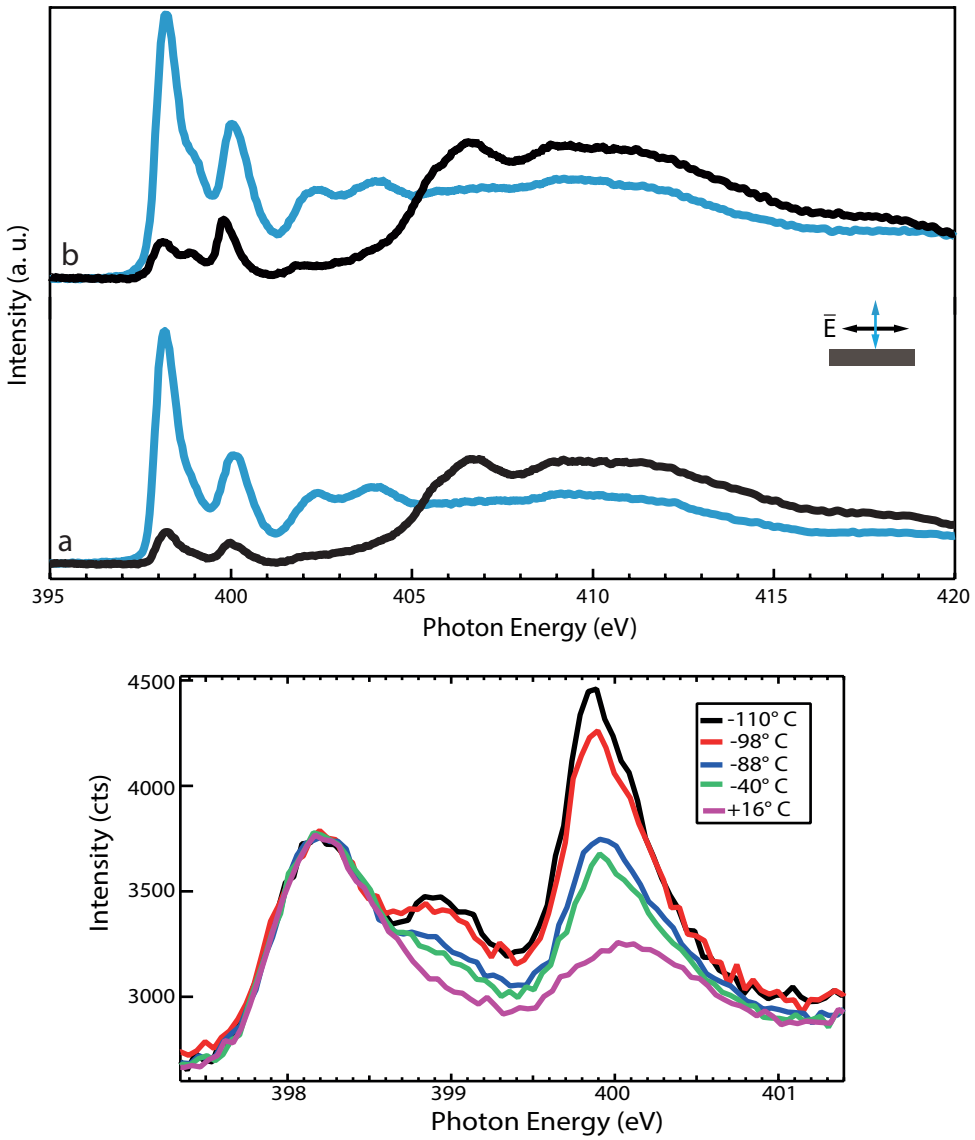

FIGURE 4.9: NEXAFS spectra of $LuPc_2$/Au(111) on the N K-edge before (a), and after 90000 L (b) (top) of oxygen at 88 K; serie of NEXAFS spectra taken during the desorption process (bottom).

the oxygen mostly adsorbs on top of the pyrrolic carbon. However the formation of a chemical bond between the C atom and the O_2 molecule is ruled out due to the low binding energy of the additional peaks and to the low desorption temperature.

The NEXAFS spectrum is shown in Figure 4.9 top. After oxygen exposition three effects are evident on the spectra: first the dichroism is maintained, meaning that the oxygen dose and the possible oxygen permeation do not influence the molecular orientation or molecular geometry. Second the intensity of the second π^* resonance increases after the first dose, and increases further after the second, up to an inversion with respect to the first resonance. Also a third resonance appears at 399 eV as a shoulder after the first dose, and is resolved as a separated peak after the second dose. No changes are seen in the region of the σ^* resonances. The desorption process

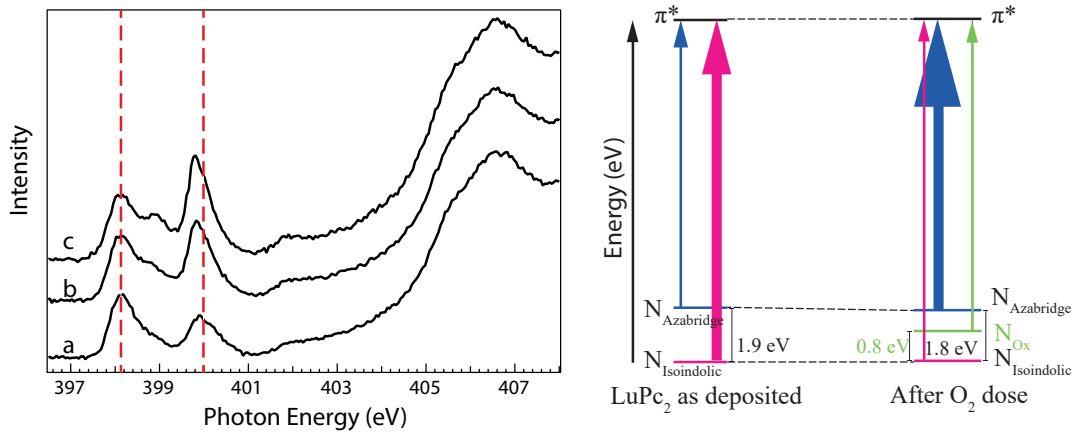

FIGURE 4.10: Zoom on the π* transitions for the pristine $LuPc_2$ molecule a), after a 3600 L oxygen dose b) and after a 90000 L dose c)(left); the energy levels involved in the π* transitions, the arrow size is proportional to the transition intensity (right).

was roughly followed via NEXAFS on N K-edge, taking spectra at defined temperatures. The results are shown in Figure 4.9 bottom. The two parameters used to follow the desorption are the relative intensities of the first two π* resonances and the disappearance of the additional resonance. It is evident that already at -88°C oxygen is desorbed from the molecule. This is a strong evidence for a weak physisorption, and a weak bond between the adsorbate and the molecule. This confirms the XPS results that no chemical bond is formed between the phthalocyanine and the O_2 molecule.

In figure 4.10 left a zoom on the π* transition is shown. From here it is apparent that the variation in the relative intensity of the two transitions is related to the oxygen dose, as it starts already from the first dose, and increases drastically after the second dose. The same can be argued for the additional component. The nature of this component is tentatively explained in Figure 4.10 right and assigned to a new π* transition. After oxygen absorption the degeneracy between the four pyrrolic N is lifted, leading to the one which is closest to the oxygen molecule and more strongly influenced, and in particular charge depleted. This leads to a new transition $N_{ox} \rightarrow \pi$* which is shifted by 0.8 eV from the first transition. It has to be pointed out that in the XPS measurement the ΔBE between the peak relative to the unreacted specie and the new component found was 1.4 eV. This discrepancy can be explained with the different screening modes in XPS and NEXAFS: in the first one

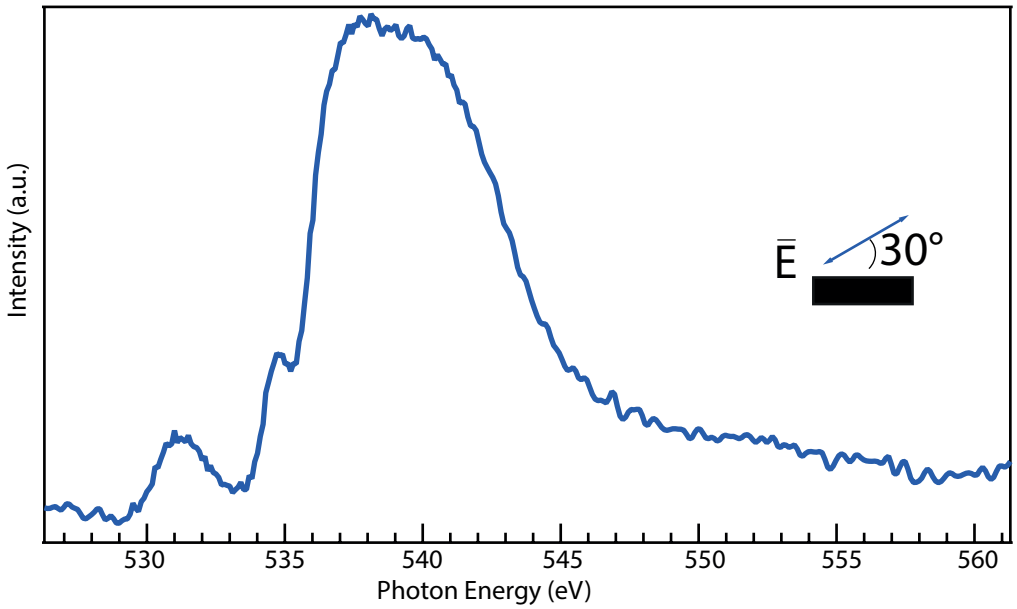

FIGURE 4.11: NEXAFS spectrum of $LuPc_2$/Au(111) at the O K-edge taken after exposition to 90000 L O_2 at 88 K.

the electron is ejected from the molecule, while in the latter it is promoted but not removed, therefore still providing some screening to the core hole, and leaving the final state in a less energetic configuration [132]. The variation in the intensity ratio between the first and the second π* resonance is seen only in the in-plane polarization. This, coupled with the absence of effects on the C K-edge spectrum (not shown) is a proof that the variation is not to be ascribed to a further doming of the molecule, as this would also have effects on spectra taken with the perpendicular polarization and on the C spectra as well. Instead as the contribution of the two different N atoms (pyrrolic and azabridge) is separated only in the inplane polarization the increased intensity is thought as a charge depletion from the azabridge nitrogen (the NEXAFS cross section is proportional to the density of empty states for the final orbital).

In Fig.4.11 NEXAFS spectrum of oxygen collected with a polarization angle of 30° with respect to the surface sample is shown. It is composed by two π* resonances at 531.2 eV and at 535 eV and a larger σ* transition at 539 eV. The first important information to be extracted from this spectrum is that the possibility of adsorbing residual water on the molecule can be ruled out. The fact itself was unlikely due to the careful purification of the gas line used to dose oxygen in the chamber by baking and repeated purging with O_2. Also low residual vapour pressure in the chamber (in the 10^{-10}mbar regime), and mostly due to hydrogen would not allow a large quantity of water to adsorb on the surface on the timescale of the experiment and the water formation reaction $H_2+\frac{1}{2}O_2=H_2O$ is unfavourable at such low temperature and without a catalyst [37], but the absence of the characteristic feature of H_2O in the spectrum is the definitive proof. It has to be noted that the first peak might be due to σ* resonances from different oxygen atoms, as its FWHM is larger than the one reported in literature for sorbed oxygen [132, 115], and π* resonances do not

shift of more than 1 eV from chemi- to physisorbed phases. The σ* resonance instead has been well studied for single and multilayer O_2 on Pt(111) by Stöhr [132]. It was found that oxygen chemisorbed on Pt(111) gives rise to a π* resonance at 535 eV, while physisorbed oxygen was found at 539.2 eV and the multilayer at 540.1 eV. Moreover they showed that multilayer oxygen tends to adsorb with the molecular axis inclined of 15° respect to the surface, this means that in the chosen geometry, the π* resonance due to the multilayer is evidenced. This, as well as the data that shows oxygen dissociation to begin at 150 K on Pt(111) [37] confirm the hypothesis that the reactive specie was O_2, not O_3 or atomic O. Also it corroborates the hypothesis of oxygen physisorption on $LuPc_2$ at low temperature. On Pt(111) it was found that the chemisorbed phase can transform in the physisorbed upon heating at 150 K which is not the case on the molecular layer. This again shows the weakness of the $LuPc_2$-O_2 interaction.
The charge transfer towards oxygen is apparent from the shift towards lower PE of the σ* resonance by 3.8 eV. This shift can be associated to a lengthening of the bond distance between the two oxygen atoms (from 1.21 ± 0.05 Å to 1.39 ± 0.05 Å) which is due to the charge donation to an antibonding orbital, et therefore a reduction of the bond order (calculated as:

$$\left[\frac{\#\text{of electrons in bonding orbitals} - \#\text{of electrons in antibonding orbitals}}{2}\right]$$

From all the set of experiments carried out on oxygen exposure, we can say that molecular oxygen adsorbs on $LuPc_2$ at low temperature with a weak physisorption, and the process being reversible by heating up to RT. Combined XPS and NEXAFS inform that the molecule is found to absorb on top of the pyrrolic carbon, where the highest SOMO density is located. A charge transfer is seen towards the oxygen molecule which mostly influences the LUMO states located on the pyrrolic nitrogens, but do not alter the molecular structure.

4.3 Reactivity Towards Water

The reactivity of $LuPc_2$ thin films towards water in close to operando conditions have been tested at the SPECIES NAP-XPS beamline in Max-Lab. The thin film ($\pm$3 nm) has been exposed to pure water at 1 mbar at room temperature. The results are shown in Figure 4.12. No residual oxygen peak has been detected by XPS and NEXAFS after pumping out the water, testifying once more to the low reactivity of the molecules. The only change is a rigid shift of 0.2 eV of all the core levels during water exposition. The shift is reversible as the initial BE is restored after pumping out the gas. This has been assigned to a surface potential effect, which is different for a molecular film/vacuum interface and a molecular film/water interface. Exposing to water at low temperature (T=-114°C) instead led to water condensation

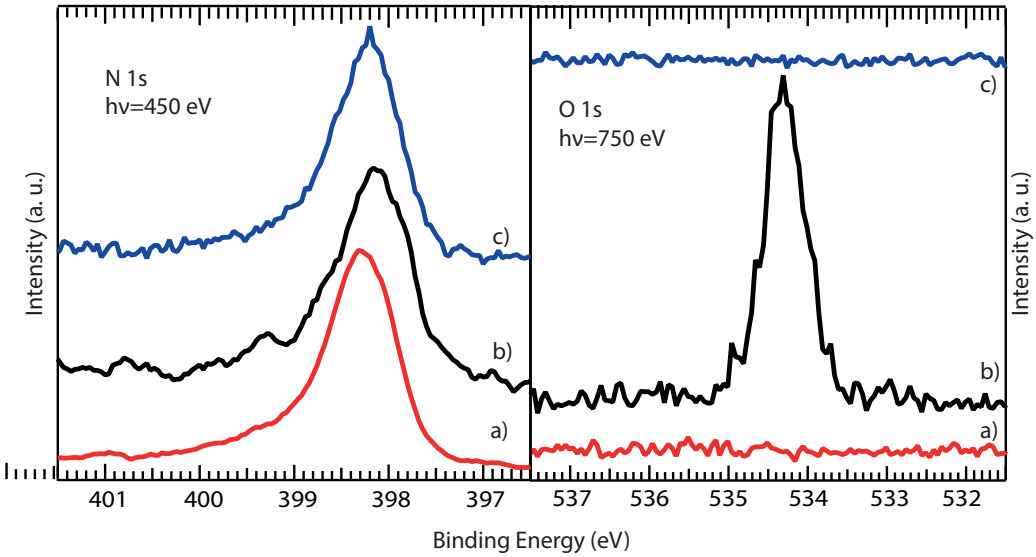

FIGURE 4.12: XPS spectra of $LuPc_2$/Au(111) exposed to water. The N 1s (right) and O 1s (right) before (a), are shown during and after the H_2O exposure.

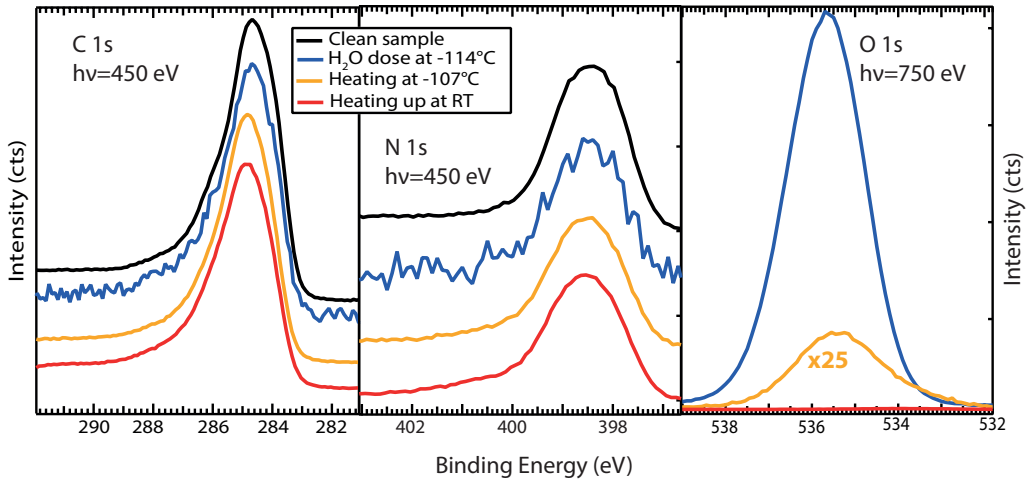

FIGURE 4.13: XPS spectra of $LuPc_2$/Au(111) exposed to water. The C 1s (a) N 1s (b) and O 1s (c) are presented before and after the exposition to water at T=100 K.

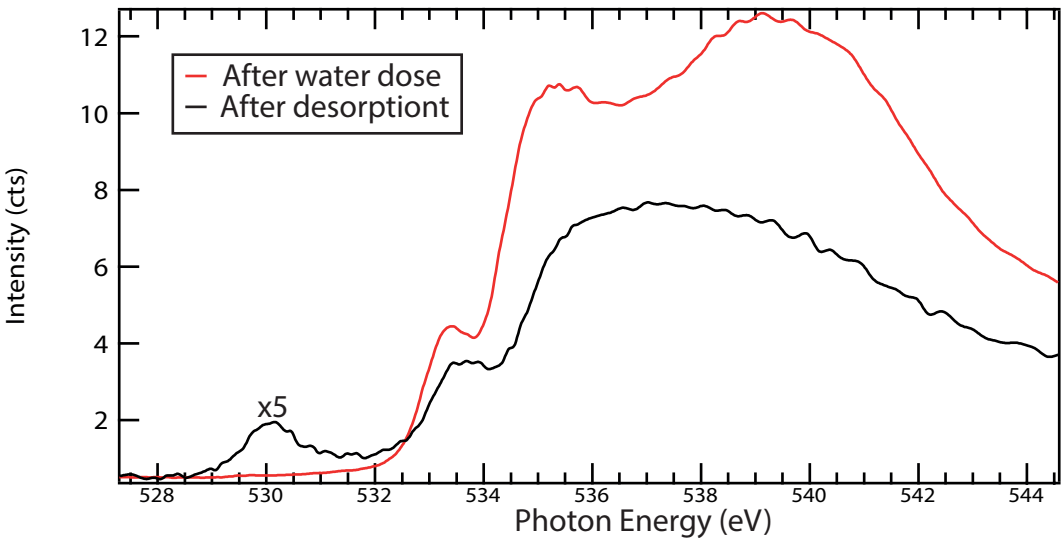

FIGURE 4.14: NEXAFS spectra of the O K-edge after the dose and after desorption.

and adsorption on the surface, as shown by the presence of the O 1s peak in the XPS spectrum (see Figure 4.13c). However this did not modify the C 1s and N 1s XPS (Figure 4.13a;b)) or NEXAFS spectra (not shown). The desorption has been followed by XPS as shown by the progression of the spectra in Figure 4.13. Note that the oxygen 1s peak was not calibrated in BE due to a lack of linearity of the retarding lenses in the XPS analyser, that makes it impossible to calibrate two peaks that are far apart from one another. It is possible to see from Figure 4.14b that the oxygen peak after the desorption is asymmetric. We ascribe this to the presence of two different components: the higher binding energy one has been assigned to the residual water multilayer (which was found to be at 531 eV by Ogasawara and coworkers [106] while the lower BE one was assigned to water adsorbed on the molecular layer. The adsorption of water on the molecular layer is likely to cause a charge transfer from the organic layer to the adsorbate molecules, which is clearly seen on the oxygen peak. It is, however, probably too small to be seen on the core levels of the elements in the organic layer due to the low resolution (nominally between 0.03 eV and 0.16 eV, probably lower due to the high pass energy). A further indication can be obtained by the NEXAFS on the O K-edge shown in Figure 4.14. Right after the adsorption three strong features are seen at 535 eV, 537 eV and 542 eV. The water NEXAFS spectrum is usually analysed in terms of three regions: the pre-edge region centred at 535 eV caused by broken or weakened H bonds, the edge region centred at 537 eV linked with the presence of interstitial water molecules, and a post-edge region starting from 541 eV which is usually associated with ice formation[52]. After the second desorption, however, the ice multilayer is almost completely removed, but a component arises that was buried below the pre-edge. As discussed before this might arise from a strong H bond acceptance. This is indeed possible, as the phthalocyanine molecules are indeed H rich in the benzene area, and in general electron rich due to the π conjugated system. Nevertheless due to the combination geometry of

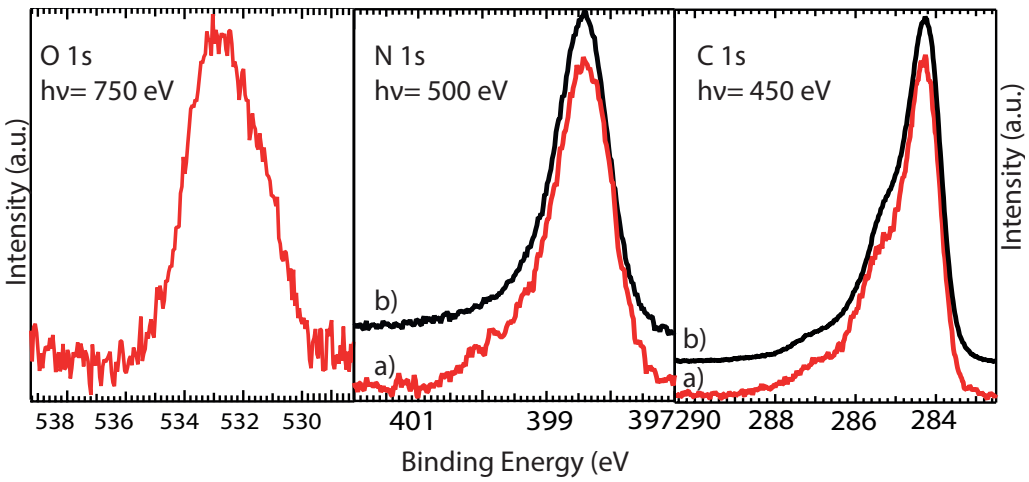

FIGURE 4.15: XPS spectra of the sample after exposition to air. O 1s (left); C 1s (centre); N 1s (right) after exposition to air (a); pristine sample (b).

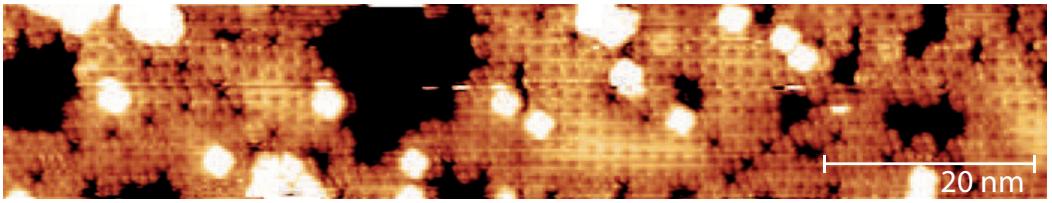

FIGURE 4.16: STM image of the $LuPc_2$/Au(111) sample after exposition to air and annealed to 280°C; V=-3 V; I=300 pA.

the frontier orbitals the unoccupied states are particularly sensitive to "donated" H bonds [52], and, moreover, a donated H bond sufficiently strong to provoke a shift of 2 eV is unlikely not to have caused any change in the N 1s and C 1s chemical environment. Instead component was signalled as belonging to O_2 in the gas phase [111], or to H_2O again in the vapour phase [125]. This is probably due to the proximity to the desorption temperature, which led to a sufficiently high vapour pressure in the proximity of the sample.
In conclusion, we can say that water does not stick on the sample at room temperature, while it does at low temperature. However the influence on the electronic structure of the molecular film is low, with a small charge transfer from the molecular film to the water molecule which does not influence the core electron of the molecule. However, at relatively high pressure the water atmosphere on top of the sample can generate a surface potential, which leads to a rigid shift in the energy levels, which has to be taken into account when designing devices.

4.4 Reactivity Towards Air

An analysis of the effect of air exposition has been carried out. The clean sample has been taken out from the vacuum chamber and analysed after a few days of air exposition. The spectra after reinsertion in the vacuum chamber are shown in Figure 4.15,

compared to the one for the clean sample. There is a visible variation in the shape of the C 1s spectrum, while no changes are seen on the N 1s. It is important to note the difference between the shape of this C 1s spectrum and the one obtained after oxygen adsorption at low temperature. Both present an additional component, but in the case of the sample exposed to oxygen at low temperature it is found at higher binding energy, while in this case the binding energy is 285 eV, which has often been reported as due to amorphous carbon contamination [39]. Nonetheless oxygen is present on the sample, as demonstrated by the O 1s peak. This probably means that the oxygen atoms have penetrated in the pore of the layer. This is known to be one of the most important factors in reduction of the conductivity in organic thin films due to the creation of deep trap states [113] (see section on degradation). However an annealing to 250$\pm$25°C for 10 minutes is enough to remove all the contaminants (while leaving the sample thickness unchanged, as measured from the ratio between the Au $4f$ and C 1s peaks). Also after this kind of treatment the surface was almost perfectly restored, as shown from the STM image shown in Figure 4.16. Still it was not possible to stabilize the tip on the sample, even after several days of working, meaning that probably a form of mobile contamination is still present on the surface of the sample.
In conclusion, these molecules present little to no reactivity when exposed to the atmosphere, or at least the process is reversible in UHV after a short annealing. Also it has to be remembered that XRD was performed on samples exposed to air for some days, and no drastic changes were seen on the expected structure.

4.5 Reactivity of $LuPc_2$/Si(100)

The effect of the substrate has been tested by studying the reactivity of a molecular film deposited on 2×1-Si(100). The adsorption of the molecules on Si(100) has recently been studied by Bidermane and coworkers [9]. They showed a strong interaction between the substrate and the overlayer bends the underlying phthalocyanine ring to form Si-$C_{benzenic}$ weak bonds. By using a reactive substrate instead of the unreactive Au(111) surface, the permeation of gases through the molecular layer and the reactivity of the buried interface can be studied. This second observation in particular is of great technological interest, as one of the most important degradation factors for organic devices (in particular organic solar cells) is the oxidation of the anode or cathode contacts at the interface with the organic layer. At the moment a strong encapsulation with a protective layer is needed to protect the anode as well as the organic layer from the oxidation, indeed coupling the active layer and the encapsulating layer would be of great interest.
The Si(100) substrate was thoroughly outgassed at 500°C, until the base pressure was recovered, and then flashed at 1050°C in a pressure better than 10^{-9} mbar for 3 times (the temperature was read by a pyrometer). As we already demonstrated the low reactivity of molecular films composed by double-decker phthalocyanine, the

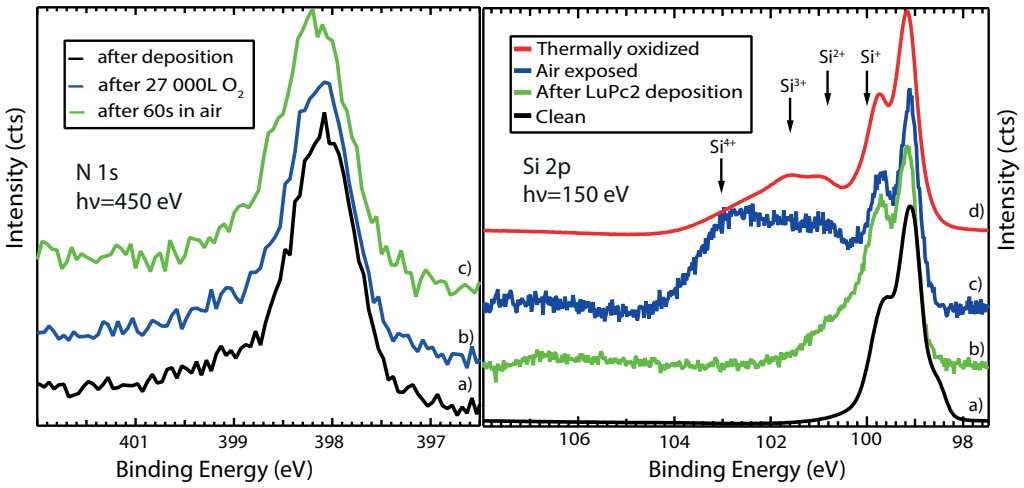

FIGURE 4.17: left: XPS spectra of the N 1s peak as deposited (a), after 27000 L O_2 (b) and after air exposition. right: Si 2p spectrum of the clean sample (a), after $LuPc_2$ deposition (b), after exposition to air (c) and a thermally oxidized sample for comparison (d). References for the Silicon oxides BE are taken from ref.[41].

next step should be to protect the metallic electrode from oxidation. Therefore we deposited a thin film (3±0.3 nm) and investigated the reactivity of the underlying substrate as well as the one of the molecular layer. The film is defined "thick" as the signature of the Si-molecule interaction, i.e. the broadening of the C 1s spectrum and the shift in the N 1s, are not seen, meaning that the largest part of the signal does not come from molecules in contact with the substrate. We exposed the sample to different gas doses and analysed the reactivity of both the organic layer and the interface. The first exposure was to 27000 L of O_2, i.e. 5×10^{-6} for 5400 seconds at room temperature. It has to be remembered that a layer of molecules adsorbed on gold did not show any reactivity at room temperature for a similar or even higher dose. The same stability of the film is found here, as no oxygen peak is evidenced. This is an interesting result, as it means that no oxygen penetrated the molecular layer. Also no components due to oxidized species are present in the Si 2p spectrum.

To further test the efficiency of our protecting layer, the same sample has later been removed from vacuum, exposed to atmosphere for 60 seconds, and then reinserted into the vacuum chamber. The results are shown in Figure 4.17. This time the oxygen peak is indeed present as well as a strong peak due to oxidized silicon in the Si 2p spectrum. The BE position of the different components of Si was assigned following the work by Dreiner et al. [41]. It is possible to see a stronger intensity of the component relative to a Si^{4+}, which is the oxidation state usually found at the interface between the substrate and the oxidizing agent (in this case air) with respect to the components of Si^{1+}, which are found at the interface between SiO_2 and Si due to the higher diffusion coefficient of O with respect to the diffusion coefficient of Si in SiO_2. This tells us that the oxidation of the substrate is mostly limited by the diffusion of oxygen (or water) in the substrate rather than from the diffusion of oxygen in the molecular layer. The N 1s peak instead show no modification; the C

peak is not reliable as it shows different components probably due to carbon present in the atmosphere which is adsorbed on the surface. This is a strong proof that air at room temperature and ambient pressure is able to penetrate in the organic layer and react with the substrate. The reaction can be understood in terms of film morphology. It was shown by Boudet [12, 13] that molecular layers deposited on bare Si(100) grows by clusters, after a first wetting layer. This kind of structure is probably highly porous and allows the penetration of oxygen and water in the layer. Also the wetting layer is probably disordered due to the strong interaction between the molecules and the substrate, as shown later by Bidermane et al. [9] This leads to disordered agglomerates, which leaves the possibility for the surface atoms to react with oxygen even after the formation of the C-Si bond. Moreover this again remembers us the limits of surface science UHV based studies when dealing with real devices, the so-called "pressure gap".

4.6 Conclusion

The reactivity of $LuPc_2$ thin films deposited on noble metal and semiconducting surfaces towards different gases have been investigated. The film itself is remarkably stable, not showing any changes after exposure to "high" partial pressure of water or oxygen. Even after being exposed to air no changes are seen, and the contaminant can be removed with a mild annealing to recover the clean surface.
By cooling down the sample at 90 K instead molecular oxygen is weakly physisorbed on the surface, and able to modify the molecular orbitals of the molecule. The central atom is not reactive, due to the protection from the macrocycle, while reaction takes place on the α carbon. Also at this low temperature water can condense on the surface, but it has been shown to be unreactive.
When deposited on more reactive surfaces, with a different absorption chemistry which leads to a different absorption geometry, the molecules are still unreactive, but unable to protect the substrate from a reaction as it has been shown on Si(100).
The reactivity of $LuPc_2$ thin films have been studied towards different gases and in a variety of conditions. Exposition to gas at room temperature did not show any influence on the molecular layer even at relatively high pressure: both oxygen and water do not stick on the surface and no traces left are seen after pumping the gas from the chamber. The only effect is a change in the surface potential seen in an atmosphere of 1 mbar of pure water, which might be due to the electrostatic difference between the molecule vacuum and the molecule-gas interface. Cooling down the surface indeed increase the sticking coefficient for gases, which condense on the surface. Water, which is usually the most reactive gas in the atmosphere does not react with the molecular layer. Also $LuPc_2$ were proved to be unreactive to air at room pressure, as exposition to air for a few days did not alter the molecular structure, and only deposited a contamination layer that was easily removed by annealing under

UHV making of this kind of double-decker phthalocyanine very robust charge carriers. Instead exposition to air at ambient pressure was able to oxidize the underlying Silicon substrate, showing that the molecular layer is not able to act as a protective layer.
Water condenses on the surface below -114°C, but no effect is seen on the molecular layer. Oxygen instead condenses on the surface below 88 K with a weak physisorption, which is completely reversible after heating up to RT. No chemical bonds are evidenced between molecular oxygen and the molecular layer. Instead a strong charge transfer is present, which drives the adsorption of molecular oxygen on top of the pyrrolic carbon. Nonetheless the core levels of N atoms are most concerned, probably due to an internal charge reorganization which mostly influence the LUMO states, which are localized on the N atoms.

Chapter 5

Conclusions

In this thesis work we showed our progresses on the description of the structure of thin molecular films of double-decker phthalocyanine and their reactivity, or, better, their stability. We studied the structure of the film by a combined local and average approach, by means of STM and different diffraction techniques. The reactivity instead was investigated by means of synchrotron based spectroscopy techniques: HR-XPS and NEXAFS. The objective of this section is to summarize the results we obtained and present them in a clear and concise way, and to give some ideas on how to proceed in the study of the organic/inorganic interfaces.

5.1 Structure of the Thin Film

The structure of double-decker phthalocyanine has been described by means of GIXD. We showed that the molecules when deposited on non-interacting substrate (H terminated Si(100)) create a mostly amorphous film, with small crystallites adopting the γ structure with the molecular axis almost perpendicular with respect to the substrate surface. On slightly more interacting substrate as noble or transition metal surfaces they tend to lie flat adopting at first the α structure which is then transformed in the β after annealing. In both cases the molecules are lying with the molecular plane parallel to the surface. The substrate was demonstrated to have a further influence on the molecular layer. The unit cell of the molecular lattice is aligned on one of the close-packed directions of the Au(111) surface. This is due to the van der Waals interaction between the molecule and the substrate. Also a small charge transfer is present, which leads to a relaxation in the herringbone reconstruction.

The surface morphology was investigated with a local microscopy approach by means of STM. For a film a few nm thick deposited on a sample kept at room temperature the surface is disordered, composed of bubble-like corrugations. It gets more ordered with increasing annealing time and temperature, going from a disordered dispersion of molecules to ordered islands on flat terraces coexisting with little disordered molecules. The terraces are composed by a double layer of molecules, probably due to the high molecule-molecule absorption energy, which leads to a favourable stacking. The molecular out of plane stacking has been shown

to be led by a minimization of the electronic repulsion between the electrons in the highest molecular orbitals. However at least two different configurations have been shown to coexist: one with the two facing phthalocyanine rings (the lower from the molecule on top, and the upper from the underlying molecule) are in the eclipsed position, which is probably favourable due to the geometry of the SOMO. In the second configuration the two macrocycles are in a staggered position. The first configuration seems to be the preferred one. The in-plane stacking has been resolved as well, and the mutual relation between molecules belong to different domains is evidenced. It was shown that the minimization of the interaction can come from the upper or the underlying phthalocyanine ring. The two configurations are not equivalent as the two rings are not rotated of exactly 45°.

5.2 Molecular Reactivity

The reactivity of $LuPc_2$ thin films deposited on noble metals and semiconducting surfaces has been investigated by means of different synchrotron based spectroscopic techniques: XPS and NEXAFS. The molecules present an exceptional stability, not displaying any reactivity at room temperature, when exposed to "high" partial pressure of water or oxygen. In fact no traces of oxygen are evidenced when the gas is pumped out. This means that either no reaction takes place either the reaction is perfectly reversible in UHV. The only variation is a change in the surface potential, due to the difference in the electrostatic processes between the molecule/vacuum and the molecule/gas interface. Even when exposed to air at room temperature and ambient pressure no changes are seen in the molecular electronic structure. Only a contamination from carbonaceous species, most probably absorbed from air is present on the surface, and is easily removed by means of a mild annealing. Instead, when deposited on a reactive semiconducting surface (Si(100)) the substrate is fully oxidized upon exposition to air at ambient pressure, as the molecular layer (a few nm thick) is not able to screen the substrate from the interaction with the gases. However the electronic structure is still preserved.
The molecules, however, did show some degree of reactivity when exposed to gases at low temperature. Water condenses on the surface at -114°C, but no effects are seen on the molecular layer. Oxygen instead condenses on the surface at 88 K with a weak physisorption. The process is completely reversible under UHV when the sample is heated back at room temperature. No chemical bonds are evidenced between the molecular layer and the adsorbed oxygen. Instead a strong charge transfer is present, which drives the adsorption of molecular oxygen on top of the pyrrolic carbon, as expected from DFT calculations and from the known reactivity of the pyrrole. Nonetheless the biggest effect is seen on the LUMO relative to the pyrrolic N atoms, probably due to an internal charge rearrangement after interaction with oxygen, which withdraws charge density from the LUMO, which is mostly localized on the pyrrolic nitrogen atoms. It is important to note that in all the above experiments

no changes have been seen on the Lu $4f$ or 3d or 4d orbitals.

5.3 General Conclusions and Perspectives

From what stated above double decker phthalocyanine present a very low reactivity, and in particular under all the conditions no reactivity is evidenced on the central atom. This is due to the low contribution of the central atom atomic orbitals in the formation of the frontier orbitals of the molecule. Moreover the double decker geometry can act as a protection for the central atom. This is particularly important in the case of molecular magnets, where the magnetic properties mostly come from the central atom, making $REPc_2$ a potential candidate for this kind of applications. However it would be interesting to see if for example adsorption of a paramagnetic molecule as oxygen might lead to a magnetic coupling with the f electrons of the RE cation. It has to be pointed out anyway that, if an application in devices is to be expected easier and cheaper solutions have to be found, as the synthesis is still complex, and RE are expensive. In this direction we would like to point out our contribution showing the low contribution of the central atom in the reactivity of the molecule, allowing for a change towards a less expensive family of Pc_2.

Appendix A

Beam Damage

X-ray and UV light are known to be ionizing radiations, due to the fact that, opposed to Visible light or Infra Red they are able not only to excite transitions in the shined material, but also to excite photoelectrons, i.e. give enough energy to an electron for it to escape from the material. The energy of these electron depends of course on the energy of the incident photon and on the Binding Energy of the excited electron, therefore they can range from a few eV in an Ultraviolet Photoelectron Spectroscopy (UPS) to thousand eV in XRD experiments.
Another important font of damage is of course the direct irradiation with electron beams, as in the case of LEED or Inverse Photoemission Spectroscopy (IPS). Again in this case electron with kinetic energies ranging between 0-200 eV interact with the sample. Interestingly it has been shown that the two phenomena (x-ray illumination and subsequent photoelectron creation, and direct irradiation with electron beams) produce the same kind of damages on thiolate Self Assembled Monolayer [63]. Hollenshead and coworkers [64] however found that the most important mechanism for carbon deposition under irradiation is not the secondary electron absorption, but direct photon absorption.

A.1 Parameters influencing beam damage

Here the most important parameters influencing beam damage are listed.

- **Temperature**: Probably the most important factor leading to beam damage is the local heating of the sample [42]. This is particularly a problem in organic sample, as they have melting points way lower respect to most inorganic materials. In particular it is important to remember that, even if the sample temperature is constant, locally it might be larger, as it depends on the thermal conductivity of the sample, which is low for organic materials. It has to be pointed out however that Leontowich demonstrated how an intense, high energy electron beam was not able to heat a sample more than °C, as measured by the melting point of stearic acid [83], meaning that even the local temperature variation might be low under irradiation. One of the techniques used to

avoid beam damage is cooling the substrate below 0, this reduce atoms mobility on the surface, and therefore the mobility of the radical. Still it was shown that although it can prevent mass loss from the sample due to evaporation of low molecular weight fragments, once the sample is again heated up to room temperature mass is indeed lost. Therefore lowering the temperature is only a temporary solution.

- **Energy**: Leontowich and coworkers [84] studied the beam damage in several different polymers by irradiation with energies above, below and exactly at the C 1s ionization threshold. They found no influence of the beam energy on the damage rate. However they pointed out that many discording studies have been published, on different absorption edges (O, N, C), as this might be very material dependent. Meents and coworkers [97] have demonstrated by means of XRD that under radiations molecular bonds can be lengthened. The increased atom separation might lead to stress that in turns leads to cracks in the organic material. Also the lengthening might be high enough to lead to a straight bond breaking.

- **Direct Radiolysis**: The biggest problem anyway is still the radiolysis. When the electrons are excited the subsequent de-excitation might lead to a broken bond in the molecule. In this case it seems that densely packed molecular layers are more resistent to beam damage due to a larger delocalization and a faster decay of the excited state [53]; Another important process is the H^- ions removal, the C-H bond is particularly prone to be cleaved by photoelectron absorption due to the possibility of resonant excitation of vibrational modes [2]. This might lead to cross linking [157], as is currently employed to prepare negative photoresists [139]. Or instead might lead to the creation of larger ionic molecules (usually $C_xH_y^-$) that might migrate and react [67]. Another important feature is the presence of etheroatoms can lead to to a preferential cleavage of the C-X (where X is not necessarily an halogen, but only a more electronegative atom) [63]. This is directly related to the composition of the volatile components that are removed. Another phenomena caused by beam damage is the polymerization of hydrocarbons presents on the surface. This is mostly seen in sample not prepared in situ but also the presence of fragments coming from the specimen can start the polymerization.

- **Material dependence**: Conjugated compounds have been demonstrated to be less sensitive to beam damage respect to aliphatic ones [104]. This is probably due to the stabilization energy provided by the delocalized electronic shell, which allow to dissipate the energy accumulated due to the scattering events

between more atoms.

- **Substrate**: Interestingly the substrate can have contrasting effect. It is indeed a source of a lot of secondary electrons, but it might also stabilize the overlayer. The excited states generated in the molecules of the overlayer by the photo-electron absorption can be quenched by the image potential generated by the substrate, leding to less beam damage in molecules closer to the interface [136].

A.2 Data

Following here our data on the beam damage on $LuPc_2$ thin films are presented. As

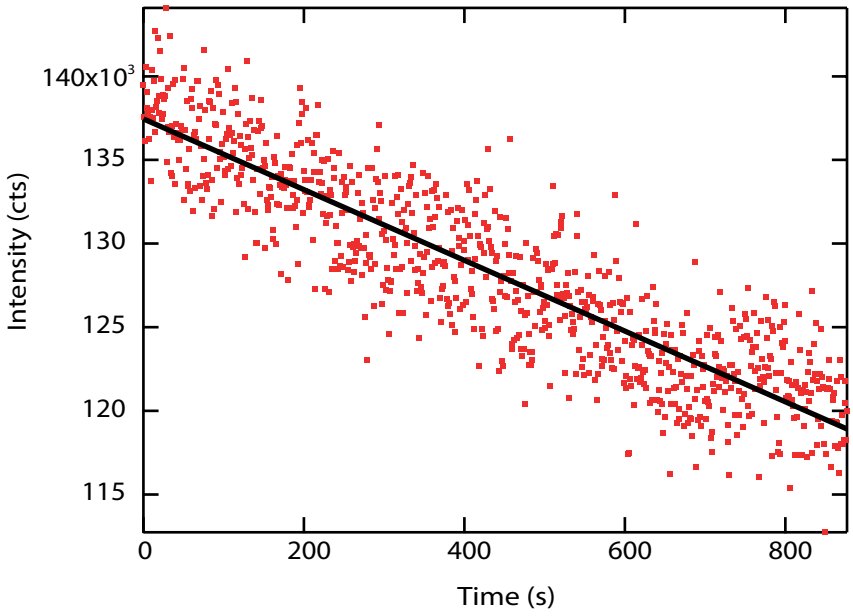

FIGURE A.1: Evolution with time of the diffraction peak relative to the (200) plane of a $\pm$3 nm thick $LuPc_2$ thin film deposited on Au(111), and linear fit of the decrease.

explained it is widely known that x-rays might damage organic layer. In particular we measured the beam damage on a $\pm$ 20nm thick $LuPc_2$ thin film deposited on Au(111) exposed to a 11 keV beam with a flux of 3×10^{12} photons on a 30×30 μm^2. The parameter we monitored was the by the decrease of the diffraction peaks due to the organic layer with time. The results are shown in Fig.A.1 (the signal of the clean gold in the same condition was subtracted as a normalization. The reduction of the intensity is 10% in an hour, but never disappeared. Even after irradiating at higher temperature, up to 300°C the structure peaks were still found.

Under prolonged beam exposition molecular desorption can be observed, as shown from Figure A.2 where the water quantity greatly decreased after half an hour of measurement on the same place. The decrease of the component relative to the σ^*

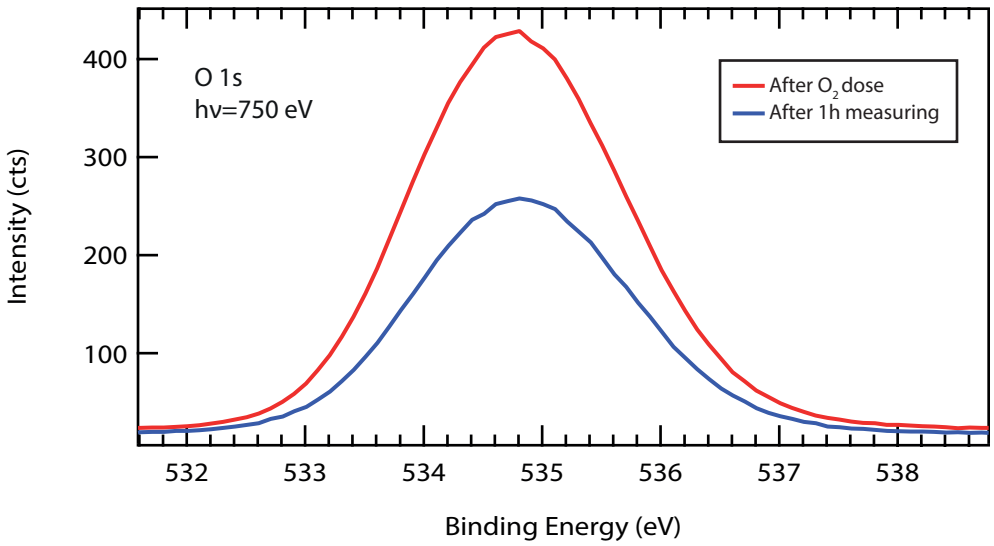

FIGURE A.2: XPS spectrum of a $\pm$3 nm thick $LuPc_2$ thin film deposited on Au(111) after measuring for half an hour (a) and on a fresh spot (b).

transitions of the disordered ice layer is clearly seen. This is most likely due to the local heating due to the beam, which leads to the evaporation of the ice layer deposited on top of the sample. Note that the BE of the spectra in Figure A.2 could not be calibrated due to a lack in linearity of the retarding lenses in the analyser, which causes the KE measured by the analizer to be irreproducible under certain conditions. In Figure A.3 it is possible to see the C 1s spectrum of a $LuPc_2$ sample $\pm$3nm thick deposited on Au/Mica. It is evident from the comparaison between the undamaged spectrum (a) and the damaged spectrum (b) that a loss of resolution is apparent: the first peak in (b) is larger, especially at lower BE. Also the valley at 285 eV which separates the first two peaks in the undamaged spectrum, disappears in the second. This is most likely due to the insurgence of a new component due to amorphous carbon. From the ratio between the first peak (mostly due to the benzenic C) and the second peak (due to the pyrrolic C) it is impossible to tell which part of the molecule was more prone to undergo beam damage. As the N peak (not shown) did show no variations we can argue that it is unlikely that the C-N or Lu-N bonds were broken, and it is possible to speculate that it is the benzene moyeties that broke under the beam. This can be understood by thinking of it as one side chain in polymer molecules, being at the periphery of the molecule it possesses less way to dissipate the energy absorbed under upon irradiation

. In Figure A.4 the C 1s spectrum of a sample after different irradiation doses are shown. It is clear that already in the first spectrum a component at 285 eV is present, that is assigned to amorphous carbon generated by the beam damage. It is interesting to see how after prolonged exposition the intensity of the component varies only slightly, meaning that a plateau in the beam damage is reached.

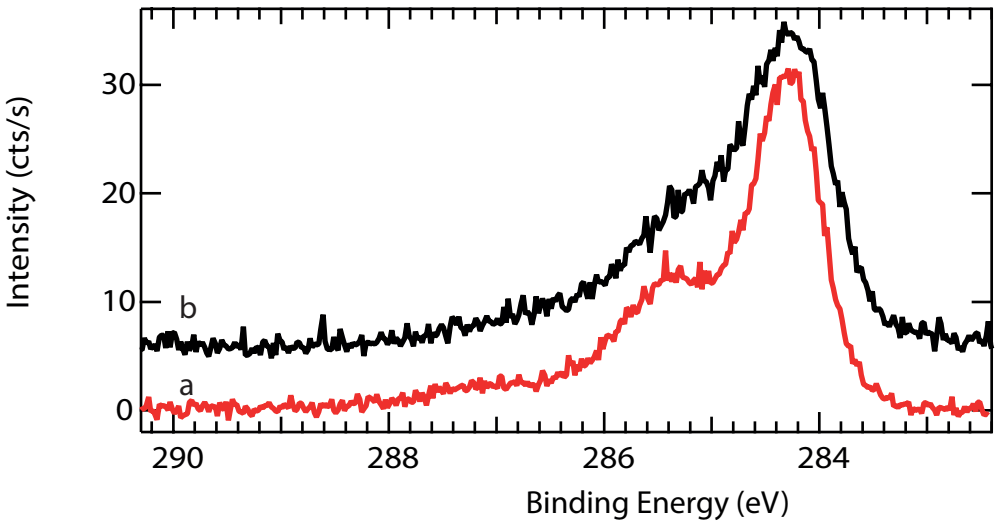

FIGURE A.3: C 1s XPS spectra of a $LuPc_2$ sample $\pm$3nm thick deposited on Au/Mica. The spectra taken moving the sample every 30 seconds (a) and after measuring 4 minutes on the same spot(b).

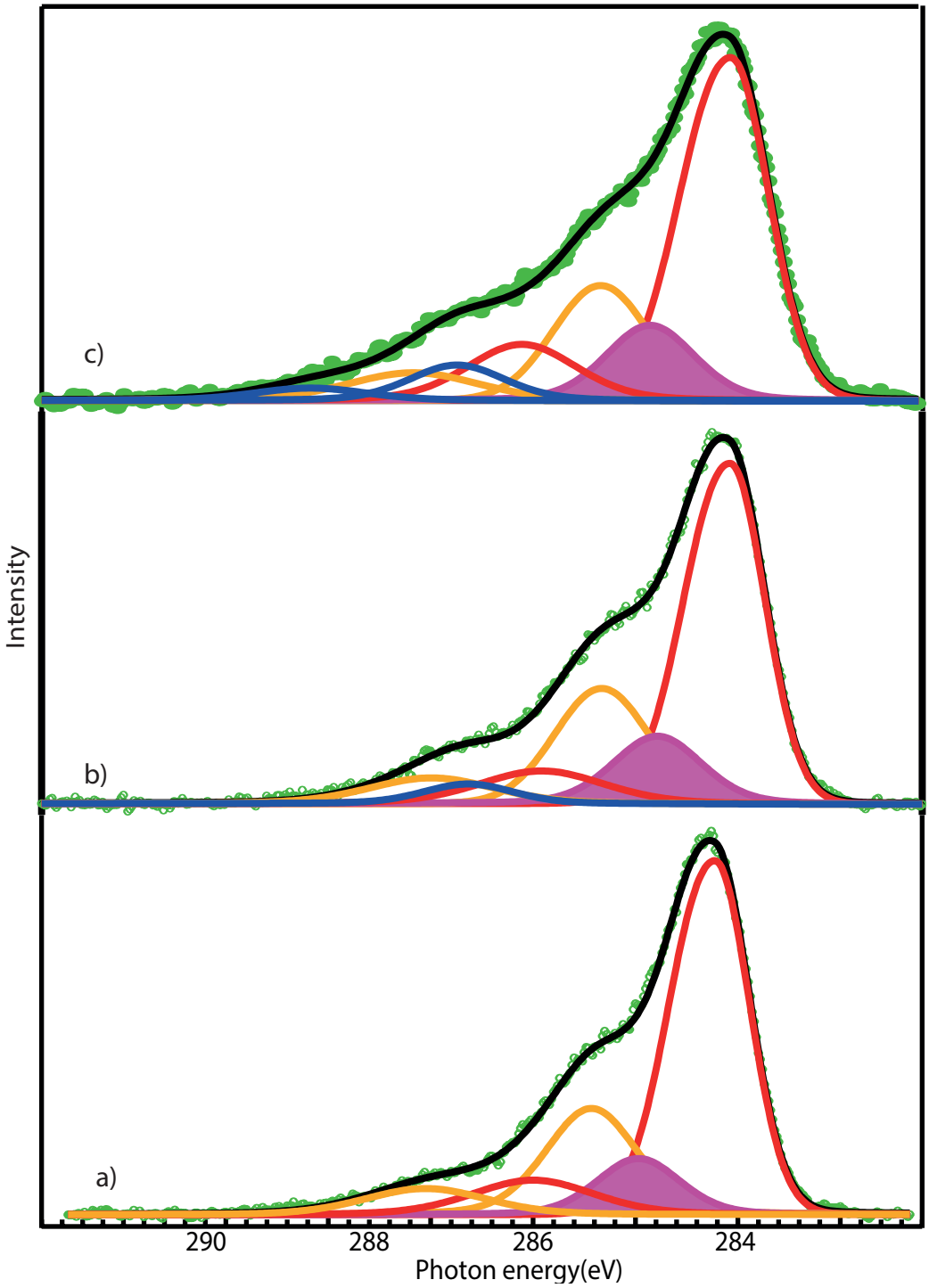

FIGURE A.4: C 1s spectra of a $LuPc_2$ $\pm$1 nm thick sample deposited on Au(111) after 2h irradiation (a), after 5h irradiation (b) and after 10h irradiation (c).

Bibliography

[1] H. Adler, M. Paszkiewicz, J. Uihlein, M. Polek, R. Ovsyannikov, T. V. Basova, T. Chasse, and H. Peisert. Interface properties of vopc on ni(111) and graphene/ni(111): Orientation-dependent charge transfer. *Journal of Physical Chemistry C*, 119(16):8755–8762, 2015.

[2] L. Amiaud, J. Houplin, M. Bourdier, V. Humblot, R. Azria, C. M. Pradier, and A. Lafosse. Low-energy electron induced resonant loss of aromaticity: consequences on cross-linking in terphenylthiol sams. *Physical Chemistry Chemical Physics*, 16(3):1050–1059, 2014.

[3] P. Amsalem, G. Heimel, M. Oehzelt, and N. Koch. The interface electronic properties of organic photovoltaic cells. *Journal of Electron Spectroscopy and Related Phenomena*, 204:177–185, 2015.

[4] M. Ashida, N. Uyeda, and E. Suito. Unit cell metastable-form constants of various phthalocyanines. *Bulletin of the Chemical Society of Japan*, 39(12):2616–+, 1966.

[5] J. V. Barth, H. Brune, G. Ertl, and R. J. Behm. Scanning tunnelling microscopy observations on the reconstructed au(111) surface - atomic structure, long range superstructure, rotational domains, and surface-defects. *Physical Review B*, 42(15):9307–9318, 1990.

[6] C. D. Batich and D. S. Donald. X-ray photoelectron spectroscopy of nitroso compounds - relative ionicity of the closed and open forms. *Journal of the American Chemical Society*, 106(10):2758–2761, 1984.

[7] E. Baumgarten, A. Fiebes, A. Stumpe, F. Ronkel, and J. W. Schultze. Synthesis and characterization of a new platinum supported catalyst based on poly-Acrylamide-co- 3-(Acryloylamino)propyltrimethylammoniumchloride as carrier. *Journal of Molecular Catalysis a-Chemical*, 113(3):469–477, 1996.

[8] I. Bidermane. *Structure and Electronic Properties of Phthalocyanine Films on Metal and Semiconductor Substrates*. Thesis, 2014.

[9] I. Bidermane, J. Luder, S. Ahmadi, C. Grazioli, M. Bouvet, B. Brena, N. Martensson, C. Puglia, and N. Witkowski. When the grafting of double decker phthalocyanines on si(100)-2 x 1 partly affects the molecular electronic structure. *Journal of Physical Chemistry C*, 120(26):14270–14276, 2016.

[10] I. Bidermane, J. Luder, S. Boudet, T. Zhang, S. Ahmadi, C. Grazioli, M. Bouvet, J. Rusz, B. Sanyal, O. Eriksson, B. Brena, C. Puglia, and N. Witkowski. Experimental and theoretical study of electronic structure of lutetium biphthalocyanine. *Journal of Chemical Physics*, 138(23), 2013.

[11] Y. Borensztein and N. Witkowski. Optical response of clean and hydrogen-covered vicinal si(001) 2x1 surfaces. *Journal of Physics-Condensed Matter*, 16(39):S4301–S4311, 2004.

[12] S. Boudet. *Auto-assemblage Moléculaire de Bisphthalocyanines de Lutétium: Organisation, Structure, et Propriétés optiques*. Thesis, 2011.

[13] S. Boudet, I. Bidermane, E. Lacaze, B. Gallas, M. Bouvet, J. Brunet, A. Pauly, Y. Borensztein, and N. Witkowski. Growth mode and self-organization of lupc2 on si(001)-2 x 1 vicinal surfaces: An optical investigation. *Physical Review B*, 86(11), 2012.

[14] M. Bouvet and J. Simon. Electrical-properties of rare-earth bisphthalocyanine and bisnaphthalocyanine complexes. *Chemical Physics Letters*, 172(3-4):299–302, 1990.

[15] D. Braga and G. Horowitz. High-performance organic field-effect transistors. *Advanced Materials*, 21(14-15):1473–1486, 2009.

[16] J. L. Bredas, J. P. Calbert, D. A. da Silva, and J. Cornil. Organic semiconductors: A theoretical characterization of the basic parameters governing charge transport. *Proceedings of the National Academy of Sciences of the United States of America*, 99(9):5804–5809, 2002.

[17] B. Brena, Y. Luo, M. Nyberg, S. Carniato, K. Nilson, Y. Alfredsson, J. Ahlund, N. Martensson, H. Siegbahn, and C. Puglia. Equivalent core-hole time-dependent density functional theory calculations of carbon 1s shake-up states of phthalocyanine. *Physical Review B*, 70(19), 2004.

[18] G. Brown, K. Halbach, J. Harris, and H. Winick. Wiggler and undulator magnets - a review. *Nuclear Instruments & Methods in Physics Research*, 208(1-3):65–77, 1983.

[19] J. Bufler, M. Abraham, M. Bouvet, J. Simon, and W. Gopel. Growth and electronic-properties of ultrathin lutetium-diphthalocyanine films studied by electron-spectroscopy. *Journal of Chemical Physics*, 95(11):8459–8466, 1991.

[20] J. K. Burdett, R. Hoffmann, and R. C. Fay. 8-coordination. *Inorganic Chemistry*, 17(9):2553–2568, 1978.

[21] F. Castet, G. D'Avino, L. Muccioli, J. Cornil, and D. Beljonne. Charge separation energetics at organic heterojunctions: on the role of structural and electrostatic disorder. *Physical Chemistry Chemical Physics*, 16(38):20279–20290, 2014.

[22] A. L. F. Cauduro, R. Dos Reis, G. Chen, A. K. Schmid, C. Methivier, H. G. Rubahn, L. Bossard-Giannesini, H. Cruguel, N. Witkowski, and M. Madsen. Crystalline molybdenum oxide thin-films for application as interfacial layers in optoelectronic devices. *Acs Applied Materials and Interfaces*, 9(8):7717–7724, 2017.

[23] A. T. Chang and J. C. Marchon. Preparation and characterization of oxidized and reduced forms of lutetium diphthalocyanine. *Inorganica Chimica Acta-Letters*, 53(6):L241–L243, 1981.

[24] Z. H. Cheng, L. Gao, Z. T. Deng, N. Jiang, Q. Liu, D. X. Shi, S. X. Du, H. M. Guo, and H. J. Gao. Adsorption behavior of iron phthalocyanine on au(111) surface at submonolayer coverage. *Journal of Physical Chemistry C*, 111(26):9240–9244, 2007.

[25] S. Ciuchi and S. Fratini. Electronic transport and quantum localization effects in organic semiconductors. *Physical Review B*, 86(24), 2012.

[26] C. Clarisse and M. T. Riou. Synthesis and characterization of some lanthanide phthalocyanines. *Inorganica Chimica Acta*, 130(1):139–144, 1987.

[27] R. S. Clegg and J. E. Hutchison. Hydrogen-bonding, self-assembled monolayers: Ordered molecular films for study of through-peptide electron transfer. *Langmuir*, 12(22):5239–5243, 1996.

[28] R. J. Cole, B. G. Frederick, and P. Weightman. Substrate dependence of adlayer optical response in reflectance anisotropy spectroscopy. *Journal of Vacuum Science & Technology a-Vacuum Surfaces and Films*, 16(5):3088–3095, 1998.

[29] N. Coppede, E. Bonnini, F. Mezzadri, G. Tarabella, P. Ranzieri, L. Barba, G. Arrighetti, L. Lutterotti, and S. Iannotta. Structural and morphological phase control by supersonic beams on titanyl phthalocyanine: An investigation on the growth. *Organic Electronics*, 32:15–20, 2016.

[30] V. Coropceanu, J. Cornil, D. A. da Silva, Y. Olivier, R. Silbey, and J. L. Bredas. Charge transport in organic semiconductors. *Chemical Reviews*, 107(4):926–952, 2007.

[31] V. Coropceanu, H. Li, P. Winget, L. Y. Zhu, and J. L. Bredas. *Electronic-Structure Theory of Organic Semiconductors: Charge-Transport Parameters and Metal/Organic Interfaces*, volume 43 of *Annual Review of Materials Research*, pages 63–87. 2013.

[32] M. Corva and E. Vesselli. Room temperature carbonylation of iron-phthalocyanines adsorbed on a single crystal metal surface: An in situ sfg investigation at near-ambient pressure. *Journal of Physical Chemistry C*, 120(39):22298–22303, 2016.

[33] A. Curcella, R. Bernard, Y. Borensztein, M. Lazzeri, A. Resta, Y. Garreau, and G. Prevot. Multilayer silicene: clear evidence of ag-terminated bulk silicon. *2d Materials*, 4(2), 2017.

[34] A. N. Darovskikh, A. K. Tsytsenko, O. V. Frankkamenetskaya, V. S. Fundamensky, and P. N. Moskalev. Neodymium diphthalocyanine polymorphism - the molecular and crystal-structyre of the beta-phase. *Kristallografiya*, 29(3):455–461, 1984.

[35] A. T. Davidson. The effect of the metal atom on the absorption-spectra of phthalocyanine films. *Journal of Chemical Physics*, 77(1):168–172, 1982.

[36] A. Decian, M. Moussavi, J. Fischer, and R. Weiss. Synthesis, structure, and spectroscopic and magnetic-properties of lutetium(iii) phthalocyanine derivatives - lupc2.ch2cl2 and lupc(oac)(h2o)2.h2o.2ch3oh. *Inorganic Chemistry*, 24(20):3162–3167, 1985.

[37] G. N. Derry and P. N. Ross. A work function change study of oxygen-adsorption on pt(111) and pt(100). *Journal of Chemical Physics*, 82(6):2772–2778, 1985.

[38] L. Derue, O. Dautel, A. Tournebize, M. Drees, H. L. Pan, S. Berthumeyrie, B. Pavageau, E. Cloutet, S. Chambon, L. Hirsch, A. Rivaton, P. Hudhomme, A. Facchetti, and G. Wantz. Thermal stabilisation of polymer-fullerene bulk heterojunction morphology for effi cient photovoltaic solar cells. *Advanced Materials*, 26(33):5831–5838, 2014.

[39] J. Diaz, G. Paolicelli, S. Ferrer, and F. Comin. Separation of the sp(3) and sp(2) components in the c1s photoemission spectra of amorphous carbon films. *Physical Review B*, 54(11):8064–8069, 1996.

[40] S. Doniach and M. Sunjic. Many-electron singularity in x-ray photoemission and x-ray line spectra from metals. *Journal of Physics Part C Solid State Physics*, 3(2):285–291, 1970.

[41] S. Dreiner, M. Schurmann, M. Krause, U. Berges, and C. Westphal. Determination of the source of two extra components in si 2p photoelectron spectra of the sio2/si(100) interface. *Journal of Electron Spectroscopy and Related Phenomena*, 144:405–408, 2005.

[42] R. F. Egerton, P. Li, and M. Malac. Radiation damage in the tem and sem. *Micron*, 35(6):399–409, 2004.

[43] A. Einstein. On a heuristic viewpoint concerning the production and transformation of light. *Annalen der Physik*, 17:16, 1905.

[44] A. El-Sayed, P. Borghetti, E. Goiri, C. Rogero, L. Floreano, G. Lovat, D. J. Mowbray, J. L. Cabellos, Y. Wakayama, A. Rubio, J. E. Ortega, and D. G.

de Oteyza. Understanding energy-level alignment in donor-acceptor/metal interfaces from core-level shifts. *Acs Nano*, 7(8):6914–6920, 2013.

[45] S. Evans. Curve synthesis and optimization procedures for x-ray photoelectron-spectroscopy. *Surface and Interface Analysis*, 17(2):85–93, 1991.

[46] S. Fahrendorf, N. Atodiresei, C. Besson, V. Caciuc, F. Matthes, S. Blugel, P. Kogerler, D. E. Burgler, and C. M. Schneider. Accessing 4f-states in single-molecule spintronics. *Nature Communications*, 4, 2013.

[47] B. G. Fanchiotti, M. P. Z. Machado, L. C. de Paula, M. Durmus, T. Nyokong, A. D. Goncalves, and A. R. da Silva. The photobleaching of the free and encapsulated metallic phthalocyanine and its effect on the photooxidation of simple molecules. *Journal of Photochemistry and Photobiology B-Biology*, 165:10–23, 2016.

[48] K. Flechtner, A. Kretschmann, H.-P. Steinrueck, and J. M. Gottfried. No-induced reversible switching of the electronic interaction between a porphyrin-coordinated cobalt ion and a silver surface. *Journal of the American Chemical Society*, 129(40):12110–+, 2007.

[49] L. Floreano, A. Cossaro, R. Gotter, A. Verdini, G. Bavdek, F. Evangelista, A. Ruocco, A. Morgante, and D. Cvetko. Periodic arrays of cu-phthalocyanine chains on au(110). *Journal of Physical Chemistry C*, 112(29):10794–10802, 2008.

[50] I. S. Flyagina, K. J. Hughes, M. Pourkashanian, and D. B. Ingham. Dft study of the oxygen reduction reaction on iron, cobalt and manganese macrocycle active sites. *International Journal of Hydrogen Energy*, 39(36):21538–21546, 2014.

[51] R. Forker and T. Fritz. Optical differential reflectance spectroscopy of ultrathin epitaxial organic films. *Physical Chemistry Chemical Physics*, 11(13):2142–2155, 2009.

[52] T. Fransson, Y. Harada, N. Kosugi, N. A. Besley, B. Winter, J. J. Rehr, L. G. M. Pettersson, and A. Nilsson. X-ray and electron spectroscopy of water. *Chemical Reviews*, 116(13):7551–7569, 2016.

[53] S. Frey, H. T. Rong, K. Heister, Y. J. Yang, M. Buck, and M. Zharnikov. Response of biphenyl-substituted alkanethiol self-assembled monolayers to electron irradiation: Damage suppression and odd-even effects. *Langmuir*, 18(8):3142–3150, 2002.

[54] K. Fukuda, T. Sekitani, and T. Someya. Effects of annealing on electronic and structural characteristics of pentacene thin-film transistors on polyimide gate dielectrics. *Applied Physics Letters*, 95(2), 2009.

[55] B. Gao, Z. Y. Wu, and Y. Luo. A density functional theory study of shake-up satellites in photoemission of carbon fullerenes and nanotubes. *Journal of Chemical Physics*, 128(23), 2008.

[56] G. Giri, E. Verploegen, S. C. B. Mannsfeld, S. Atahan-Evrenk, D. H. Kim, S. Y. Lee, H. A. Becerril, A. Aspuru-Guzik, M. F. Toney, and Z. A. Bao. Tuning charge transport in solution-sheared organic semiconductors using lattice strain. *Nature*, 480(7378):504–U124, 2011.

[57] E. Goiri, P. Borghetti, A. El-Sayed, J. E. Ortega, and D. G. de Oteyza. Multicomponent organic layers on metal substrates. *Advanced Materials*, 28(7):1340–1368, 2016.

[58] H. Z. Gok and B. Farsak. Synthesis and spectral properties of novel metal-free and metallophthalocyanines bearing four 19-membered tetrathiadiaza macrocycles. *Journal of Molecular Structure*, 1054:25–31, 2013.

[59] W. Greenbank, L. Hirsch, G. Wantz, and S. Chambon. Interfacial thermal degradation in inverted organic solar cells. *Applied Physics Letters*, 107(26), 2015.

[60] M. T. Greiner, M. G. Helander, W. M. Tang, Z. B. Wang, J. Qiu, and Z. H. Lu. Universal energy-level alignment of molecules on metal oxides. *Nature Materials*, 11(1):76–81, 2012.

[61] S. Guha, W. Graupner, S. Yang, M. Chandrasekhar, and H. R. Chandrasekhar. *Optical Properties of Organic Wide Band-Gap Semiconductors under High Pressure*, chapter 9, pages 127–142.

[62] V. Heine and L. D. Marks. Competition between pairwise and multi-atom forces at noble-metal surfaces. *Surface Science*, 165(1):65–82, 1986.

[63] K. Heister, H. T. Rong, M. Buck, M. Zharnikov, M. Grunze, and L. S. O. Johansson. Odd-even effects at the s-metal interface and in the aromatic matrix of biphenyl-substituted alkanethiol self-assembled monolayers. *Journal of Physical Chemistry B*, 105(29):6888–6894, 2001.

[64] J. Hollenshead and L. Klebanoff. Modeling radiation-induced carbon contamination of extreme ultraviolet optics. *Journal of Vacuum Science & Technology B*, 24(1):64–82, 2006.

[65] L. G. Hu, X. Liu, S. Dalgleish, M. M. Matsushita, H. Yoshikawa, and K. Awaga. Organic optoelectronic interfaces with anomalous transient photocurrent. *Journal of Materials Chemistry C*, 3(20):5122–5135, 2015.

[66] Y. L. Huang, E. Wruss, D. A. Egger, S. Kera, N. Ueno, W. A. Saidi, T. Bucko, A. T. S. Wee, and E. Zojer. Understanding the adsorption of cupc and znpc on noble metal surfaces by combining quantum-mechanical modelling and photoelectron spectroscopy. *Molecules*, 19(3):2969–2992, 2014.

[67] M. A. Huels, P. C. Dugal, and L. Sanche. Degradation of functionalized alkanethiolate monolayers by 0-18 ev electrons. *Journal of Chemical Physics*, 118(24):11168–11178, 2003.

[68] S. Hufner. *Photoelectron spectroscopy: Principles and applications*. Springer, Berlin, 2003.

[69] J. E. Huheey, E. A. Keiter, and R. A. Keiter. *Inorganic Chemistry: Principles of Structure and Reactivity*. Harper Collins College Publisher, New York, 1993.

[70] C. A. Hunter and J. K. M. Sanders. The nature of pi-pi interactions. *Journal of the American Chemical Society*, 112(14):5525–5534, 1990.

[71] S. Illig, A. S. Eggeman, A. Troisi, L. Jiang, C. Warwick, M. Nikolka, G. Schweicher, S. G. Yeates, Y. H. Geerts, J. E. Anthony, and H. Sirringhaus. Reducing dynamic disorder in small-molecule organic semiconductors by suppressing large-amplitude thermal motions. *Nature Communications*, 7, 2016.

[72] N. Kawasaki, Y. Kubozono, H. Okamoto, A. Fujiwara, and M. Yamaji. Trap states and transport characteristics in picene thin film field-effect transistor. *Applied Physics Letters*, 94(4), 2009.

[73] K. W. Kolasinski. *Surface Science: Foundations of Catalysis and Nanoscience*. Wiley, Chichester, England, 2008.

[74] T. Komeda, H. Isshiki, and J. Liu. Metal-free phthalocyanine (h2pc) molecule adsorbed on the au(111) surface: formation of a wide domain along a single lattice direction. *Science and Technology of Advanced Materials*, 11(5), 2010.

[75] T. Komeda, K. Katoh, and M. Yamashita. Double-decker phthalocyanine complex: Scanning tunneling microscopy study of film formation and spin properties. *Progress in Surface Science*, 89(2):127–160, 2014.

[76] T. Koopmans. The classification of wave functions and eigen-values to the single electrons of an atom. *Physica*, 1:104–113, 1934.

[77] B. Krause, A. C. Durr, K. Ritley, F. Schreiber, H. Dosch, and D. Smilgies. Structure and growth morphology of an archetypal system for organic epitaxy: Ptcda on ag(111). *Physical Review B*, 66(23), 2002.

[78] F. C. Krebs. Roll-to-roll fabrication of monolithic large-area polymer solar cells free from indium-tin-oxide. *Solar Energy Materials and Solar Cells*, 93(9):1636–1641, 2009.

[79] F. C. Krebs, T. Tromholt, and M. Jorgensen. Upscaling of polymer solar cell fabrication using full roll-to-roll processing. *Nanoscale*, 2(6):873–886, 2010.

[80] I. Kroger, B. Stadtmuller, and C. Kumpf. Submonolayer and multilayer growth of titaniumoxide-phthalocyanine on ag(111). *New Journal of Physics*, 18, 2016.

[81] H.-S. Lee and S.-G. Kim. Threshold voltage properties of ofet with cupc active material. *Journal of Information and Communication Convergence Engineering*, 13(4):257 – 263, 2015.

[82] T. H. Lee and J. W. Rabalais. X-ray photoelectron-spectra and electronic structure of some diamine compounds. *Journal of Electron Spectroscopy and Related Phenomena*, 11(1):123–127, 1977.

[83] A. F. G. Leontowich and A. P. Hitchcock. Secondary electron deposition mechanism of carbon contamination. *Journal of Vacuum Science & Technology B*, 30(3), 2012.

[84] A. F. G. Leontowich, A. P. Hitchcock, and R. F. Egerton. Radiation damage yields across the carbon 1s excitation edge. *Journal of Electron Spectroscopy and Related Phenomena*, 206:58–64, 2016.

[85] R. Lessmann, Z. Hong, S. Scholz, B. Maennig, M. K. Riede, and K. Leo. Aging of flat heterojunction zinc phthalocyanine/fullerene c-60 organic solar cells. *Organic Electronics*, 11(4):539–543, 2010.

[86] H. Li, P. Winget, and J. L. Bredast. Transparent conducting oxides of relevance to organic electronics: Electronic structures of their interfaces with organic layers. *Chemistry of Materials*, 26(1):631–646, 2014.

[87] N. Lin, J. Qiao, L. Duan, H. F. Li, L. D. Wang, and Y. Qiu. Achilles heels of phosphine oxide materials for oleds: Chemical stability and degradation mechanism of a bipolar phosphine oxide/carbazole hybrid host material. *Journal of Physical Chemistry C*, 116(36):19451–19457, 2012.

[88] L. Lozzi, S. Picozzi, S. Santucci, C. Cantalini, and B. Delley. Photoemission and theoretical investigations on no2 doping of copper phthalocyanine thin films. *Journal of Electron Spectroscopy and Related Phenomena*, 137:101–105, 2004.

[89] L. Y. Lu, T. Y. Zheng, Q. H. Wu, A. M. Schneider, D. L. Zhao, and L. P. Yu. Recent advances in bulk heterojunction polymer solar cells. *Chemical Reviews*, 115(23):12666–12731, 2015.

[90] M. C. Lu, R. B. Wang, A. Yang, and S. Duhm. Pentacene on au(111), ag(111) and cu(111): From physisorption to chemisorption. *Journal of Physics-Condensed Matter*, 28(9), 2016.

[91] B. Lussem, M. L. Tietze, H. Kleemann, C. Hossbach, J. W. Bartha, A. Zakhidov, and K. Leo. Doped organic transistors operating in the inversion and depletion regime. *Nature Communications*, 4, 2013.

[92] R. Madru, G. Guillaud, M. Alsadoun, M. Maitrot, J. J. Andre, J. Simon, and R. Even. A well-behaved field effect transistor based on an intrinsic molecular semiconductor. *Chemical Physics Letters*, 145(4):343–346, 1988.

[93] M. Maitrot, G. Guillaud, B. Boudjema, J. J. Andre, H. Strzelecka, J. Simon, and R. Even. Lutetium bisphthalocyanine - the 1st molecular semiconductor - conduction properties of thin-films of p-doped and n-doped materials. *Chemical Physics Letters*, 133(1):59–62, 1987.

[94] T. Makela, S. Jussila, H. Kosonen, T. G. Backlund, H. G. O. Sandberg, and H. Stubb. Utilizing roll-to-roll techniques for manufacturing source-drain electrodes for all-polymer transistors. *Synthetic Metals*, 153(1-3):285–288, 2005.

[95] G. Margaritondo. A primer in synchrotron-radiation - everything you wanted to know about sex (synchrotron emission of x-rays) but were afraid to ask. *Journal of Synchrotron Radiation*, 2:148–154, 1995.

[96] P. Matyba, H. Yamaguchi, G. Eda, M. Chhowalla, L. Edman, and N. D. Robinson. Graphene and mobile ions: The key to all-plastic, solution-processed light-emitting devices. *Acs Nano*, 4(2):637–642, 2010.

[97] A. Meents, B. Dittrich, and S. Gutmann. A new aspect of specific radiation damage: hydrogen abstraction from organic molecules. *Journal of Synchrotron Radiation*, 16:183–190, 2009.

[98] P. N. Moskalev, G. N. Shapkin, and A. N. Darovskikh. Synthesis and properties of electrochemically oxidized dipththalocyanine of rare-earth elements and americium. *Zhurnal Neorganicheskoi Khimii*, 24(2):340–346, 1979.

[99] N. F. Mott. Conduction in glass containing transition metal ions. *Journal of Non-Crystalline Solids*, 1(1):1–17, 1968.

[100] M. Msadak, J. Roncali, and F. Garnier. Rare-earth substitution effect on the electrochemical properties of lanthanide diphthalocyanine. *Journal of Electroanalytical Chemistry*, 189(1):99–111, 1985.

[101] R. Murdey, M. Bouvet, M. Sumimoto, S. Sakaki, and N. Sato. Direct observation of the energy gap in lutetium bisphthalocyanine thin films. *Synthetic Metals*, 159(15-16):1677–1681, 2009.

[102] Y. Nakayama, Y. Mizuno, M. Hikasa, M. Yamamoto, M. Matsunami, S. Ideta, K. Tanaka, H. Ishii, and N. Ueno. Single-crystal pentacene valence-band dispersion and its temperature dependence. *Journal of Physical Chemistry Letters*, 8(6):1259–1264, 2017.

[103] D. Necas and P. Klapetek. Gwyddion: an open-source software for spm data analysis. *Central European Journal of Physics*, 10(1):181–188, 2012.

[104] A. Neuhold, J. Novak, H. G. Flesch, A. Moser, T. Djuric, L. Grodd, S. Grigorian, U. Pietsch, and R. Resel. X-ray radiation damage of organic semiconductor

thin films during grazing incidence diffraction experiments. *Nuclear Instruments & Methods in Physics Research Section B-Beam Interactions with Materials and Atoms*, 284:64–68, 2012.

[105] R. Nyholm, S. Svensson, J. Nordgren, and A. Flodstrom. A soft-x-ray monochromator for the max synchrotron radiation facility. *Nuclear Instruments & Methods in Physics Research Section a-Accelerators Spectrometers Detectors and Associated Equipment*, 246(1-3):267–271, 1986.

[106] H. Ogasawara, B. Brena, D. Nordlund, M. Nyberg, A. Pelmenschikov, L. G. M. Pettersson, and A. Nilsson. Structure and bonding of water on pt(111). *Physical Review Letters*, 89(27), 2002.

[107] E. Orti, J. L. Bredas, and C. Clarisse. Electronic structure of phthalocyanines - theoretical investigation of the optical properties of phthalocyanine monomers, dimers and crystals. *Journal of Chemical Physics*, 92(2):1228–1235, 1990.

[108] L. Ottaviano, L. Lozzi, and S. Santucci. Interaction of naphthalocyanine with oxygen and with si(111) 7x7: an in-situ x-ray photoelectron spectroscopy study. *Surface Science*, 431(1-3):242–251, 1999.

[109] K. Oura, V. G. Lifshits, A. A. Saranin, A. V. Zotov, and M. Katayama. *Surface Science - An introduction*. Springer, Berlin, 2003.

[110] N. Padma, S. Sen, S. N. Sawant, and R. Tokas. A study on threshold voltage stability of low operating voltage organic thin-film transistors. *Journal of Physics D-Applied Physics*, 46(32), 2013.

[111] G. Pan, G. Z. He, M. Y. Zhang, Q. Zhou, T. Tyliszczak, R. Z. Tai, J. H. Guo, L. Bi, L. Wang, and H. G. Zhang. Nanobubbles at hydrophilic particle-water interfaces. *Langmuir*, 32(43):11133–11137, 2016.

[112] J. H. Park, L. Ravavar, I. Kwak, S. K. Fullerton-Shirey, P. Choudhury, and A. C. Kummel. Growth mode transition from monolayer by monolayer to bilayer by bilayer in molecularly flat titanyl phthalocyanine film. *Journal of Physical Chemistry C*, 121(12):6721–6728, 2017.

[113] M. Passard, J. P. Blanc, and C. Maleysson. Gaseous oxidation and compensating reduction of lutetium bis-phthalocyanine and lutetium phthalonaphthalocyanine films. *Thin Solid Films*, 271(1-2):8–14, 1995.

[114] N. Pauly, F. Yubero, and S. Tougaard. Quantitative analysis of satellite structures in xps spectra of gold and silver. *Applied Surface Science*, 383:317–323, 2016.

[115] C. Puglia, A. Nilsson, B. Hernnas, O. Karis, P. Bennich, and N. Martensson. Physisorbed, chemisorbed and dissociated o2 on pt(111) studied by different core-level spectroscopy methods. *Surface Science*, 342(1-3):119–133, 1995.

[116] E. E. Rennie, B. Kempgens, H. M. Koppe, U. Hergenhahn, J. Feldhaus, B. S. Itchkawitz, A. L. D. Kilcoyne, A. Kivimaki, K. Maier, M. N. Piancastelli, M. Polcik, A. Rudel, and A. M. Bradshaw. A comprehensive photoabsorption, photoionization, and shake-up excitation study of the c 1s cross section of benzene. *Journal of Chemical Physics*, 113(17):7362–7375, 2000.

[117] R. Resel, O. Lengyel, T. Haber, O. Werzer, W. Hardeman, D. M. de Leeuw, and H. J. Wondergem. Wide-range three-dimensional reciprocal-space mapping: a novel approach applied to organic monodomain thin films. *Journal of Applied Crystallography*, 40:580–582, 2007.

[118] J. M. Robertson. An x-ray study of the structure of the phthalocyanines part i the metal-free, nickel, copper, and platinum compounds. *Journal of the Chemical Society*, pages 615–621, 1935.

[119] L. Romaner, G. Heimel, J. L. Bredas, A. Gerlach, F. Schreiber, R. L. Johnson, J. Zegenhagen, S. Duhm, N. Koch, and E. Zojer. Impact of bidirectional charge transfer and molecular distortions on the electronic structure of a metal-organic interface. *Physical Review Letters*, 99(25), 2007.

[120] R. Rousseau, R. Aroca, and M. L. Rodriguezmendez. Extended huckel molecular orbital model for lanthanide bisphthalocyanine complexes. *Journal of Molecular Structure*, 356(1):49–62, 1995.

[121] A. Scholl, Y. Zou, M. Jung, T. Schmidt, R. Fink, and E. Umbach. Line shapes and satellites in high-resolution x-ray photoelectron spectra of large pi-conjugated organic molecules. *Journal of Chemical Physics*, 121(20):10260–10267, 2004.

[122] S. Scholz, D. Kondakov, B. Luessem, and K. Leo. Degradation mechanisms and reactions in organic light-emitting devices. *Chemical Reviews*, 115(16):8449–8503, 2015.

[123] F. Sedona, M. Di Marino, D. Forrer, A. Vittadini, M. Casarin, A. Cossaro, L. Floreano, A. Verdini, and M. Sambi. Tuning the catalytic activity of ag(110)-supported fe phthalocyanine in the oxygen reduction reaction. *Nature Materials*, 11(11):970–977, 2012.

[124] A. Seemann, T. Sauermann, C. Lungenschmied, O. Armbruster, S. Bauer, H. J. Egelhaaf, and J. Hauch. Reversible and irreversible degradation of organic solar cell performance by oxygen. *Solar Energy*, 85(6):1238–1249, 2011.

[125] J. A. Sellberg, S. Kaya, V. H. Segtnan, C. Chen, T. Tyliszczak, H. Ogasawara, D. Nordlund, L. G. M. Pettersson, and A. Nilsson. Comparison of x-ray absorption spectra between water and ice: New ice data with low pre-edge absorption cross-section. *Journal of Chemical Physics*, 141(3), 2014.

[126] B. R. Sheu, S. Chaturvedi, and D. R. Strongin. Adsorption and decomposition of methanol on nial(110). *Journal of Physical Chemistry*, 98(40):10258–10268, 1994.

[127] H. Shirakawa, E. J. Louis, A. G. Macdiarmid, C. K. Chiang, and A. J. Heeger. Synthesis of electrically conducting organic polymers - halogen derivatives of polyacetylene (ch)x. *Journal of the Chemical Society-Chemical Communications*, (16):578–580, 1977.

[128] S. Shoaee and J. R. Durrant. Oxygen diffusion dynamics in organic semiconductor films. *Journal of Materials Chemistry C*, 3(39):10079–10084, 2015.

[129] J. L. Solomon, R. J. Madix, and J. Stohr. Orientation and absolute coverage of furan and 2,5-dihydrofuran on ag(110) determined by near edge x-ray absorption fine-structure and x-ray photoelectron-spectroscopy. *Journal of Chemical Physics*, 94(5):4012–4023, 1991.

[130] R. Sondergaard, M. Hosel, D. Angmo, T. T. Larsen-Olsen, and F. C. Krebs. Roll-to-roll fabrication of polymer solar cells. *Materials Today*, 15(1-2):36–49, 2012.

[131] P. Stallinga. Electronic transport in organic materials: Comparison of band theory with percolation/(variable range) hopping theory. *Advanced Materials*, 23(30):3356–3362, 2011.

[132] J. Stöhr. *NEXAFS Spectroscopy*, volume 25 of *Springer Series in Surface Science*. Berlin, 2003.

[133] H. Sugimoto, M. Mori, H. Masuda, and T. Taga. Synthesi and molecular structure of a lithium complex of the phthalocyanine radical. *Journal of the Chemical Society-Chemical Communications*, (12):962–963, 1986.

[134] V. C. Sundar, J. Zaumseil, V. Podzorov, E. Menard, R. L. Willett, T. Someya, M. E. Gershenson, and J. A. Rogers. Elastomeric transistor stamps: Reversible probing of charge transport in organic crystals. *Science*, 303(5664):1644–1646, 2004.

[135] D. R. Tackley, G. Dent, and W. E. Smith. Phthalocyanines: structure and vibrations. *Physical Chemistry Chemical Physics*, 3(8):1419–1426, 2001.

[136] Y. Tai, A. Shaporenko, W. Eck, M. Grunze, and M. Zharnikov. Depth distribution of irradiation-induced cross-linking in aromatic self-assembled monolayers. *Langmuir*, 20(17):7166–7170, 2004.

[137] S. Tanuma, C. J. Powell, and D. R. Penn. Calculations of electron inelastic mean free paths .5. data for 14 organic-compounds over the 50-2000 ev range. *Surface and Interface Analysis*, 21(3):165–176, 1994.

[138] M. Toader, M. Knupfer, D. R. T. Zahn, and M. Hietschold. Initial growth of lutetium(iii) bis-phthalocyanine on ag(111) surface. *Journal of the American Chemical Society*, 133(14):5538–5544, 2011.

[139] A. Turchanin, D. Kafer, M. El-Desawy, C. Woll, G. Witte, and A. Golzhauser. Molecular mechanisms of electron-induced cross-linking in aromatic sams. *Langmuir*, 25(13):7342–7352, 2009.

[140] P. Tyagi, R. Srivastava, L. I. Giri, S. Tuli, and C. Lee. Degradation of organic light emitting diode: Heat related issues and solutions. *Synthetic Metals*, 216:40–50, 2016.

[141] M. A. Vanhove, R. J. Koestner, P. C. Stair, J. P. Biberian, L. L. Kesmodel, I. Bartos, and G. A. Somorjai. The surface reconstruction of the (100) crystal faces of iridium, platinum and gold .1. experimental observations and possible structural models. *Surface Science*, 103(1):189–217, 1981.

[142] J. Vegh. Alternative form for the pseudo-voigt peak shape. *Review of Scientific Instruments*, 76(5), 2005.

[143] G. Volonakis, L. Tsetseris, and S. Logothetidis. Impurity-related degradation in a prototype organic photovoltaic material: A first-principles study. *Organic Electronics*, 14(5):1242–1248, 2013.

[144] J. Wang, A. J. Davenport, H. S. Isaacs, and B. M. Ocko. Surface-charge induced ordering of the au(111) surface. *Science*, 255(5050):1416–1418, 1992.

[145] N. N. Wang, X. R. Tong, Q. Burlingame, J. S. Yu, and S. R. Forrest. Photodegradation of small-molecule organic photovoltaics. *Solar Energy Materials and Solar Cells*, 125:170–175, 2014.

[146] Y. Wang, N. S. Hush, and J. R. Reimers. Simulation of the au(111)-(22 x root 3) surface reconstruction. *Physical Review B*, 75(23), 2007.

[147] J. M. Warman, M. P. de Haas, G. Dicker, F. C. Grozema, J. Piris, and M. G. Debije. Charge mobilities in organic semiconducting materials determined by pulse-radiolysis time-resolved microwave conductivity: pi-bond-conjugated polymers versus pi-pi-stacked discotics. *Chemistry of Materials*, 16(23):4600–4609, 2004.

[148] B. Warner, F. El Hallak, N. Atodiresei, P. Seibt, H. Pruser, V. Caciuc, M. Waters, A. J. Fisher, S. Blugel, J. van Slageren, and C. F. Hirjibehedin. Sub-molecular modulation of a 4f driven kondo resonance by surface-induced asymmetry. *Nature Communications*, 7, 2016.

[149] S. Yadav and S. Ghosh. Low voltage pentacene organic field effect transistors with high-k gate dielectric. *Physics of Semiconductor Devices*, pages 905–906, 2014.

[150] J. J. Yeh and I. Lindau. Atomic subshell photoionization cross-sections and asymmetry parameters - 1 less-than-or-equal-to z less-than-or-equal-to 103. *Atomic Data and Nuclear Data Tables*, 32(1):1–155, 1985.

[151] F. A. Yildirim, R. R. Schliewe, W. Bauhofer, R. M. Meixner, H. Goebel, and W. Krautschneider. Gate insulators and interface effects in organic thin-film transistors. *Organic Electronics*, 9(1):70–76, 2008.

[152] S. Yim, S. Heutz, and T. S. Jones. Model for the alpha ->beta(1) phase transition in phthalocyanine thin films. *Journal of Applied Physics*, 91(6):3632–3636, 2002.

[153] J. L. Zhang, Z. Z. Wang, J. Q. Zhong, K. D. Yuan, Q. Shen, L. L. Xu, T. C. Niu, C. D. Gu, C. A. Wright, A. Tadich, D. C. Qi, H. X. Li, K. Wu, G. Q. Xu, Z. Y. Li, and W. Chen. Single-molecule imaging of activated nitrogen adsorption on individual manganese phthalocyanine. *Nano Letters*, 15(5):3181–3188, 2015.

[154] L. S. Zhang, S. S. Roy, R. J. Hamers, M. S. Arnold, and T. L. Andrew. Molecular orientation-dependent interfacial energetics and built-in voltage tuned by a template graphene monolayer. *Journal of Physical Chemistry C*, 119(1):45–54, 2015.

[155] Y. Zhang, P. Guan, H. Isshiki, M. Chen, M. Yamashita, and T. Komeda. Bis(phthalocyaninato)yttrium grown on au(111): Electronic structure of a single molecule and the stability of two-dimensional films investigated by scanning tunneling microscopy/spectroscopy at 4.8 k. *Nano Research*, 3(8):604–611, 2010.

[156] Y. L. Zhao, W. H. Wang, F. Qi, J. F. Li, G. W. Kuang, R. Q. Zhang, N. Lin, and M. A. van Hove. Donor/acceptor properties of aromatic molecules in complex metal-molecule interfaces. *Langmuir*, 33(2):451–458, 2017.

[157] M. Zharnikov, W. Geyer, A. Golzhauser, S. Frey, and M. Grunze. Modification of alkanethiolate monolayers on au-substrate by low energy electron irradiation: Alkyl chains and the s/au interface. *Physical Chemistry Chemical Physics*, 1(13):3163–3171, 1999.

[158] Q. S. Zheng, S. Jockusch, Z. Zhou, and S. C. Blanchard. The contribution of reactive oxygen species to the photobleaching of organic fluorophores. *Photochemistry and Photobiology*, 90(2):448–454, 2014.

[159] S. Zhong, J. Q. Zhong, A. T. S. Wee, and W. Chen. Molecular orientation and electronic structure at organic heterojunction interfaces. *Journal of Electron Spectroscopy and Related Phenomena*, 204:12–22, 2015.

[160] K. Zojer, E. Zojer, A. F. Fernandez, and M. Gruber. Impact of the capacitance of the dielectric on the contact resistance of organic thin-film transistors. *Physical Review Applied*, 4(4), 2015.